School of Molecular and Life Sciences

Shedding Light on the Structural and Luminescent Properties of Lanthanoid β-Triketonate Complexes

Lee John Cameron

This thesis is presented for the Degree of
Master of Research
of
Curtin University

November 2019

Declaration

To the best of my knowledge and belief, this thesis contains no material previously published by any other person except where due acknowledgment has been made.

This thesis contains no material which has been accepted for the award of any other degree or diploma in any university.

Signature:

Date: 29-11-2019

“Sometimes life is like this dark tunnel. You can’t always see the light at the end of the tunnel, but if you just keep moving… you will come to a better place”

– Uncle Iroh

Abstract

This thesis presents research centred around the structural and photophysical characterisation of new *β*-diketonate and *β*-triketonate lanthanoid complexes. In Chapter 1, background information is given, discussing the properties of lanthanoid complexes alongside the ligands utilised in these luminescent systems. Chapter 2 reports an investigation utilising tribenzoylmethane (**tbm**H) in combination with various solvent ligands, which resulted in the formation of three differently solvated complexes with the general formula [Ln(**tbm**)$_3$(DMSO)(X)] where Ln = La^{3+}, Pr^{3+}, Sm^{3+}, Eu^{3+}, Tb^{3+}, Dy^{3+}, Er^{3+}, Yb^{3+}, Lu^{3+}, Y^{3+}; and X = DMSO, EtOH, or H_2O. Although consistent structural trends were identified in the H_2O solvated complexes, no overall trend could be identified that would allow the synthesis of specific solvates. In Chapter 3, the effect of 1,10-phenanthroline (phen) on the photophysical properties of lanthanoid complexes was explored. By comparing deuterated and non-deuterated phen in complexes with the formula [Ln(**tbm**)$_3$(phen)] (Ln = Sm^{3+}, Eu^{3+}, Yb^{3+}) it was found that phen had a significant quenching effect on the emission of the Yb^{3+} complex. Chapter 4 presents a series of *β*-diketonate complexes isolated as analogues to a previously reported series of *β*-triketonate complexes. Incorporating three dinaphthoylmethane (**dnm**H) ligands and two DMSO solvent ligands, an isostructural series for Ln = Nd^{3+}, Eu^{3+}, and Gd^{3+} was isolated. Although possessing a less distorted coordination sphere than their *β*-triketonate counterparts, the *β*-diketonate complexes revealed similar luminescent properties. Chapter 5 describes the synthesis of a new ligand for use in lanthanoid complexes, 3,3'-(1,3-phenylene)bis(2-benzoyl-1-phenylpropane-1,3-dione) (**Btbm**H$_2$). Lanthanoid complexes of the deprotonated precursor ligand 3,3'-(1,3-phenylene)bis(1-phenylpropane-1,3-dione) (**Bdbm**) were isolated. With a molecular formula of [Ln$_2$(**Bdbm**)$_3$(phen)$_2$] (Ln = Eu^{3+} and Yb^{3+}) these complexes are the first crystallographically characterised lanthanoid complexes of this ligand. When compared to the previously isolated [Eu(**tbm**)$_3$(phen)], a substantial increase in luminescent lifetime and quantum yield was observed for the room temperature solution phase measurements of the [Eu$_2$(**Bdbm**)$_3$(phen)$_2$] complex, although there were no significant changes in the

properties of the [Yb_2(**Bdbm**)$_3$(phen)$_2$] complex. Attempts made to study solution phase speciation are covered in Chapter 6. This investigation was carried out *via* NMR spectroscopy on complexes of specific lanthanoids (La^{3+}, Sm^{3+}, Lu^{3+}) and Y^{3+} complexes. The results showed that the coordination of a bidentate co-ligand such as phen generally resulted in well-defined spectra, however the coordination of solvent molecules such as DMSO, H_2O, and EtOH gave broad spectra that could not be readily interpreted. Chapter 7 summarises the key conclusions, in particular the effect of phen on near-infrared emitting lanthanoids and the potential of the bis-ketonate ligands for solution phase studies.

Acknowledgements

A number of people have helped me over the course of this project, and it would be remiss of me not to acknowledge them. First of all, I would like to thank my supervisor, Prof. Mark Ogden for his wisdom and guidance over these past years. My understanding of crystallography, the lanthanoids, and chemistry in general has grown greatly over this year due to his help, and the speed at which he provides feedback is phenomenal. Second, my co-supervisor A/Prof. Massimiliano Massi. My interest and knowledge in the field of photophysics has grown immensely under his supervision.

Thank you to Dr Alexandre Sobolev, Dr Stephen Moggach, and Gemma Turner from the University of Western Australia. Their help in collection and refinement of crystal structures was instrumental to this thesis.

To those poor souls stuck in the lab with me, the lunch crew, and my desk mates, thank you for all the laughs and good times, many friendships were forged, and it made work days enjoyable.

I'd like to give a special shout out to the scary Italian ladies Anna and Chiara for always being there to lend a helping hand. My general lab skills improved significantly under your guidance, and you were not only exceptional teachers, but also amazing friends.

Most importantly, I would like to thank my mentor and essentially third supervisor, Dr Laura Abad Galán. Without her initial guidance into the world of lanthanoid β-triketonate complexes I would have accomplished a fraction of what I did. From teaching me how to use a fluorimeter to interpreting crystallography data, her help set the foundations of my knowledge for which I will always be grateful.

Last but not least, I would like to thank my friends, family, and Kimba, for putting up with me during stressful times, and understanding when I seemingly disappeared off the face of the Earth whilst writing.

Contents

Symbols and Abbreviations

$4f^*$	Lanthanoid excited state
λ_{em}	Emission Wavelength
λ_{ex}	Excitation Wavelength
appt	Apparent
BET	Back Energy Transfer
BdbmH_2	Bis-dibenzoylmethane
bpy	bipyridine
br	broad
BtbmH_2	Bis-tribenzoylmethane
BTPR	Biaugmented Trigonal Prism
dbmH	Dibenzoylmethane
d-phen	Deuterated 1,10-phenanthroline
CD_3CN	Deuterated Acetonitrile
DCM	Dichloromethane
DMSO	Dimethylsulfoxide
dnmH	Dinaphthoylmethane
ED	Electric Dipole
ET	Energy Transfer
EtOH	Ethanol
$HNEt_3^+$	Triethylammonium
IC	Internal Conversion
ISC	Intersystem Crossing
IR	Infrared
LEIP	Lowest Energy Interconversion Pathway
Ln/Ln^{3+}	Lanthanoid/Yttrium
MD	Magnetic Dipole
MeCN	Acetonitrile
MeOD	Deuterated methanol
MeOH	Methanol
M.p.	Melting Point
NEt_3	Triethylamine

NIR	Near-Infrared
NMR	Nuclear Magnetic Resonance
OLED	Organic Light Emitting Device
phen	1,10-phenanthroline
RT	Room Temperature
S_0	Ground State
S_1	Lowest Excited Singlet State
SAPR	Square Antiprism
SOC	Spin Orbit Coupling
SS	Solid-state
T_1	Lowest Excited Triplet State
tbmH	Tribenzoylmethane
TDD	Triangular Dodecahedron
THF	Tetrahydrofuran
tnmH	Trinaphthoylmethane
tta	Thenoyltrifluoracetone
UV	Ultraviolet

List of Compounds

Abbreviation	*Compound*
	Ligands
dbmH	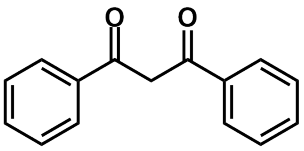
tbmH	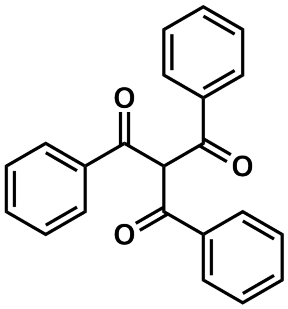
dnmH	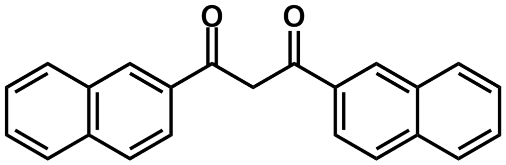
tnmH	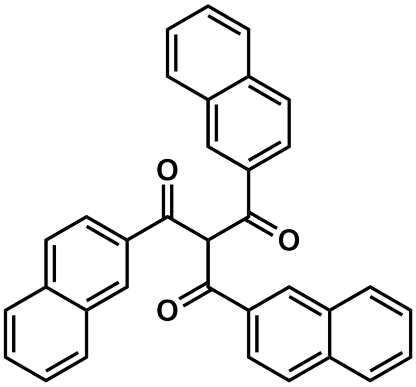
BdbmH_2	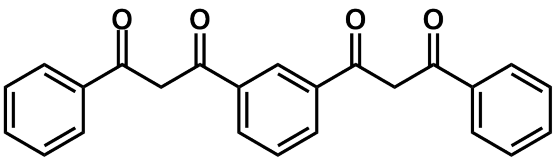

BtbmH_2

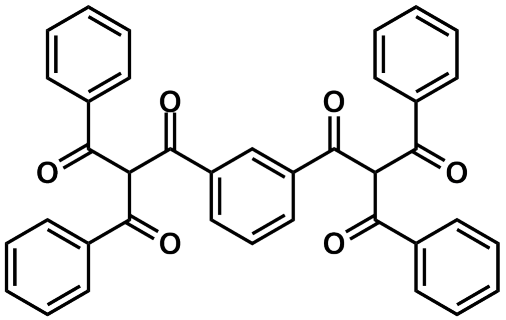

Lanthanoid Complexes

$(HNEt_3)[Sm(\mathbf{dbm})_4]\cdot(EtOH)$

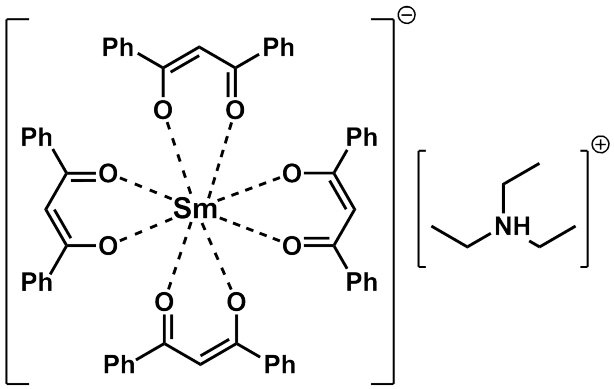

$[Sm(\mathbf{dbm})_3(phen)]\cdot(EtOH)$

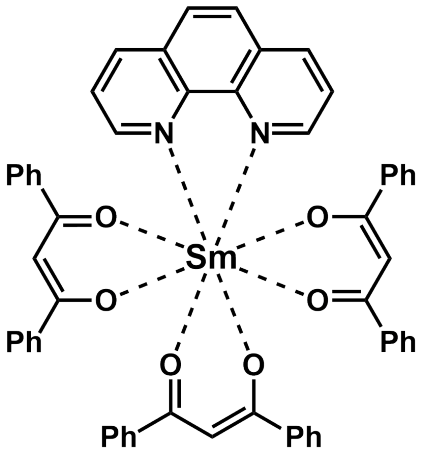

[Ln(**tbm**)$_3$(DMSO)$_2$]

Ln = La^{3+}, Sm^{3+}

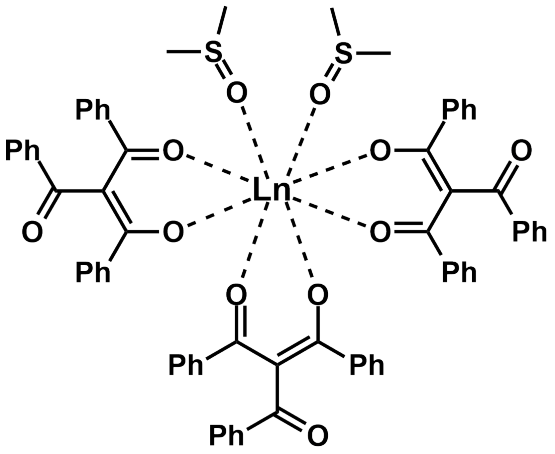

[Ln(**tbm**)$_3$(DMSO)(EtOH)]

Ln = La^{3+}, Pr^{3+}, Er^{3+}, Lu^{3+}

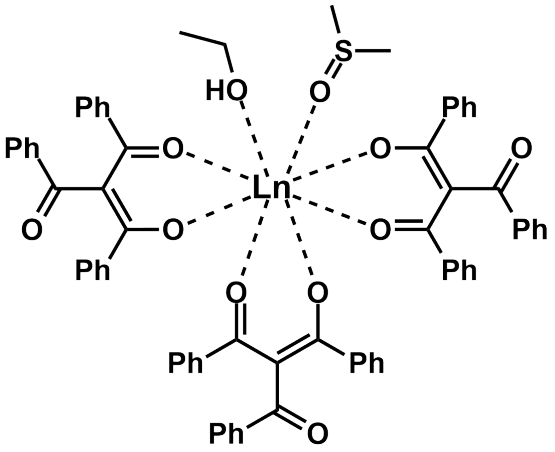

[Ln(**tbm**)$_3$(DMSO)(H_2O)]·(EtOH)

Ln = Eu^{3+}, Tb^{3+}, Dy^{3+}, Yb^{3+}, Y^{3+}

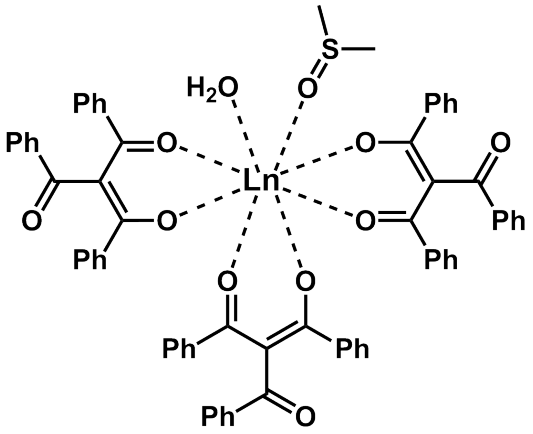

[Sm(**tbm**)$_3$(phen)]

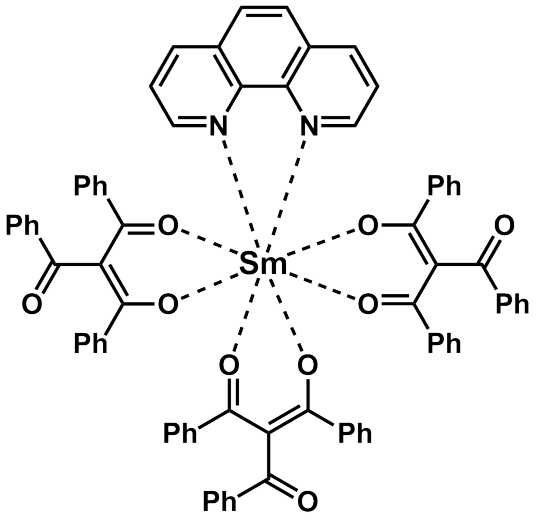

[Ln(**tbm**)$_3$(*d*-phen)]

Ln = Sm^{3+}, Eu^{3+}, Yb^{3+}

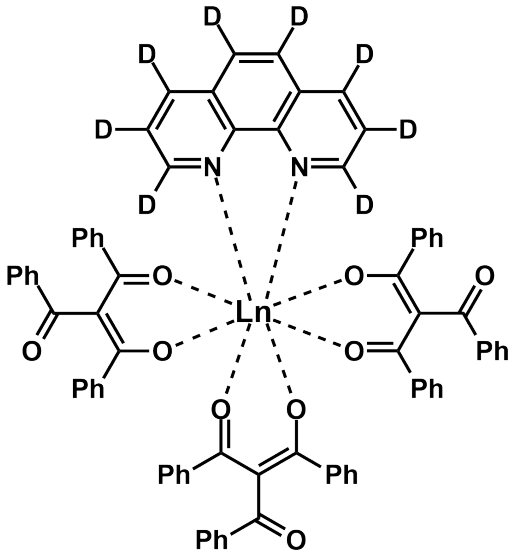

[Ln(**dnm**)$_3$(DMSO)$_2$]

Ln = Nd^{3+}, Sm^{3+}, Eu^{3+}, Gd^{3+}

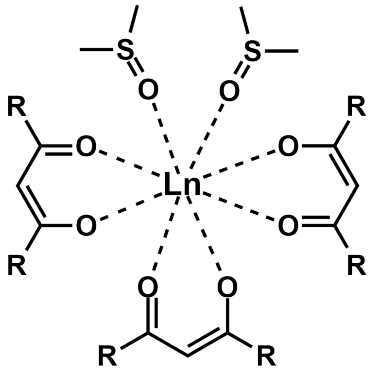

R =

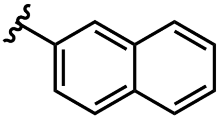

[Sm(**tnm**)$_3$(DMSO)$_2$]

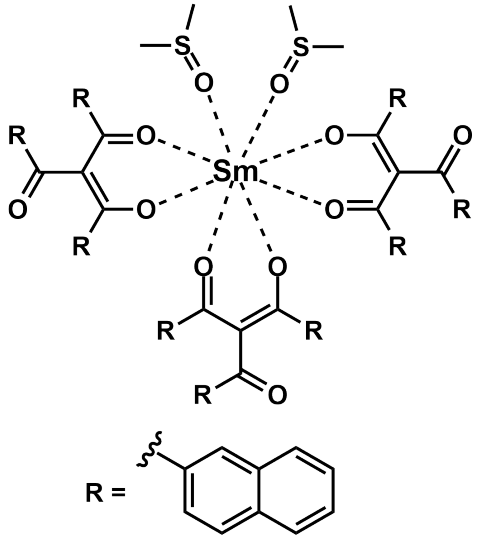

[Ln$_2$(**Bdbm**)$_3$(phen)$_2$]

Ln = Eu^{3+}, Yb^{3+}

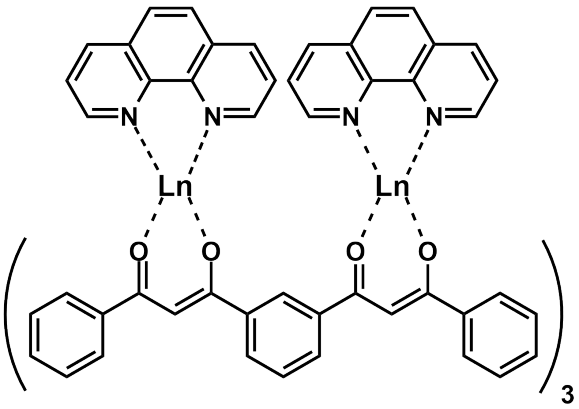

Preface

The lanthanoids, a group of elements commonly denoted with 'Ln' are part of a larger common classification of elements known as rare earth metals.* Rare earth metals consist of the 15 lanthanoids, scandium, and yttrium. While this thesis primarily deals with the lanthanoids, some work was done with yttrium complexes. For simplicity, yttrium is sometimes abbreviated as 'Ln' along with the other lanthanoids.

Many lanthanoids are investigated throughout this thesis. Due to their emissive properties, four lanthanoids (Nd^{3+}, Sm^{3+}, Eu^{3+}, and Yb^{3+}) were consistently used as the focus of this research. Sm^{3+} was also chosen for its use in NMR investigations, as explored in Chapter 6. In Chapter 2, the full series of lanthanoids was used to investigate the change in structure and solvation of *β*-triketonate complexes as the series progresses. In Chapter 4, a Gd^{3+} complex was isolated in order to compare its structural information with a published *β*-triketonate complex. In each chapter some Ln^{3+} complexes are missing from the range listed here, whichwas due to time constraints preventing the successful isolation and analysis of certain Ln^{3+} complexes.

Several ligands and complexes are presented throughout this thesis, all of which are based upon a *β*-diketone backbone and represented by a specific code. As formation of a Ln^{3+} complex using *β*-diketone ligands requires the deprotonation of the α-H, this is incorporated in the ligand designations. For example, the neutral *β*-triketone ligand tribenzoylmethane will be written as **tbm**H, while the deprotonated ketonate form will be written as **tbm**.

Due to time constraints, all RT solution quantum yield measurements presented have only been recorded once and will need to be confirmed with independent experiments in the future. Some solid-state quantum yields were unable to be measured due to time constraints, whereas other solid-state measurements gave values below 0.1% and are not reported.

* a) Cotton, S. A., *Scandium, Yttrium & the Lanthanides: Inorganic & Coordination Chemistry*. Wiley: ***2006***.

b) Eliseeva S. V., Bunzli J.-C. G., Rare earths: jewels for functional materials of the future. *New J. Chem.* **2011,** *35* (6), 1165.

1.0. Introduction

1.1. The Lanthanoids

The lanthanoids are a group of metallic elements with atomic numbers 57-71 (Ln = La-Lu) (Figure 1.1). Ranging from lanthanum to lutetium, they belong to the *f*-block of the periodic table and possess an electronic configuration of [Xe]$4f^n6s^2$ where n = 0-14, with the exceptions of lanthanum, cerium, gadolinium, and lutetium which possess a single *d*-electron ([Xe]$4f^{n-1}$ $5d^16s^2$).[1-3] Lanthanoids typically adopt a trivalent cationic state (Ln^{3+}, [Xe]$4f^n$) as this tends to be their most stable form, however all lanthanoids (bar promethium) have been isolated in oxidation states of +2 , and some can be isolated in oxidations states of +4 (Ce^{4+}).[4-6]

57	58	59	60	61	62	63	64	65	66	67	68	69	70	71
La	Ce	Pr	Nd	Pm	Sm	Eu	Gd	Tb	Dy	Ho	Er	Tm	Yb	Lu
Lanthanum	Cerium	Praseodymium	Neodymium	Promethium	Samarium	Europium	Gadolinium	Terbium	Dysprosium	Holmium	Erbium	Thulium	Ytterbium	Lutetium

Figure 1.1: The lanthanoids arranged as seen in the periodic table.

Although the first lanthanoids were discovered as early as the late 1700s by Carl Arrhenius and Johan Gadolin,[7-8] they were originally thought to have few practical uses. This changed in 1901 when Carl Auer von Welsbach, an Austrian scientist and inventor, filed two patents pertaining to the use of lanthanoids in gas mantles and flint stone production.[9-10] With both inventions still in use today in the form of camping lanterns and ignition sources for lighters, these discoveries sparked interest in the scientific community initiating further research on the lanthanoids.

Now known for their optical and magnetic properties, lanthanoids have helped in the advancement of many technologies and can be found in a range of fields including; magnetism, electronics, lasers, telecommunications, counterfeit technology, catalysis, solar energy conversion materials, and medical applications.[9-18]

1.2. Lanthanoid Characteristics

Interest in lanthanoid research springs from their innate characteristics which arise from the peculiarities associated with their 4*f* subshell. As part of the *f*-block, the electrons occupying the 4*f* subshell are valence in name, but core in nature. Due to the 4*f* orbitals penetrating the [Xe] core, the 4*f* electrons experience a stronger nuclear attraction, resulting in the contraction of the atomic radii.[19] Known as the *lanthanoid contraction*, this effect describes the fact that the lanthanoids have a decreasing atomic radii across the series.[20]

Unlike traditional *d*-metal complexes which are generally no more than hexacoordinate, the lanthanoids can form up to dodecacoordinate complexes, although octa- or nona-coordinate complexes tend to be the most common.[21] This results in a large array of geometrical shapes that can be formed in the primary coordination sphere (Figure 1.2).[22-23]

Figure 1.2: Eight coordinate complex geometries; biaugmented trigonal prism (BTPR), square antiprism (SAPR), and triangular dodecahedron (TDD). Images adapted from Casanova, et al.[23]

From the number of shapes alone this creates a greater variety in structure than is observed in transition metal complexes. However, lanthanoid complexes possess an added layer of complexity. Unlike the structured geometries of transition metals which form from strong orbital interactions between the metal and ligand,[24] direct orbital interaction between the lanthanoid and ligands are limited due to the shielded 4*f* orbitals.[25] Thus, through electrostatic interactions, weakly covalent and labile metal-ligand bonds form, with the overall structural stereochemistry being determined by the coordinating ligands.[25] This causes lanthanoid complexes to have unpredictable coordination geometries that exist between ideal geometric conformations, requiring relatively new shape analysis

methods to determine their geometry.[26] In solution this unpredictability becomes even more pronounced as the ligands can often exchange freely in the coordination sphere of the lanthanoid atom making characterisation of these complexes quite challenging.

1.3. Lanthanoid Photophysics

Emission from the lanthanoids occurs from specific excited states which results in predictable emission bands that range from the ultraviolet (UV) to the near-infrared (NIR) regions of light.[4] Previously, visible emitters such as Eu^{3+} (orange-red), Sm^{3+} (orange-red), and Tb^{3+} (green) were the focus of research due to their use in lasers and light emitting devices (LEDs).[27] However, NIR emitters such as Yb^{3+}, Er^{3+}, and Nd^{3+} are increasingly becoming the subject of interest due to demand from the biomedical industry for light emitters with greater depth penetration.[10, 17, 28]

While the predictable emission bands are quite desirable, they are simultaneously difficult to utilise due to the lanthanoids having an innately poor absorption capability. Absorption in the lanthanoids occurs through forbidden 4*f*-4*f* transitions which can be activated by electric dipole (ED) or magnetic dipole (MD) transitions.[1, 19] Laporte's rule states that for a transition to be allowed, a change in parity must occur. As such, pure ED transitions (odd parity) involving the 4*f* orbitals (odd parity) are forbidden, whereas pure MD transitions (even parity) are allowed.[4, 19] However, interactions between the heavy lanthanoid atom and the ligand field cause the magnetic vector produced by the orbit to interact with the electron spin, culminating in spin-orbit coupling (SOC).[1, 4-5] SOC causes a relaxation of Laporte's rule by introducing states of mixed spin wherein 4*f*-4*f* transitions become allowed as the transitions are no longer pure u→u. As ED transitions are influenced by the ligand field, their intensity is strongly dependent on the symmetry and geometry of the coordination sphere. Denoted as *hypersensitive* transitions, small changes in symmetry or coordination environment can result in the intensity of transitions changing by a factor of up to 200.[1, 15] Despite all this, absorption by the lanthanoid atoms can occur,

however the absorption coefficient of the 4*f*-4*f* transitions is quite low ($\varepsilon < 10$ L mol^{-1} cm^{-1})[29] leading to the requirement of an alternative method for effective excitation.

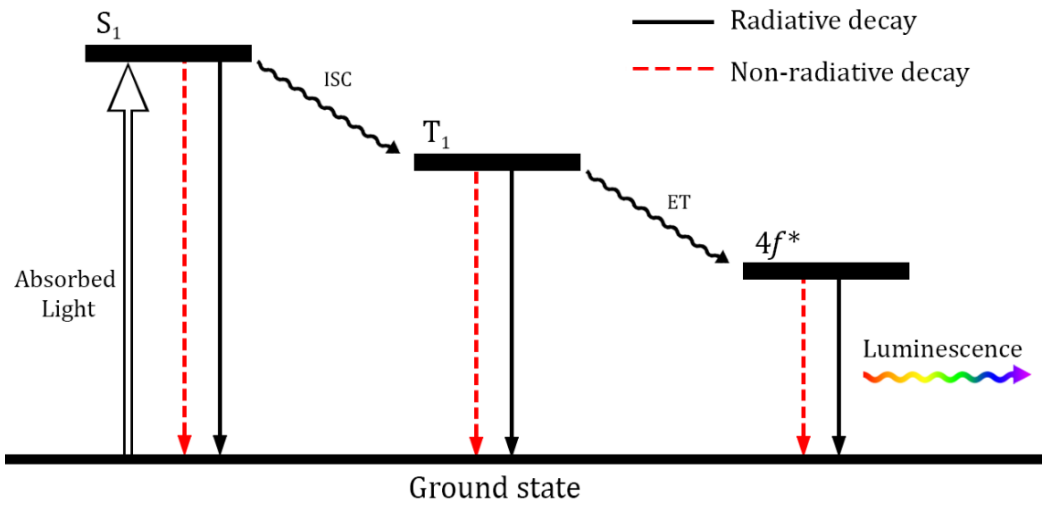

Figure 1.3: Sensitisation pathway utilised by the antenna effect.

The solution to this problem was first discovered by Weissman in 1942[30] and later coined the *antenna effect* by Sabbatini and Lehn.[31-32] This effect describes the indirect sensitisation of the lanthanoid using a coordinated ligand acting as a luminophore (Figure 1.3). In the excitation process, the antenna ligand absorbs light and is excited to a higher electronic level known as the singlet excited state (S_1). Relaxation from the singlet state to the ground state (S_0) can occur *via* radiative or non-radiative pathways, with non-radiative pathways describing every process that does not result in the emission of light. Following Kasha's rule, the molecule will undergo internal conversion (IC) to reach the lowest singlet excited state before further relaxing to the ground state *via* IC. Alternatively, the system may undergo a change in multiplicity and relax to the triplet excited state (T_1) *via* inter-system crossing (ISC). ISC is made possible by the influence of SOC introduced by the heavy lanthanoid atom and corresponding ligand field.[1, 4] From the triplet state, energy may relax to the ground state or undergo an energy transfer (ET) to the lanthanoid excited state (4*f**). As with the singlet and triplet excited states, relaxation of the 4*f** can occur *via* radiative pathways resulting in luminescence, or *via* non-radiative pathways, where the energy is lost non-

emissively. Non-raditiave pathways are commonly referred to as quenching effects, and attempts to minimise them are crucial in designing highly luminescent complexes.[9]

1.4. Quenching Mechanisms

The triplet excited state energy level of the antenna ligand state plays a crucial role in the sensitisation process. While sensitisation can occur from the singlet excited state,[33] it is more likely to occur from the triplet state as it has a longer excited lifetime. The overall efficiency of the ET is reliant upon the energy gap between excited states and the presence of alternative non-radiative pathways. Generally, the lower the energy gap between the triplet excited state and the lanthanoid excited state the more efficient the transfer. However, should the excited states lie too close, the system may undergo a back-energy transfer (BET) to the triplet excited state resulting in decreased emissions. Previous studies have shown that a difference of 2500-3000 cm^{-1} between excited states is required in order to minimise BET whilst maximising efficiency.[4, 34] BET is just one factor that can be responsible for the quenching of luminescent emissions. Other common sources of quenching include cross relaxation and multiphonon relaxation.

Cross relaxation (or concentration quenching) typically occurs at a high density or concentration of Ln^{3+} ions where the energy may transfer from the excited state of one lanthanoid to another. This can occur directly between two lanthanoid ions (distances <8 Å) or be mediated through a ligand (distances >8 Å).[4] Although usually considered a quenching pathway, studies have shown it can be used as a source of sensitisation between two lanthanoid centres.[4, 35]

Multiphonon relaxation refers to the transfer and overall loss of energy to the molecular vibrations of nearby molecular bonds. Vibrational overtones are formed from the molecular vibrations, providing an alternate relaxation pathway that competes with the energy gap of the $4f^* \rightarrow S_0$ transitions (Figure 1.4). Molecular bonds such as O-H, N-H, and C-H are the most common sources of multiphonon relaxation due to their high energy vibrations requiring a minimal

number of overtones to bridge energy gaps.[4-5, 36-37] As fewer vibrational overtones result in a more competitive pathway, preventative measures for multiphonon relaxation typically involve the deuteration,[36-37] perfluorination,[38-40] or complete removal of these bonds. By replacing -H bonds with -D or -F bonds, the vibrational energy of the bond is significantly reduced. This is aptly demonstrated in Figure 1.4 by comparing the vibrational energy of O-H bonds (~3,600 cm^{-1}) and O-D bonds (~2,600 cm^{-1}).[41] In the case of Eu^{3+}, four O-H overtones are required to provide an alternative relaxation pathway, but by replacing the hydrogen with deuterium the number of required overtones increases to six, thus decreasing the favourability of this pathway. NIR emitting lanthanoids such as Yb^{3+} and Nd^{3+} are particularly susceptible to multiphonon relaxation as their energy gap is quite small and only a minimal number of overtones are required to bridge the gap.[4-5]

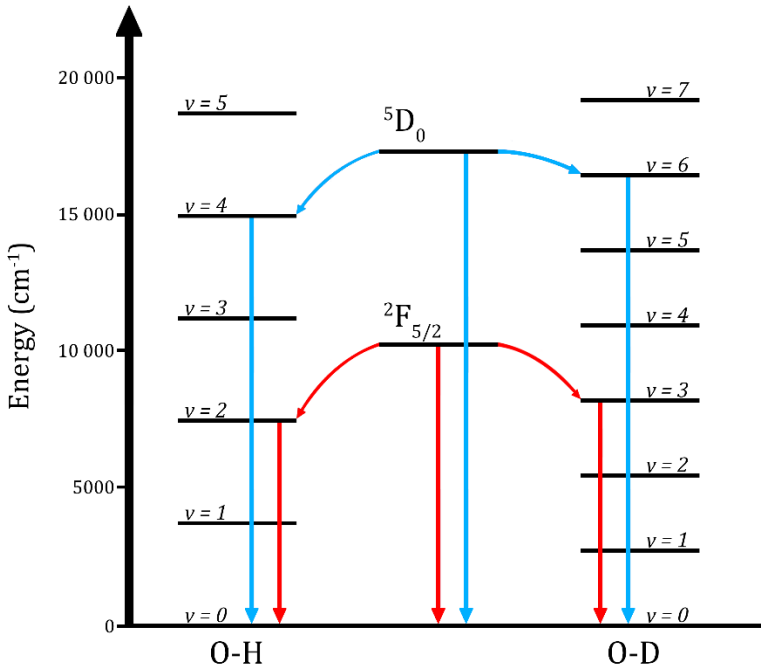

Figure 1.4: Radiative and non-radiative relaxation pathways from Eu^{3+} ($^5D_0$) and Yb^{3+} ($^2F_{5/2}$) excited states via vibrational overtones of O-H and O-D bonds.

1.5. β-Diketonates

When designing antenna ligands, it is important to consider factors such as absorptivity, chelating ability, efficiency of transitions, and potential non-radiative relaxation pathways. Molecules that have been studied for their ability as antenna ligands include β-diketones/ketonates,[40, 42-43] calix[4]arenes,[44-45] cryptates,[46-47], benzoates,[48-49] and multidentate pyridine derivatives[50-53] (Figure 1.5).

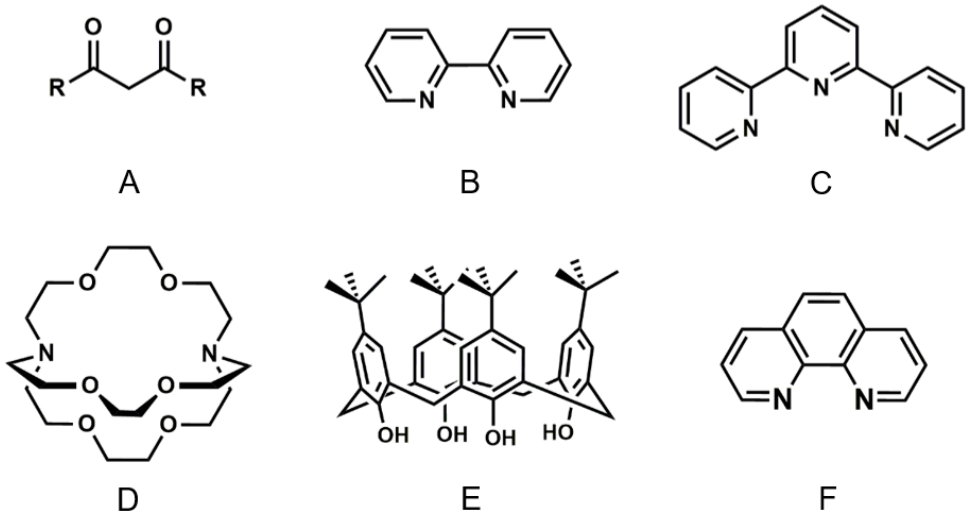

Figure 1.5: Commonly used ligands; β-diketones/ketonates (A), bidentate (B) and tridentate (C) pyridine derivatives, cryptates (D), calix[4]arenes (E), and 1,10-phenanthroline (F).

β-Diketonates in particular have been studied as antenna ligands due to their accessibility and strong chelating ability. Varying the terminal substituents on the carbonyl groups gives access to a wide variety of molecules. Common substituents include akyl, aromatic, or heteroaromatic groups, as well as their deuterated or fluorinated counterparts. Due to the high degree of variety in available substituents leading to varying chemical properties, β-diketonate lanthanoid complexes are well established.[43] Investigations into potential applications have changed over time, from laser light sources in the '60s,[27] to NMR shift reagents in the '70s and '80s.[54] In recent years, applications as catalysts[16] or electroluminescent materials in organic LEDs have been identified.[55-56]

When paired with *β*-diketonate ligands, Ln^{3+} cations typically form octacoordinate tris or tetrakis complexes. In tris complexes, six coordination sites are occupied by three bis-chelating *β*-diketonate ligands, while the remaining coordination sites are filled by monodentate solvent molecules or Lewis bases such as 1,10-phenanthroline (phen) and 2,2'-bipyridine (Figure 1.5).[4-5, 43] On the other hand, tetrakis complexes feature four *β*-diketonate ligands, utilising a cationic species to counteract the negative charge of the extra *β*-diketonate ligand.[57-58]

Owing to the variety of potential complexes formed through changes in substituents, there has been a resurgence in structural investigations of lanthanoid *β*-diketonate complexes. Alongside the tris and tetrakis complexes mentioned above, *β*-diketonates are capable of supporting clusters, ranging from as low as three or four metal ions to over fourteen ions contained within a single molecular cluster.[43, 59-61] In these systems, keto-oxygen atoms often act as bridges between two Ln^{3+}, with additional aqua or hydroxo ligands supporting the formation of the cluster. It has been found that the formation of tetra- or penta-nuclear assemblies can be dependent on the size of the Ln^{3+} ion, with the larger lanthanoids (La^{3+} – Eu^{3+}) forming pentanuclear assemblies and the smaller lanthanoids (Eu^{3+} – Yb^{3+}) forming tetranuclear assemblies.[61]

1.6. *β*-Triketonates

More recently, literature has been published on the *β*-triketonates, a family of molecules that had previously only seen a brief period of investigation in the '60s.[62-64] A natural extension of the *β*-diketonates, these studies started investigating the *β*-triketonates for use as sensitising ligands in NIR emitting lanthanoid complexes.[4-5, 12, 65-67] This led to the discovery of a family of lanthanoid complexes featuring different structural motifs including mononuclear complexes, tetranuclear assemblies, and coordination polymers.[4-5, 35, 66] The tetranuclear assemblies featured two Ln^{3+} and two alkali metal cations, maintaining a consistent structure throughout a range of different metals with Yb^{3+} forming the sole exception.[68] These assemblies were made possible by

bridging β-triketonates that would bis chelate to one Ln^{3+} while the third keto-O atom coordinated to a second metal ion (Figure 1.6). Photophysical analysis of these assemblies revealed long lifetimes and improved luminescent quantum yields relative to typical β-diketonate complexes. However, they had issues with solubility, proving insoluble in water and other common organic solvents. While this hindered their use for fundamental photophysical studies, the assemblies were just soluble enough for photophysical measurements in ethanol or methanol, allowing solution studies at room temperature (RT) and at 77 K to take place.[66, 68]

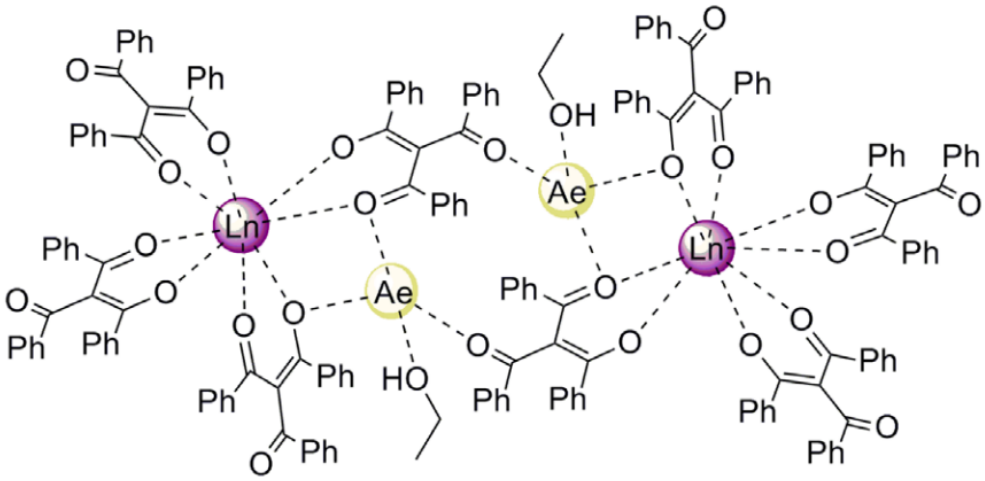

Figure 1.6: Bimetallic tetranuclear assembly formed by two lanthanoids (Ln = Gd^{3+}, Tb^{3+}, Dy^{3+}, Ho^{3+}), two alkali metal cations (Ae = Na^{+}, K^{+}, Rb^{+}) and β-triketonates. Reproduced with permission from Reid et al.[65]

In order to better understand the photophysical properties of the lanthanoid β-triketonate complexes, the solubility issues of the tetranuclear assemblies needed to be addressed. This was achieved by turning to mononuclear complexes, which showed increased solubility in organic solvents. While mononuclear complexes were isolated in the process of the previous investigations they were not intensively studied as the focus was on the tetranuclear assemblies. Preliminary investigations on the mononuclear β-triketonate complexes showed photophysical properties that were an improvement on their β-diketonate counterparts, but not quite as good as the assemblies.[4, 67] The mononuclear complexes were typically synthesised in alcoholic conditions with the addition of

phen to prevent the coordination of water or other solvents with high energy vibrational bonds. This method remained in use until retro-Claisen condensation reactions were observed in the alcoholic solutions, resulting in the isolation of complexes with both β-diketonate and β-triketonate ligands.[4] To prevent this from happening different solvent systems were trialled, culminating in the formation of DMSO solvated complexes which proved to possess photophysical properties equal to those of the tetranuclear assemblies, but with the advantage of solubility in organic solvents.[4, 69] However, the DMSO coordinated complexes were only isolated with trinaphthoylmethane (**tnm**H), as opposed to the tribenzoylmethane (**tbm**H) ligand used for the phen coordinated complexes. It is known that increased conjugation leads to lower triplet excited states which can, in turn, lead to a more efficient energy transfer.[42] Hence it was unknown whether the improved luminescent properties exhibited by the DMSO solvated complexes was due to the replacement of the benzoyl groups with the naphthoyl groups, or the replacement of phen with DMSO.

1.7. Overview

This body of work aims to continue the investigation into the DMSO solvated complexes, as well as the overarching investigation into optimising the photophysical properties of NIR emitting complexes utilising β-triketonate ligands. Each chapter will explore the structural and photophysical properties of the different complexes isolated throughout the duration of this work. Multiple lanthanoids have been used in this research, however emphasis for the photophysical studies will be placed on Nd^{3+}, Sm^{3+}, Eu^{3+}, and Yb^{3+} for comparisons between the visible and NIR emitters. Crystal X-ray diffraction studies will be done in tandem so as to provide detailed structural information that can be related to the resulting photophysical properties.

Chapter 2 explores the coordination of DMSO in tribenzoylmethane (**tbm**H, Figure 1.7) complexes.

Chapter 3 analyses the effect phen has on the luminescent properties of β-triketonate complexes, including looking at the impact of the deuteration of phen.

Chapter 4 examines the differences between the β-di- and β-tri-ketonates by comparing a series of di- and tri-naphthoylmethane (**dnm**H, **tnm**H, Figure 1.7) DMSO solvated complexes.

Chapter 5 presents the synthesis of a new ligand, bis-tribenzoylmethane (**Btbm**H_2, Figure 1.7), as well as the first crystal structure of a lanthanoid complex utilising bis-dibenzoylmethane (**Bdbm**H_2, Figure 1.7).

Lastly, Chapter 6 will investigate the use of NMR spectroscopy to probe the behaviour of lanthanoid complexes in solution, in an effort to complement photophysical studies of the lanthanoid complexes in solution.

This research is presented with the intent of broadening the field of β-triketonate chemistry, with particular emphasis on their use as antenna ligands for efficient NIR emitting lanthanoid complexes.

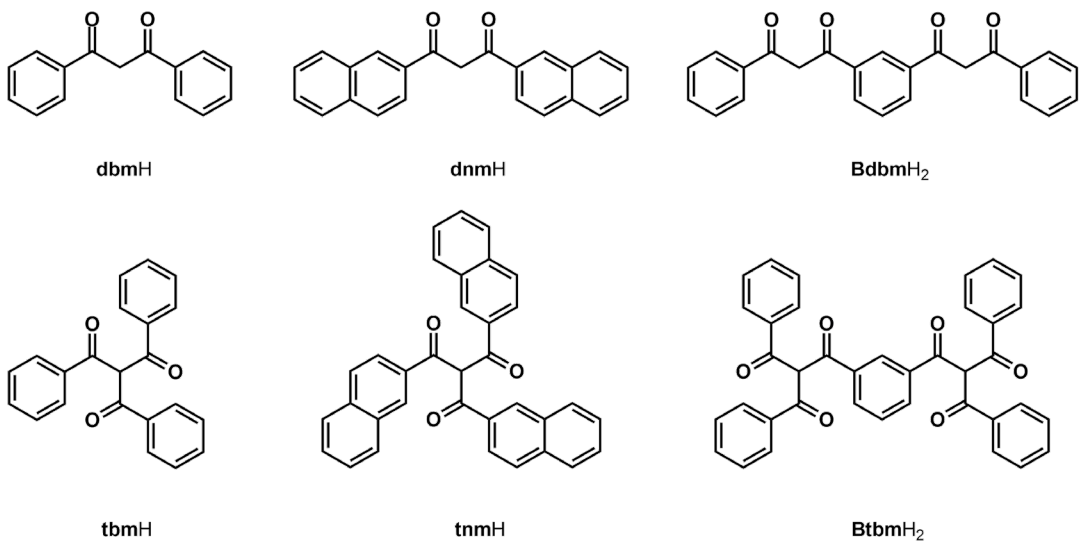

*Figure 1.7: Ligand molecules presented in this body of work. Dibenzoylmethane (**dbm**H), dinaphthoylmethane (**dnm**H), bis-dibenzoylmethane (**Bdbm**H_2), tribenzoylmethane (**tbm**H), trinaphthoylmethane (**tnm**H), bis-tribenzoylmethane (**Btbm**H_2)*

2.0. DMSO Solvated Complexes

2.1. Introduction

This chapter focuses on the synthesis and analysis of solvated tribenzoylmethane (**tbm**H) complexes. This will include X-ray diffraction studies, shape analysis of the coordination sphere, and photophysical characterisation.

In order to compare against a previously reported series of triketonate complexes with the formulae [Ln(**tbm**)$_3$(phen)] and [Ln(**tnm**)$_3$(DMSO)$_2$], the target of this research was to isolate a series of complexes with the formula [Ln(**tbm**)$_3$(DMSO)$_2$]. It is hoped that by investigating the co-ligands used alongside antenna ligands, new methods for improved sensitisation in lanthanoid complexes can be developed. The **tbm**H complexes presented in this body of work possess the general formula of [Ln(**tbm**)$_3$(DMSO)(X)], where Ln = La^{3+}, Pr^{3+}, Sm^{3+}, Eu^{3+}, Tb^{3+}, Dy^{3+}, Er^{3+}, Yb^{3+}, Lu^{3+}, Y^{3+}; and X = DMSO, EtOH, or H_2O.

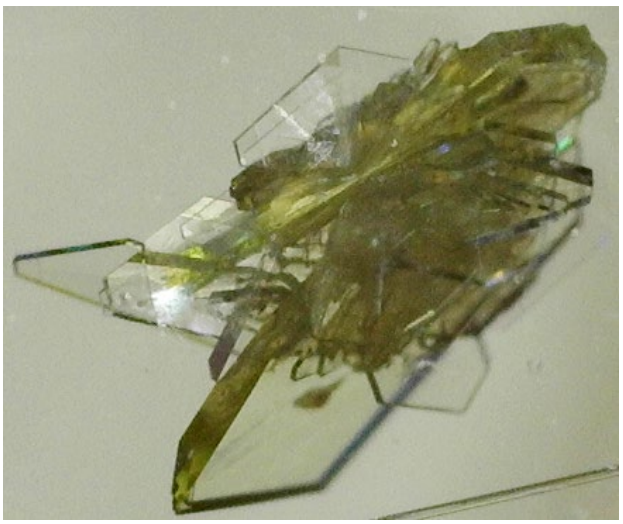

*Crystals of [Sm(**tbm**)$_3$(DMSO)$_2$]*

2.2. Synthesis

Following a previously reported procedure,[12] **tbm**H was successfully synthesised in consistently high yields (75 – 85%) from **dbm**H using sodium hydride and benzoyl chloride in diethyl ether (see Section 8.3 for experimental and spectroscopic data).

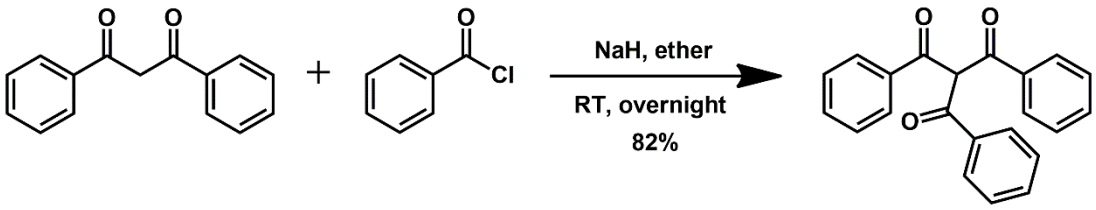

*Scheme 2.1: Synthetic pathway for the isolation of **tbm**H from **dbm**H.*

Using **tbm**H, the Ln^{3+} complexes were synthesised through two different methods as detailed in Sections 8.4.1. and 8.4.2. These methods followed previously reported procedures,[69] with modifications in reaction conditions to allow the growth of single crystals for analysis *via* X-ray diffraction.

The majority of the DMSO solvated complexes were isolated using a layered solvent system where **tbm**H was combined with a Ln^{3+} salt and triethylamine (NEt_3) in a minimal amount of DMSO. Ethanol (EtOH) was slowly added to the system forming a separate layer atop the DMSO. Sealing the system and allowing the two solvents to mix resulted in the formation of crystals after a few days, although it was sometimes necessary to allow the solvent to slowly evaporate to encourage crystal formation.

The target complex of [Ln(**tbm**)$_3$(DMSO)$_2$] was only isolated twice, (for Ln = La^{3+}, Sm^{3+}) with both methods utilising a solvent mixture of DMSO:EtOH (1:1) layered wth diethyl ether. This suggested that the presence of diethyl ether was a requirement for bis-DMSO solvation, however these results were difficult to replicate, possibly because of the high volatility of diethyl ether.

2.3. Structural Analysis

All complexes presented in this chapter were octacoordinate, possessing three bis-chelating **tbm** ligands along with two monodentate solvent ligands. These complexes can be split into three series based upon the solvent ligands coordinated. The target complex with two DMSO ligands, [Ln(**tbm**)$_3$(DMSO)$_2$], and the two more commonly isolated variants with one DMSO ligand and one H_2O or EtOH ligand; [Ln(**tbm**)$_3$(DMSO)(EtOH)] and [Ln(**tbm**)$_3$(DMSO)(H_2O)]·(EtOH). Selected inter- and intra- molecular distances are presented in Tables 2.1, 2.2, and 2.3 (see Tables A1, A2, and A3 in Appendix 10.4.1. for individual bond lengths). Despite multiple attempts to grow the bis-DMSO solvated complex, the EtOH and H_2O solvated complexes proved to be the more favoured compositions. Originally, it was thought that coordination of the second solvent molecule was dictated by the size of the lanthanoid, however the formation of [Ln(**tbm**)$_3$(DMSO)(EtOH)] for the largest (La^{3+}) and smallest (Lu^{3+}) lanthanoids disproved this hypothesis.

DMSO-DMSO Complexes

The two bis-DMSO solvated complexes are shown in Figure 2.1. While the coordination complexes are similar, the crystal packing is different with the La^{3+} complex crystallising as a triclinic system, whereas the Sm^{3+} complex is monoclinic (see Section 8.5. for details).

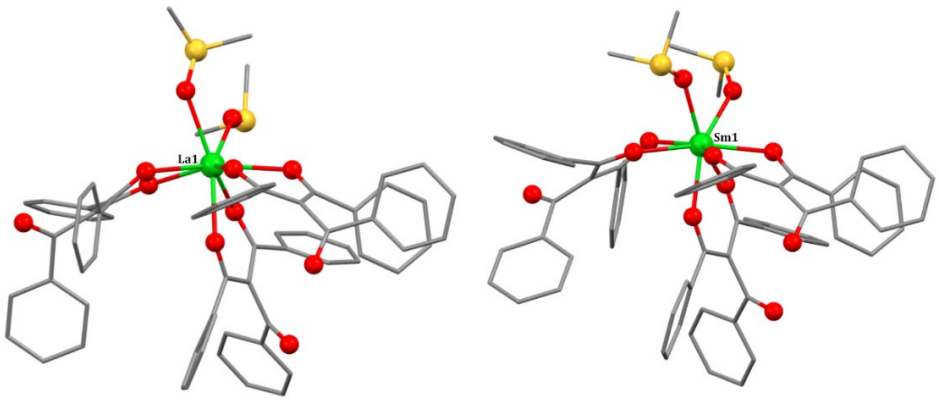

*Figure 2.1: Crystal structures of [Ln(**tbm**)$_3$(DMSO)$_2$] for La^{3+} (left) and Sm^{3+} (right). Hydrogen atoms omitted for clarity.*

A decrease in Ln-O bond distances was observed between the La^{3+} (2.436 (2) – 2.530 (2) Å) and Sm^{3+} (2.363 (1) – 2.410 (2) Å) complexes as expected given the reduction in ionic radius of Sm^{3+} compared to La^{3+}.[70] The closest metal to metal distance in the La^{3+} complex was measured at 10.222 (6) Å while the Sm^{3+} complex featured a longer distance of 10.384 (6) Å.

*Table 2.1: Selected inter- and intra- molecular distances (Å) of [Ln(**tbm**)$_3$(DMSO)$_2$] (Ln = La^{3+}, Sm^{3+}). Refer to Figures 2.1 and 2.2 for crystal structures. See Table A1 in Appendix 10.4.1. for individual bond lengths.*

Complex	Ln – O	Ln – Ln
[La(**tbm**)$_3$(DMSO)$_2$]	2.436 (2) – 2.530 (2)	10.222 (6)
[Sm(**tbm**)$_3$(DMSO)$_2$]	2.363 (1) – 2.410 (2)	10.384 (1)

Structural changes in Ln^{3+} complexes with the same ligands across the series are not uncommon, with the transition commonly occurring around the central lanthanoids (Sm^{3+} to Gd^{3+}).[71-74] With only two examples of these complexes characterised to date, it is not possible to determine the structural trends in this series at this point.

DMSO-EtOH Complexes

The EtOH solvated complexes isolated as triclinic systems with two distinct monomers forming based upon the size of the Ln^{3+} (Figure 2.2). The most notable difference between the structures was the altered orientation of the EtOH ligand allowing for different intermolecular interactions between different monomers. Changes in the first coordination sphere were observed, leading to different structural geometries, however this will be discussed in more detail in Section 2.4.2.

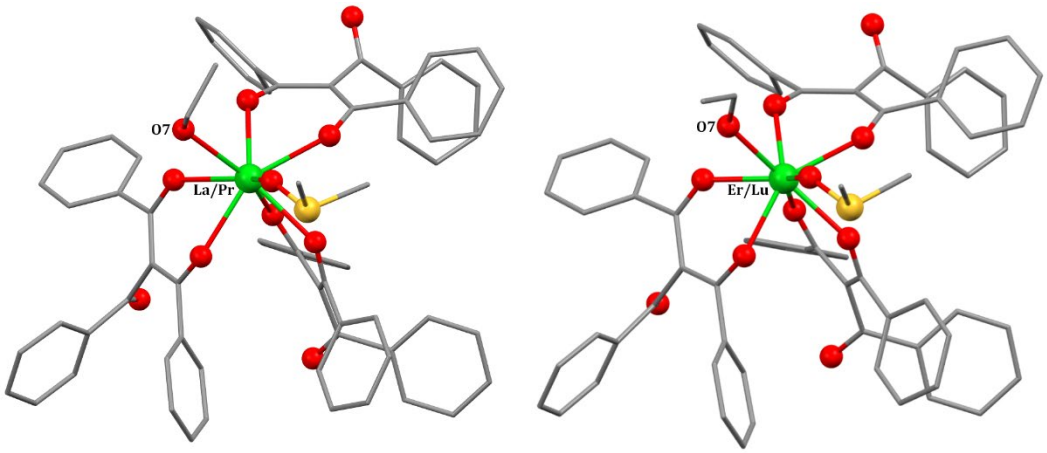

*Figure 2.2: Crystal structures of [Ln(**tbm**)$_3$(EtOH)] for Ln = La^{3+}, Pr^{3+} (left), Ln = Er^{3+}, Lu^{3+} (right). Hydrogen atoms omitted for clarity.*

The Ln-O bond lengths maintained a consistent decrease across the series, starting from 2.454 (3) – 2.577 (5) Å for the La^{3+} complex and decreasing to 2.255 (3) – 2.346 (3) Å for the Lu^{3+}. The Ln-Ln distances averaged around 9.90 (2) Å, proving shorter than the bis-DMSO complexes suggesting a tighter packing of the crystal lattice. Similar to the bis-DMSO complexes, the smaller lanthanoids had longer intermolecular distances compared to the larger lanthanoids; however, this is likely due to differences in the crystal packing forces caused by the two structural orientations.

*Table 2.2: Selected inter- and intra- molecular distances (Å) of [Ln(**tbm**)$_3$(DMSO)(EtOH)] (Ln = La^{3+}, Pr^{3+}, Er^{3+}, Lu^{3+}). Refer to Figure 2.2 for crystal structures. See Table A2 in Appendix 10.4.1. for individual bond lengths.*

Complex	Ln – O	Ln – Ln
[La(**tbm**)$_3$(DMSO)(EtOH)]	2.454 (3) – 2.577 (5)	9.880 (6)
[Pr(**tbm**)$_3$(DMSO)(EtOH)]	2.413 (2) – 2.538 (3)	9.888 (6)
[Er(**tbm**)$_3$(DMSO)(EtOH)]	2.287 (2) – 2.377 (2)	9.939 (6)
[Lu(**tbm**)$_3$(DMSO)(EtOH)]	2.255 (3) – 2.346 (3)	9.899 (7)

DMSO-H_2O Complexes

Unlike the other DMSO solvated complexes, the H_2O solvated complexes formed a supramolecular dimer about an inversion centre, evidenced by the H-bonds between the aqua ligand and the uncoordinated keto-O atom of a **tbm** ligand (Figure 2.3). EtOH molecules could be seen throughout lattice forming H-bonds with the third uncoordinated keto-O of the **tbm** ligands. The series of H_2O complexes maintained the expected trend of decreasing Ln-O bond distances, starting from Eu^{3+} as the largest and finishing with Yb^{3+} as the smallest.

*Table 2.3: Selected inter- and intra- molecular distances (Å) of [Ln(**tbm**)$_3$(DMSO)(H_2O)]·(EtOH) (Ln = Eu^{3+}, Tb^{3+}, Dy^{3+}, Yb^{3+}, Y^{3+}). Refer to Figure 2.3 for crystal structure. See Table A3 in Appendix 10.4.1. for individual bond lengths.*

Complex	Ln – O	Ln – Ln
[Eu(**tbm**)$_3$(DMSO)(H_2O)]·(EtOH)	2.340 (1) – 2.462 (2)	8.717 (5)
[Tb(**tbm**)$_3$(DMSO)(H_2O)]·(EtOH)	2.317 (2) – 2.434 (2)	8.624 (5)
[Dy(**tbm**)$_3$(DMSO)(H_2O)]·(EtOH)	2.312 (2) – 2.431 (2)	8.643 (5)
[Yb(**tbm**)$_3$(DMSO)(H_2O)]·(EtOH)	2.267 (2) – 2.384 (2)	8.626 (5)
[Y(**tbm**)$_3$(DMSO)(H_2O)]·(EtOH)	2.289 (1) – 2.412 (2)	8.621 (6)

Y^{3+} is an interesting case, while it does not belong to the *f*-block, it possesses similar chemical properties to the lanthanoids allowing them to be classified together under the label, rare earths.[75] Y^{3+} has an ionic radius similar to Ho^{3+} placing it towards the end of the series.[75] With this understanding, it can be concluded that the Ln-O bond lengths of Y^{3+} fit the expected trend. The Ln-Ln distances also decreased across the series and were smaller than the bis-DMSO and EtOH complexes, likely due to the dimer formation. All Ln-Ln distances were above 8 Å however, suggesting that cross relaxation issues should be negligible.

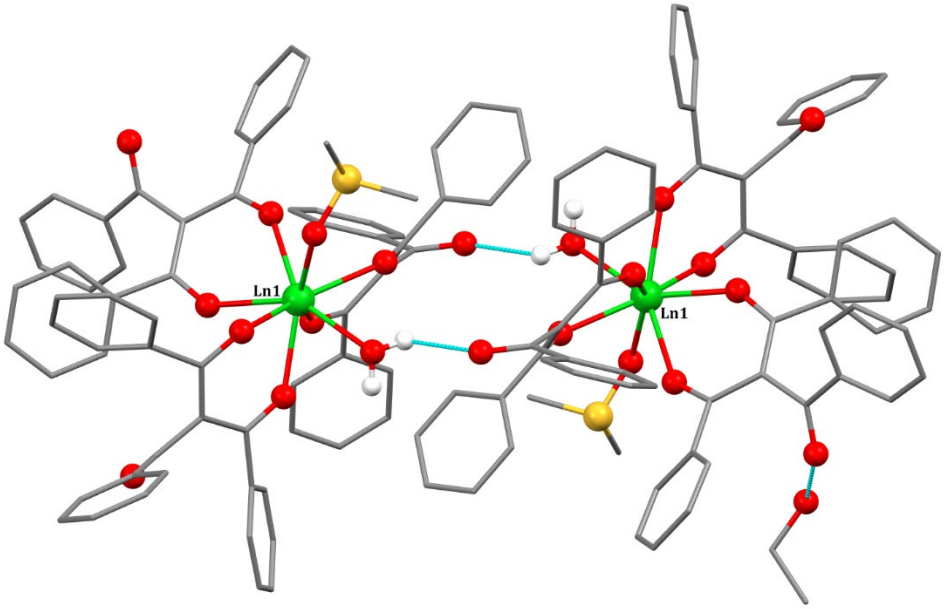

*Figure 2.3: Crystal structure of [Ln(**tbm**)$_3$(DMSO)(H$_2$O)]·(EtOH) (Ln = Eu^{3+}, Tb^{3+}, Dy^{3+}, Yb^{3+}, Y^{3+}). Hydrogen bonds are highlighted in cyan. Hydrogen atoms other than on water omitted for clarity.*

2.4. Shape Analysis

2.4.1. CShM Theory

The geometry of a lanthanoid complex plays a vital role in its emissive properties, as variations in the ligand field affect the forbidden or allowed nature of their 4*f*-4*f* transitions.[1, 3] Due to this, an analysis of the first coordination sphere of each complex presented in this thesis will be carried out in order to ascertain potential effects on their luminescent properties.

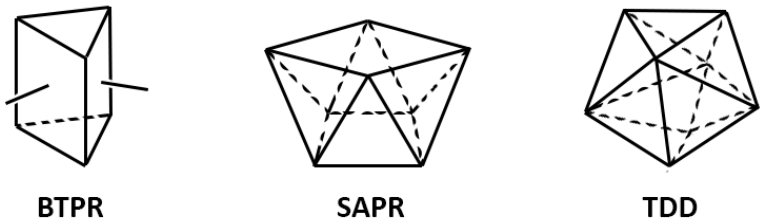

Figure 2.4: Ideal polyhedron geometries discussed in this body of work. Biaugmented Trigonal Prism (BTPR), Square Antiprism (SAPR), and Triangular Dodecahedron (TDD). Images adapted from Casanova et al.[23]

Thanks to work by Zabrodsky *et al.*[76] it is possible to identify the deviation of a given complex from an 'ideal' geometry (Figure 2.4) using a series of calculations that follow Eq. 2.1. In this equation, P represents the polyhedron to be analysed with its characteristic position vectors (Q_i) and vertex atoms (N). The position of the vertices and geometrical centre of the desired polyhedron are represented by P_i and Q_0. The smallest positional difference between the given polyhedron and all ideal polyhedra is measured, giving a CShM number that decreases in value the closer the polyhedron is to an ideal polyhedron. Therefore, a theoretically ideal polyhedron would have a CShM(P) value of 0.

$$\mathrm{CShM}(P) = min\frac{\sum_{i=1}^{N}|Q_i - P_i|^2}{\sum_{i=1}^{N}|Q_i - Q_0|^2}100 \qquad \text{Eq. 2.1}$$

Analysis of the complexes using Eq. 2.1 was simplified using Shape Version 2.1 software developed by Casanova *et al.*[23, 26] that uses Eq. 2.1 to generate *CShM*(P) values of a given polyhedron. The program is also capable of generating a shape map that identifies the lowest energy interconversion pathway (LEIP) between two ideal polyhedra by plotting CShM values on the x and y-axis. Shape maps will be used throughout this thesis to compare the extent of deviation experienced by a given complex from two ideal polyhedra and the LEIP that exists between them.

2.4.2. Analysis of Tribenzoylmethane Complexes

All of the bis-solvated complexes adhered most closely to the octacoordinate polyhedra of a square antiprism (SAPR), triangular dodecahedron (TDD), or biaugmented trigonal prism (BTPR). Their relative CShM values are presented in Table 2.4, while a comparison of these values and their related LEIP is visualised *via* shape maps in Figures 2.5 and 2.6.

Table 2.4: CShM values for the complexes presented in this chapter.

Complex	BTPR	SAPR	TDD
[La(**tbm**)$_3$(DMSO)$_2$]	1.727	--	1.891
[Sm(**tbm**)$_3$(DMSO)$_2$]	1.907	--	0.487
[La(**tbm**)$_3$(DMSO)(EtOH)]	1.037	--	1.747
[Pr(**tbm**)$_3$(DMSO)(EtOH)]	0.994	--	1.554
[Er(**tbm**)$_3$(DMSO)(EtOH)]	1.259	--	0.916
[Lu(**tbm**)$_3$(DMSO)(EtOH)]	1.283	--	0.859
[Eu(**tbm**)$_3$(DMSO)(H$_2$O)]·(EtOH)	--	0.685	1.623
[Tb(**tbm**)$_3$(DMSO)(H$_2$O)]·(EtOH)	--	0.543	1.622
[Dy(**tbm**)$_3$(DMSO)(H$_2$O)]·(EtOH)	--	0.670	1.496
[Yb(**tbm**)$_3$(DMSO)(H$_2$O)]·(EtOH)	--	0.613	1.471
[Y(**tbm**)$_3$(DMSO)(H$_2$O)]·(EtOH)	--	0.670	1.450

As expected from the structural changes observed previously, the bis-DMSO solvated complexes exhibited varying degrees of distortion. Both complexes were closest in shape to a BTPR or TDD, however the La^{3+} had relatively equal CShM values (BTPR = 1.727, TDD = 1.891) leading to a high degree of distortion overall. Comparatively, the Sm^{3+} complex lay far closer to a TDD (0.487) in shape than a BTPR (1.907) resulting in a more ordered shape.

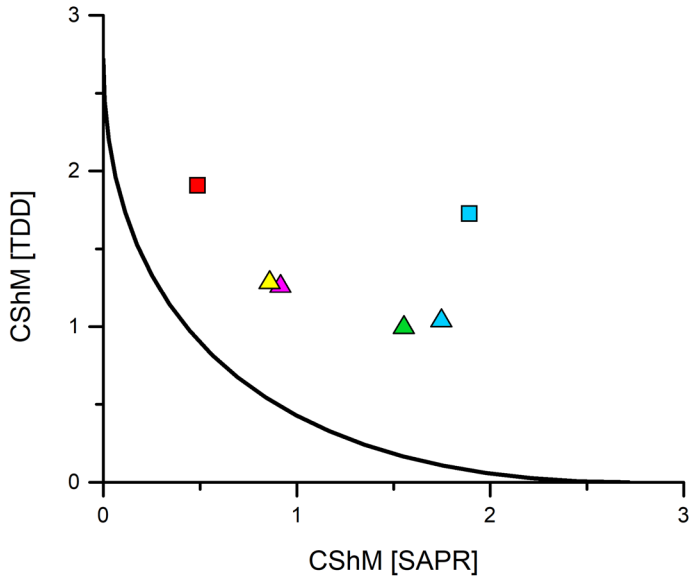

*Figure 2.5: Shape map of [Ln(**tbm**)$_3$(DMSO)$_2$] (square) and [Ln(**tbm**)$_3$(DMSO)(EtOH)] (triangle) for Ln = La^{3+} (blue), Pr^{3+} (green), Sm^{3+} (red), Er^{3+} (magenta), and Lu^{3+} (yellow).*

Similar to the bis-DMSO complexes, the EtOH solvated complexes lay closest to a BTPR or TDD in shape and showed varying degrees of distortion based upon the two structures identified in the previous section. The larger Ln^{3+} complexes (La^{3+} and Pr^{3+}) lay closer to a BTPR with CShM values around 1, whereas the smaller Ln^{3+} complexes (Er^{3+} and Lu^{3+}) were closer to a TDD with CShM values around 0.9. Given the lower overall CShM values and the proximity to the LEIP it can be concluded that the smaller Ln^{3+} complexes display less distortion than the larger Ln^{3+} complexes.

The H_2O solvated complexes showed a consistent degree of distortion, matching the consistent structural shape previously identified (Figure 2.6). All five complexes lay closest to a SAPR in shape ranging from 0.685 (Eu^{3+}) to 0.543 (Tb^{3+}). A general trend could be seen where the smaller the ionic radius of the Ln^{3+}, the more ordered the resulting complex was.

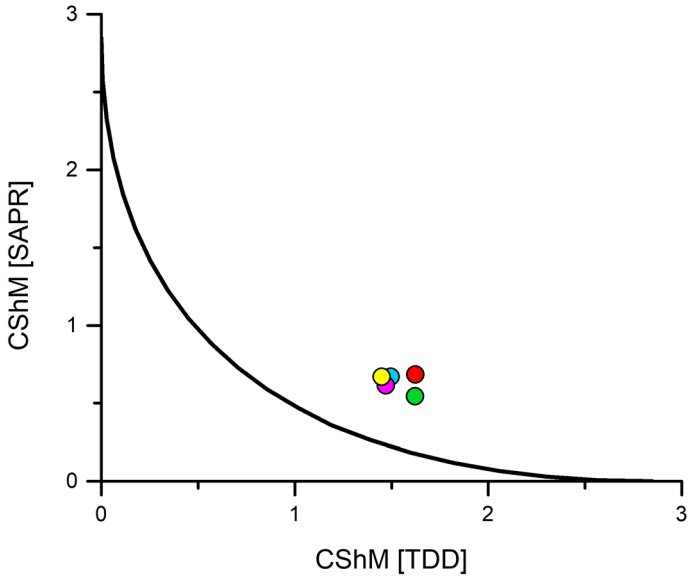

*Figure 2.6: Shape map of [Ln(**tbm**)$_3$(DMSO)(H_2O)]·(EtOH) for Ln = Eu^{3+} (red), Tb^{3+} (green), Dy^{3+} (blue), Yb^{3+} (magenta), and Y^{3+} (yellow).*

2.5. Photophysical Characterisation

The triplet state of the deprotonated antenna ligand **tbm** was previously reported by Reid, *et al.*[12] to lie at ~20,704 cm^{-1}. This value was based upon the phosphorescent 0-phonon transition from a Gd^{3+} complex at 77 K. Only the Eu^{3+} and Yb^{3+} complexes were analysed for their luminescent properties as sensitisation of their excited states (~19,000 cm^{-1} and ~10,200 cm^{-1} respectively) should occur with a minimal chance of BETs occurring.

All complexes were measured in the solid-state and in an acetonitrile (MeCN) solution at room temperature (RT) and at 77 K. The luminescent lifetime (τ_{obs}) and overall photoluminescent quantum yield (Φ_{Ln}^{L}) of the complexes presented in this chapter are shown below in Table 2.5. Measurement of the solid-state quantum yield for the Eu^{3+} complex was unachievable due to time constraints, while measurements for the Yb^{3+} gave values below 0.1% and are not reported.

*Table 2.5: Photophysical data of [Ln(**tbm**)$_3$(DMSO)(H$_2$O)]·(EtOH) for Ln = Eu^{3+} and Yb^{3+}.*

Complex	Medium	τ_{obs} (μs)	Φ_{Ln}^{L}(%)
[Eu(**tbm**)$_3$(DMSO)(H$_2$O)]·(EtOH)	Solid-state	269	--
	RT (MeCN)	166	0.1
	77 K (MeCN)	322 (42%) 526 (58%)	--
[Yb(**tbm**)$_3$(DMSO)(H$_2$O)]·(EtOH)	Solid-state	9	--
	RT (MeCN)	32	4.0
	77 K (MeCN)	16	--

[Eu(tbm)$_3$(DMSO)(H$_2$O)]·(EtOH)

Eu^{3+} is most known for its vibrant red-orange emission arising from the $^5D_0 \rightarrow {}^7F_J$ (J = 0 – 4) transitions which appear around 580, 590, 615, 650, and 720 nm respectively (Figure 2.7).[15, 77] Emission from the $^5D_0$ can also occur from transitions to two more J states of $^7F_5$ (~750 nm) and $^7F_6$ (~820 nm), however these transitions are typically quite weak and in the case of $^7F_6$ exist outside the limit of detection for the visible detector employed. The $^5D_0 \rightarrow {}^7F_2$ transition is a hypersensitive ED transition making it highly sensitive to changes in the

coordination environment.[77] Although dependent on the environment, this transition typically possesses the greatest intensity and is overall responsible for the strong red-orange emission of Eu^{3+} complexes. Although emission occurs from the $^5D_0$ state, direct excitation of this state is rare and it is typically excited through internal conversion from the $^5D_1$ state. This process means that the sensitisation of Eu^{3+} has a threshold of ~19,000 cm^{-1} ($^5D_1$), compared to the expected ~17,200 cm^{-1} ($^5D_0$).[19] Although the energy gap between the $^5D_1$ excited state and the ketonate ligands used in this work indicate that non-radiative BET pathways should be accessible, a publication by Sato and Wada indicated that an energy gap of ~1,500 cm^{-1} is sufficient for efficient sensitisation of the $^5D_1$ state.[42]

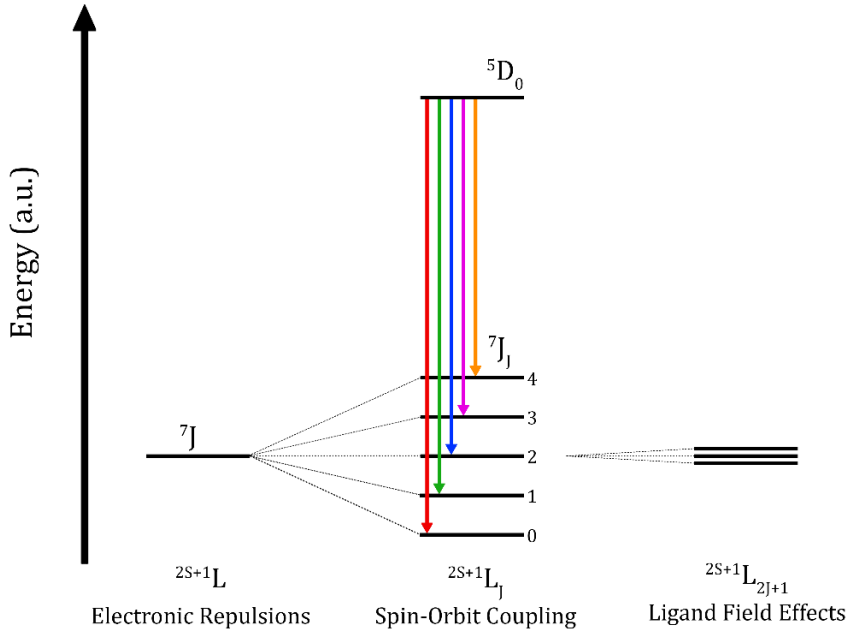

Figure 2.7: Energy level diagram of Eu^{3+}.

The characteristic emission bands of Eu^{3+} can be seen in the emission spectra of [Eu(**tbm**)$_3$(DMSO)(H_2O)]·(EtOH) leading to the conclusion that sensitisation of the metal centre is effective (Figure 2.8). The J splitting observed in the solid-state measurement proved significantly different to the solution phase measurements, with the peak at 615 nm resulting from the $^5D_0 \rightarrow {}^7F_2$ transition showing a three-way split compared to a smoothened single peak in the solution measurements. This is a commonly seen phenomenon in Ln^{3+} complexes, and it occurs due to the loss of structural rigidity in solution allowing for movement in

the coordination sphere, consequently affecting the emissive properties. A shift is seen in the excitation spectra between the solid-state and solution measurements as well, however this is a typical occurrence in lanthanoid complexes and can occur due to the loss of rigidity upon dissolution, or aggregation in the solid-state broadening the excitation bands. The sharp peaks seen in the solid-state excitation spectra around 460 nm could arise from direct excitation of the Eu^{3+} atom, or from the excitation light source, a Xe arc-lamp, which is known to cause sharp peaks in that region.[78]

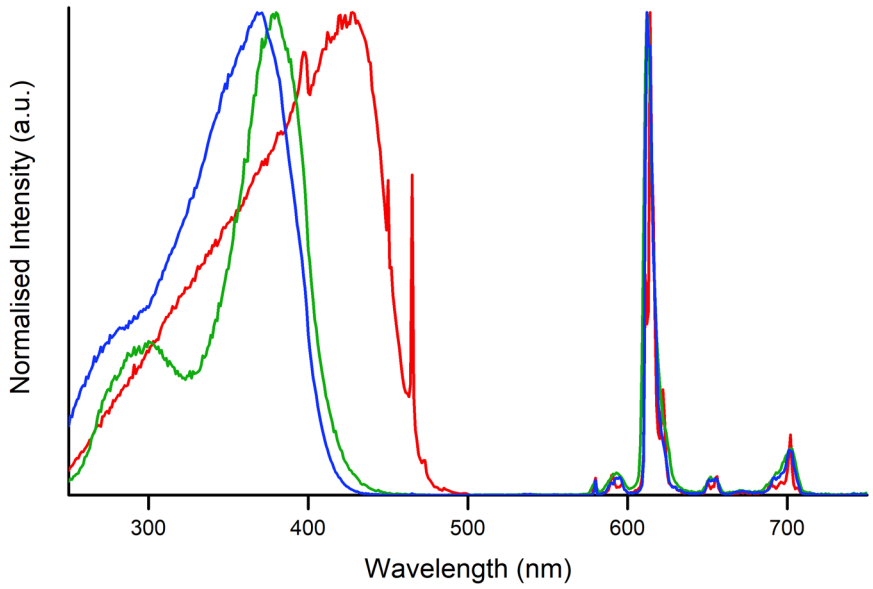

*Figure 2.8: Excitation and emission spectra of [Eu(**tbm**)$_3$(DMSO)(H$_2$O)]·(EtOH) in the solid-state (red trace, λ_{ex} = 420 nm), a MeCN solution at RT (green trace, λ_{ex} = 380 nm), and a MeCN solution at 77 K (blue trace, λ_{ex} = 380 nm). λ_{em} = 615 nm.*

Both the solid-state and RT solution possessed mono-exponential lifetimes of 269 µs and 166 µs respectively (Figure 2.9). Comparitively, the 77 K measurement was bi-exponential ranging from 322 µs (42%) to 526 µs (52%). The quantum yield for the RT solution measurements was 0.1%, the low value being indicative of quenching effects caused by the presence of H_2O and EtOH.

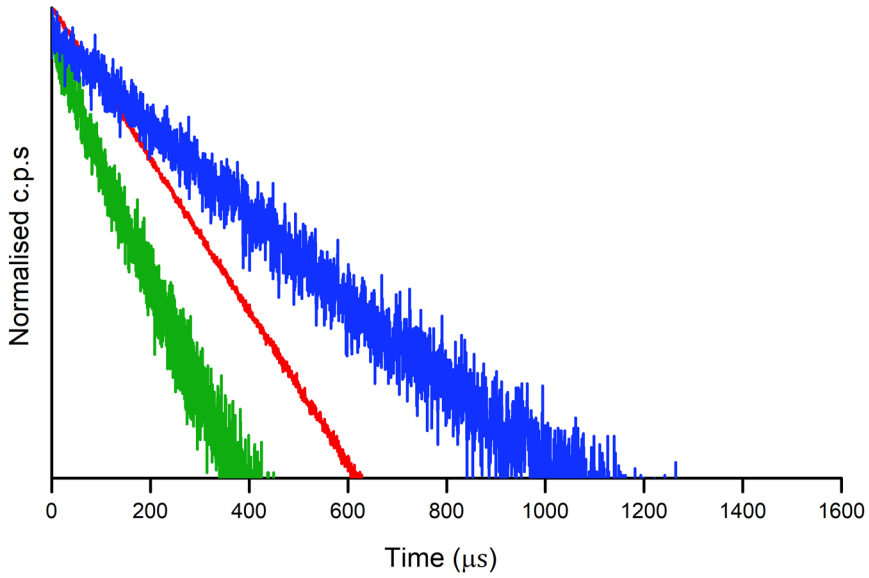

*Figure 2.9: Lifetime decay of [Eu(**tbm**)$_3$(DMSO)(H$_2$O)]·(EtOH) in the solid-state (red trace, λ_{ex} = 420 nm), a MeCN solution at RT (green trace, λ_{ex} = 380 nm), and a MeCN solution at 77 K (blue trace, λ_{ex} = 380 nm).*

[Yb(tbm)$_3$(DMSO)(H$_2$O)]·(EtOH)

Ytterbium possesses a single emissive excited state, $^2F_{5/2}$ (~10,200 cm^{-1}), resulting in the appearance of a single broad emission band. This peak corresponds to the $^2F_{5/2} \rightarrow {}^2F_{7/2}$ transition and appears in the NIR region around 980 – 1050 nm (Figure 2.10). Under ligand field influences, further splitting of the energy states may occur, culminating in Stark states of 2J+1 with a splitting value no greater than 10^2 cm^{-1}.[3] However, as Yb^{3+} possesses an odd electron configuration ($4f^{13}$) it can be classified as a Kramer's ion, meaning any states formed from the ligand field effects will be doubly degenerate, with the maximum number of states equalling J + ½.[3] Following this rule, four doubly degenerate states will be observed which correspond to the four-fold peak splitting occasionally seen within the emission band of Yb^{3+} spectra.

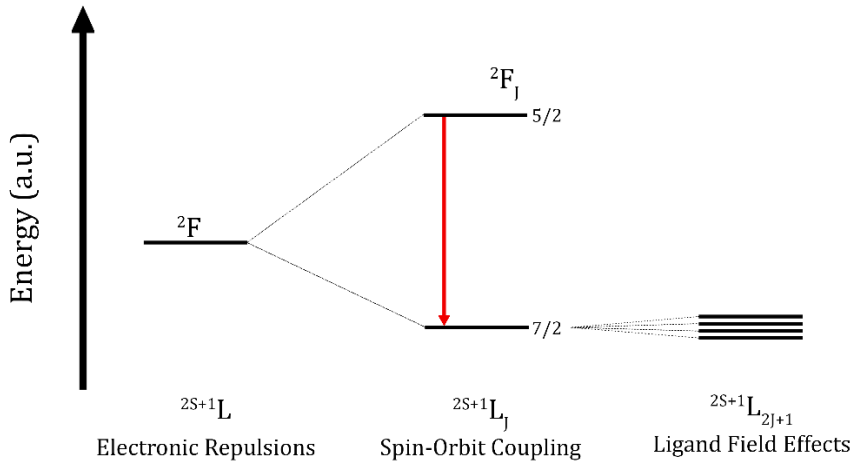

Figure 2.10: Energy level diagram of Yb^{3+}.

The emission spectra of [Yb(**tbm**)$_3$(DMSO)(H$_2$O)]·(EtOH) presents the characteristic emission bands of Yb^{3+} confirming that sensitisation *via* **tbm** was successful (Figure 2.11). As with the previous Eu^{3+} complex, a shift in peak maxima can be seen in the solid-state excitation spectra. A number of sharp peaks can be seen in the 77 K excitation spectrum, potentially arising from heavily distorted geometries adopted by the complex upon freezing of the solution. Emission from the solid-state occurred as a broad band showing no trace of peak splitting from ligand field effects which comes as little surprise given the complexes proximity to an ideal polyhedron as determined by the CShM value (SAPR = 0.613). Comparatively, the 77 K measurement displayed the highest degree of splitting with a separation of three peaks at 977, 997, and 1029 nm while the RT solution showed a single sharp peak at 977 nm and a broadened plateau extending to 1025 nm. Both of these splitting patterns suggest the complex changes its geometry upon dissolution resulting in a shape with more overall disorder. The broadened baseline of the solid-state and room temperature measurements are a result of thermal energy populating varying Stark states, resulting in broader emission bands. Cooling to 77 K mostly prevents the thermal population of these states resulting in sharper peaks.

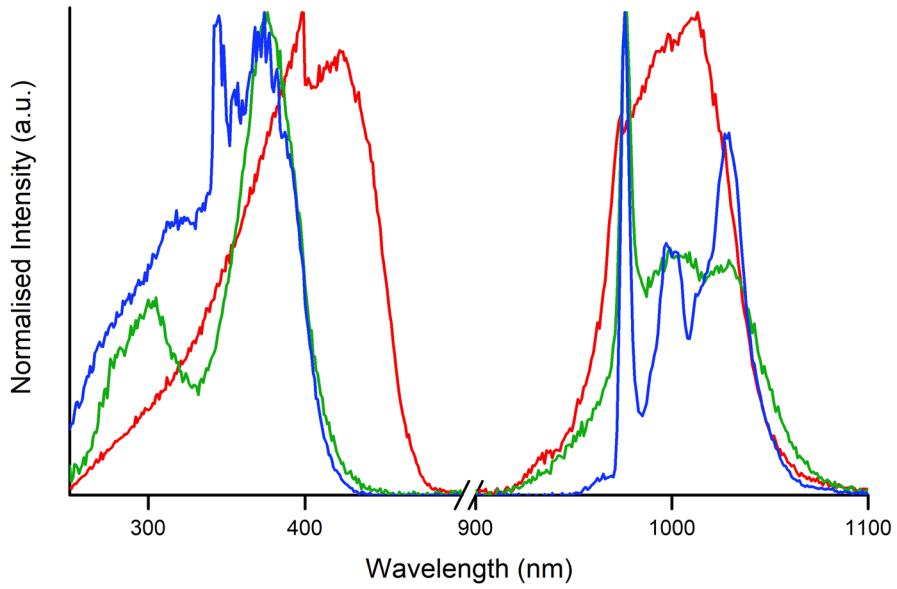

*Figure 2.11: Excitation and emission spectra of [Yb(**tbm**)$_3$(DMSO)(H$_2$O)]·(EtOH) in the solid-state (red trace), a MeCN solution at RT (green trace), and MeCN solution at 77 K (blue trace). λ_{ex} = 375 nm, λ_{em} = 977 nm.*

The solid-state, RT solution, and 77 K measurements gave mono-exponential lifetimes, with values of 9 µs, 32 µs, and 16 µs, respectively. A quantum yield of 4.0% was recorded for the RT solution, however no reportable value could be obtained for the solid-state. Despite the presence of H_2O and EtOH in the complex, the RT solution measurement proved to have an unusually high quantum yield and lifetime for a Yb^{3+} complex, which were consistent over multiple measurements. A previously reported [Yb(**tbm**)$_3$(phen)] complex gave lifetime and quantum yield values in a RT DCM solution of 18 µs and 1.16%, whereas [Yb(**dbm**)$_3$(phen)] had even lower values of 13 µs and 0.87%.[67] Given the distinct difference in lifetime and quantum yield of these complexes, it can be hypothesised that phen may have a greater influence on luminescent properties than previously thought.

2.6. Summary

Eleven new lanthanoid β-triketonate complexes were presented in this chapter, each possessing three **tbm** and two solvent ligands. The aim of this research, to isolate complexes with the formula [Ln(**tbm**)$_3$(DMSO)$_2$] and study their photophysical properties, was partially achieved through the formation of La^{3+} and Sm^{3+} complexes. However, the isolation of bis-DMSO solvated complexes proved more difficult than expected, with the majority of isolated complexes containing one DMSO ligand, and one H_2O or EtOH ligand. Both bis-DMSO and DMSO-EtOH solvated complexes presented different crystalline structures based upon the size of their Ln^{3+}. Whilst relatively consistent bond lengths were maintained, varying degress of distortion were observed. Comparitively, the H_2O complexes formed an isostructural series for Ln = Eu^{3+}, Tb^{3+}, Dy^{3+}, Yb^{3+}, and Y^{3+}, presenting a relatively low degree of distortion. From the isolated complexes, it appears that the H_2O monomer is favoured for the central to smaller Ln^{3+} while the EtOH monomer is favoured for the extremities of the series.

The photophysics of the Eu^{3+} and Yb^{3+} complexes were analysed with both showing the expected emission bands of their respective Ln^{3+} ions. The Eu^{3+} complex gave an extremely low quantum yield as expected from the close proximity of O-H bonds to the metal centre. However, the Yb^{3+} complex presented unexpected results, revealing a lifetime for the RT solution that was not only greater than the solid-state and 77 K measurements, but also from other literature examples. Similarly, the quantum yield of the RT solution proved higher than literature examples despite the presence of O-H bonds which typically result in increased multiphonon relaxation pathways and decreased quantum yields.

While the overall aim of isolating bis-DMSO solvated complexes did not come to fruition, this work isolated a different range of Ln^{3+} complexes that presented their own questions to be answered. Currently, it is difficult to conclude whether the formation of the H_2O or EtOH solvated complexes is determined by ionic radius due to the conflicting information presented. Isolating complexes of a wider range of lanthanoids may provide an understanding of the factors influencing solvation, but based on the results to date, it seems likely that subtle

changes in the reaction conditions may have a greater impact than the ionic radius of the complex. In the case of the bis-DMSO complexes, it can be concluded that their formation was a more challenging task than first imagined. While proven possible by the isolation of the La^{3+} and Sm^{3+} complexes, neither synthetic method proved repeatable or reliable hindering further studies. However, both synthetic methods utilised diethyl ether in some manner which provides a point of reference for future work into this area. Another avenue for future work should include the use purified and dried DMSO alongside anhydrous reaction conditions. In doing so, the possibility of water coordinating will be reduced leading to a potentially more reliable isolation method for bis-DMSO complexes.

3.0. 1,10-Phenanthroline Complexes

3.1. Introduction

The main focus for this area of research was to determine whether phen negatively impacts the luminescent properties of di- and tri- ketonate lanthanoid complexes. This was achieved through two pathways; the comparison of [Sm(**dbm**)$_3$(phen)]·(EtOH) and (HNEt$_3$)[Sm(**dbm**)$_4$]·(EtOH) to explore the replacement of phen with a fourth **dbm** ligand, and comparisons between complexes with the formula [Ln(**tbm**)$_3$(phen)] and [Ln(**tbm**)$_3$(*d*-phen)] (Ln = Sm^{3+}, Eu^{3+}, Yb^{3+}), where *d*-phen is deuterated phenanthroline. Deuteration of molecules is known to reduce the favourability of non-radiative relaxation pathways due to the replacement of high energy oscillators (O-H, C-H) with oscillators of lower energy (O-D, C-D).[36-37] Therefore, should phen be affecting the photophysical properties of these complexes then a change should be observed.

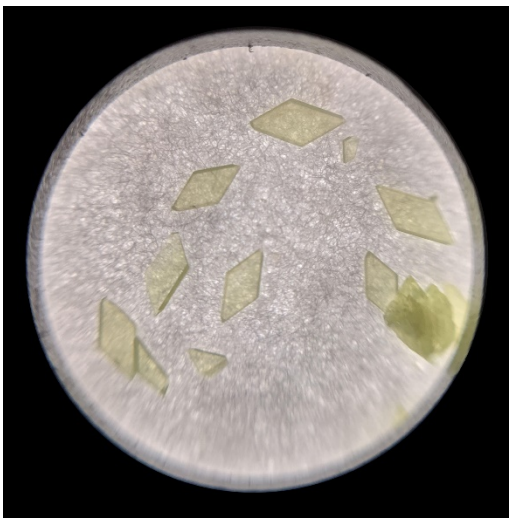

*Crystals of [Sm(**tbm**)$_3$(phen)]*

3.2. Synthesis

The [Ln(**tbm**)$_3$(phen)] and [Ln(**tbm**)$_3$(*d*-phen)] (Ln = Sm^{3+}, Eu^{3+}, Yb^{3+}) complexes were synthesised following a previously reported procedure (see Section 8.4.2. for experimental and spectroscopic information).[67] Single crystals were reliably grown by combining the ligands (**tbm**H, phen or *d*-phen) with a Ln^{3+} salt, and NEt_3 in hot ethanol and stirring with heating for 30 minutes, before filtering the hot solution and allowing it to slowly evaporate over several days or weeks. Overall yields for the *d*-phen complexes were quite poor, ranging from 8 – 10%, although this increased to 32% for [Sm(**tbm**)$_3$(phen)] and 72% for [Y(**tbm**)$_3$(phen)].

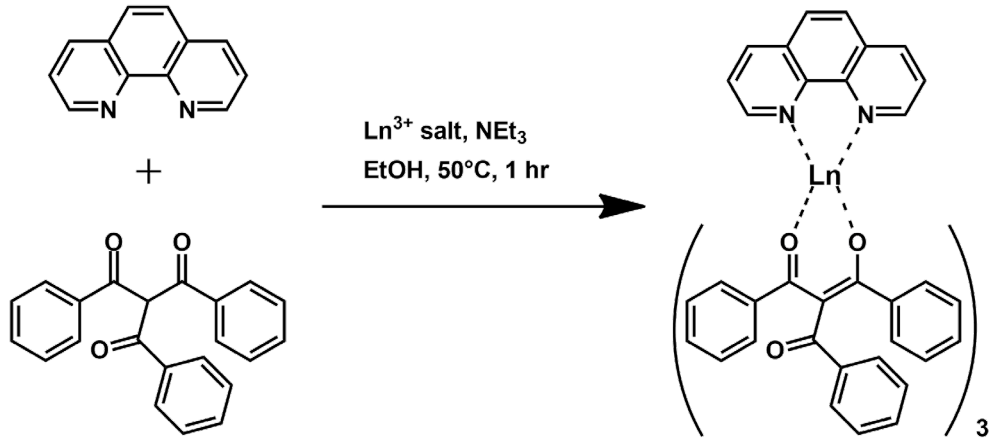

*Scheme 3.1: Synthetic pathway for the isolation of [Ln(**tbm**)$_3$(phen)]*

The isolation of (HNEt$_3$)[Sm(**dbm**)$_4$]·(EtOH) was serendipitous, resulting from a reaction where the intended product was [Sm(**dbm**)$_3$(DMSO)$_2$]. A literature investigation revealed that the method used to isolate this complex was very similar to the procedures used by Akerboom, *et al.*[58] and Hollerman, *et al.*[79] to reliably produce anionic complexes. To provide a point of comparison, the [Sm(**dbm**)$_3$(phen)] complex was then synthesised using the same procedure as the **tbm** complexes. Prior to the isolation of the anionic complex, crystallisation attempts using the evaporation method for bis-DMSO solvated complexes relied on the salt Ln(NO$_3$)$_3$(DMSO)$_4$ to provide the DMSO ligands. In subsequent experiments, excess DMSO was added to reactions with the intent of obtaining bis-DMSO solvated complexes over anionic complexes.

3.3. Structural Analysis

3.3.1. Dibenzoylmethane Complexes

Both **dbm** complexes were octacoordinate. For $(HNEt_3)[Sm(\mathbf{dbm})_4]\cdot(EtOH)$, all donor atoms were provided by the keto-O atoms of the **dbm** ligands, whereas two of these keto-O atoms were replaced by the N atoms from phen for $[Sm(\mathbf{dbm})_3(phen)]\cdot(EtOH)$. Selected inter- and intra- molecular distances for these complexes are shown in Table 3.1. An overall decrease of Sm-O bond lengths was observed in the phen coordinated complex compared to the anionic complex. The presence of four charged ligands vs three charged and one neutral ligand could cause the discrepancy between the bond lengths, where the charged ligands will have a stronger attraction to the metal centre, thus displacing the less attracted phen molecule. Comparitively the four charged molecules would result in more consistent bond lengths as no ligand would possess a greater force of attraction than the others.

Table 3.1: Selected inter- and intra- molecular distances (Å) of $(HNEt_3)[Sm(\mathbf{dbm})_4]\cdot(EtOH)$ and $[Sm(\mathbf{dbm})_3(phen)]\cdot(EtOH)$. Refer to Figures 3.1 and 3.2 for crystal structures. See Table A4 in Appendix 10.4.2. for individual bond lengths.

$(HNEt_3)[Sm(dbm)_4]\cdot(EtOH)$			**$[Sm(dbm)_3(phen)]\cdot(EtOH)$**	
Measurement	**Sm1**	**Sm2**	**Measurement**	**Sm1**
Sm – O	2.40 (2)*	2.40 (3)*	Sm – O	2.304 (9)*
Sm – N	--	--	Sm – N	2.547 (1)*
Sm – Sm	23.699 (7)	14.440 (7)	Sm1 – Sm1	11.3 (5)*
Sm1 – Sm2	14.1 (8)*		--	--

** Denotes averaged values.*

The complex $(HNEt_3)[Sm(\mathbf{dbm})_4]\cdot(EtOH)$ formed two symmetrically independent but similar monomers (Figure 3.1). Coordination of the four **dbm** ligands resulted in an anionic complex where the negative charge of the fourth **dbm** ligand is offset by the positive charge of a triethylammonium molecule seen forming a hydrogen bond at O11 or O82 in each monomer. A lone EtOH molecule was seen throughout the crystal lattice forming a hydrogen bond to O51 in the

Sm2 monomers. Three different Sm1-Sm2 distances were identified (13.006 (7), 14.389 (7), and 15.011 (7) Å), alongside different Sm1-Sm1 (23.699 (7) Å) and Sm2-Sm2 (14.440 (7) Å) distances. Given all metal-metal distances were above 8 Å, non-radiative relaxation *via* concentration quenching should be prevented. The Sm-O distances identified for this complex (2.364 (4) – 2.448 (3) Å) were near identical to those of a previously isolated complex ($HNEt_3$)[Sm(**dbm**)$_4$] (2.358 (4) – 2.421 (3) Å)[58] suggesting that the presence of the EtOH does not have a significant impact on the first coordination sphere.

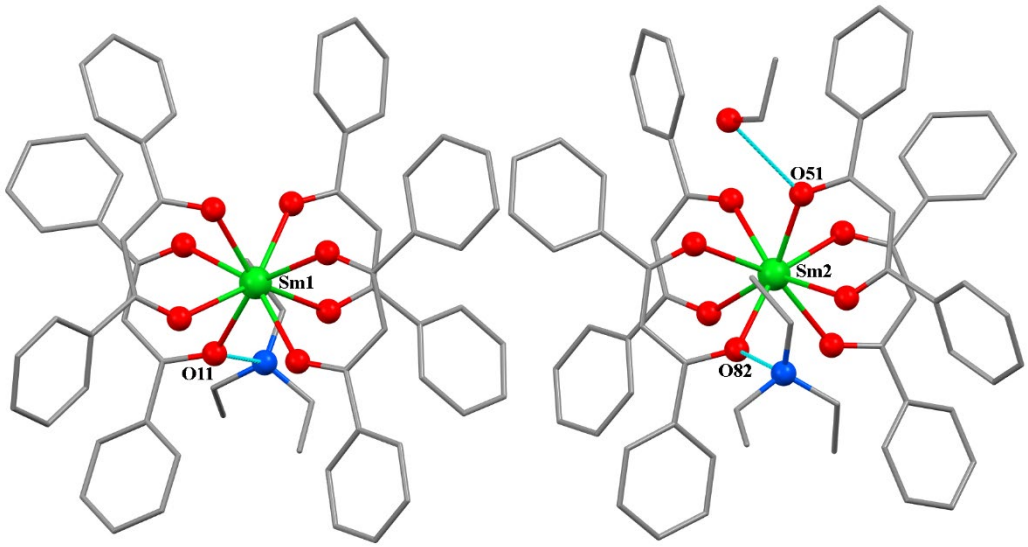

*Figure 3.1: Crystal structure of ($HNEt_3$)[Sm(**dbm**)$_4$]·(EtOH). Hydrogen bonds are highlighted in cyan. Hydrogen atoms omitted for clarity.*

Unlike the anionic complex, the crystal structure of [Sm(**dbm**)$_3$(phen)]·(EtOH) featured a single unique monomer (Figure 3.2). Three different metal-metal distances of 10.594 (3) Å, 11.442 (7) Å, and 11.888 (5) Å were found throughout the crystal. As all distances were above 8 Å, it suggests that cross-relaxation pathways will be prevented. An EtOH molecule can be seen forming a hydrogen bond with O21 in each complex. Although usually present in phen coordinated complexes, no π – π stacking was observed in this system.[80]

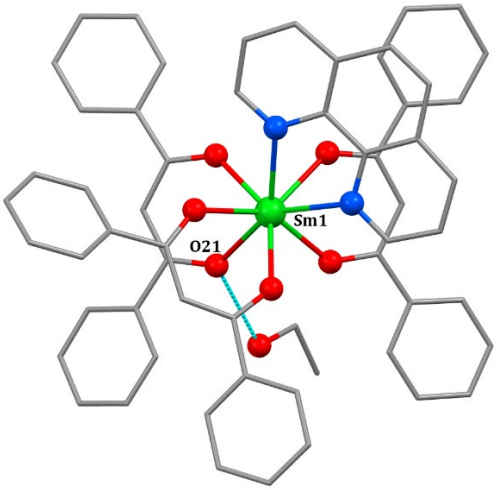

*Figure 3.2: Crystal structure of [Sm(**dbm**)$_3$(phen)]·(EtOH). Hydrogen bonds are highlighted in cyan. Hydrogen atoms omitted for clarity.*

The average Sm-O and Sm-N distances proved to be shorter than those of a previously characterised EtOH free [Sm(**dbm**)$_3$(phen)] complex,[81] with the average distances of each shown in Table 3.2. There is no clear indication as to what caused this decrease in bond lengths, however it could be reasoned that the presence of EtOH altered the geometry of the complex, resulting in decreased bond lengths. The result of this will be explored further as part of the shape analysis in chapter 3.3.2. Overall it is expected that the decreased bond lengths and presence of EtOH will influence the luminescent properties of the complex.

*Table 3.2: Average Sm-O and Sm-N bond lengths for the two [Sm(**dbm**)$_3$(phen)] complexes.*

	Experimental	**Literature[81]**
Sm – O	2.30 (1)	2.37 (2)
Sm – N	2.547 (1)	2.66 (3)

3.3.2. Tribenzoylmethane Complexes

The [Ln(**tbm**)$_3$(phen/*d*-phen)] (Ln = Sm^{3+}, Eu^{3+}, Yb^{3+}, Y^{3+}) complexes were octacoordinate, with six coordination sites occupied by keto-O atoms of the **tbm** ligands and the remaining two by the N atoms of phen (Figure 3.3). Each new complex presented here proved isostructural to the previously reported

[Ln(**tbm**)$_3$(phen)] (Ln = Eu^{3+}, Yb^{3+}),[67] with selected molecular distances shown in Table 3.3. Due to time constraints, [Sm(**tbm**)$_3$(*d*-phen)] was unable to be structurally characterised via x-ray diffraction crystallography. However, the IR spectra for both the deuterated and non-deuterated complexes showed similarities indicative of isostructural complexes. The photophysical properties of these complexes also support the isostructural nature of these species, as explored in a later section.

*Table 3.3: Selected inter- and intra- molecular distances (Å) of the [Ln(**tbm**)$_3$(phen/d-phen)] (Ln = Sm^{3+}, Eu^{3+}, Yb^{3+}, Y^{3+}) complexes. Refer to Figure 3.3 for crystal structure. See Table A5 in Appendix 10.4.2. for individual bond lengths.*

Complex	Ln – O*	Ln – N*	Ln – Ln	π – π	Centroid – Centroid
[Sm(**tbm**)$_3$(phen)]	2.37 (2)	2.608 (1)	9.241 (6)	3.257	3.395
#[Eu(**tbm**)$_3$(phen)]	2.36 (2)	2.593 (9)	9.251 (6)	3.292	3.602
[Eu(**tbm**)$_3$(*d*-phen)]	2.35 (2)	2.59 (1)	9.237 (6)	3.250	3.392
#[Yb(**tbm**)$_3$(phen)]	2.278 (2)	2.51 (1)	9.214 (6)	3.256	3.588
[Yb(**tbm**)$_3$(*d*-phen)]	2.28 (2)	2.51 (1)	9.206 (8)	3.238	3.410
[Y(**tbm**)$_3$(phen)]	2.31 (2)	2.54 (1)	9.236 (6)	3.243	3.400

* *Denotes averaged values.*
\# *Experimental data in accordance with literature.*[67]

The crystal lattice is constructed from supramolecular dimers, oriented around an inversion centre formed through π – π stacking between the phen ligands (Figure 3.3). On average the Ln-N bond distances were ~0.24 Å larger than the Ln-O distances and a consistent decrease was seen in all inter- and intra-molecular distances as the metal centre decreased in size. A slight decrease for intramolecular bond lengths was observed between the *d*-phen and phen complexes, although the difference is negligible when factoring in error margins. As each complex possessed Ln-Ln distances greater than 8 Å, a loss of energy due to cross relaxation is not expected.

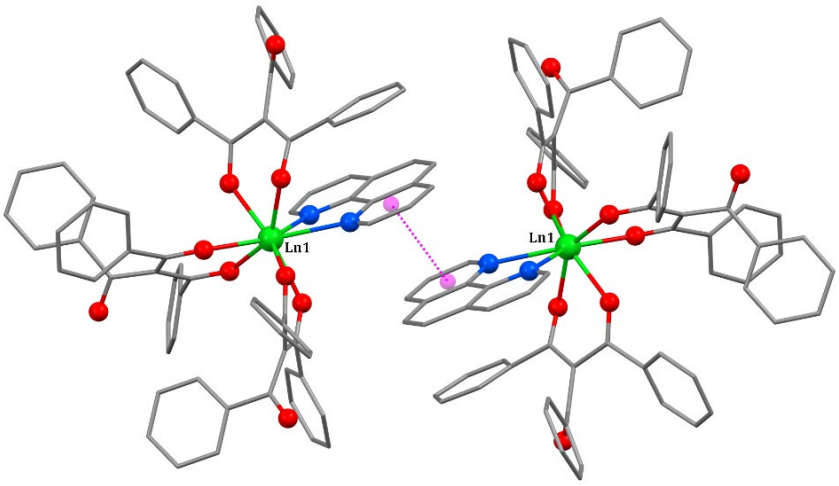

*Figure 3.3: Crystal structure of [Ln(**tbm**)$_3$(phen/d-phen)] (Ln = Sm^{3+}, Eu^{3+}, Yb^{3+}). Centroid-centroid distances are highlighted in magenta. Hydrogen and deuterium atoms omitted for clarity.*

3.4. Shape Analysis

All complexes presented in this chapter were compared to the 13 ideal octacoordinate geometrical shapes, with the resulting complexes ranging between SAPR, TDD, and BTPR. Their relative CShM values are shown in Table 3.4 alongside similar structures reported in literature.

Table 3.4: CShM values for the complexes presented in this chapter.

Complex	SAPR-8	TDD-8	BTPR-8
(HNEt$_3$)[Sm(**dbm**)$_4$]·(EtOH)	1.165	0.866	
[a](HNEt$_3$)[Sm(**dbm**)$_4$]	0.528	1.688	
[Sm(**dbm**)$_3$(phen)]·(EtOH)	0.315	2.598	2.306
[b][Sm(**dbm**)$_3$(phen)]	1.488	1.583	1.750
[Sm(**tbm**)$_3$(phen)]	1.433	1.751	
[c][Eu(**tbm**)$_3$(phen)]	1.320	1.700	
[Eu(**tbm**)$_3$(*d*-phen)]	1.345	1.703	
[c][Yb(**tbm**)$_3$(phen)]	0.996	1.590	
[Yb(**tbm**)$_3$(*d*-phen)]	1.014	1.598	
[Y(**tbm**)$_3$(phen)]	1.105	1.638	

[a] *Experimental data in accordance with literature.*[58]
[b] *Experimental data in accordance with literature.*[81]
[c] *Experimental data in accordance with literature.*[67]

3.4.1. Dibenzoylmethane Complexes

Comparing the CShM values of the solvated and un-solvated complexes reveals some intriguing differences. The anionic complex $(HNEt_3)[Sm(\mathbf{dbm})_4]\cdot(EtOH)$ adheres more closely to a TDD when solvated, but the removal of the EtOH molecule drives it closer to a SAPR in shape. These differences are a result of different crystal packing forces, potentially brought about by the presence of the EtOH molecule. Although closer to different shapes, both molecules maintain a similar level of distortion from the LEIP (Figure 3.4).

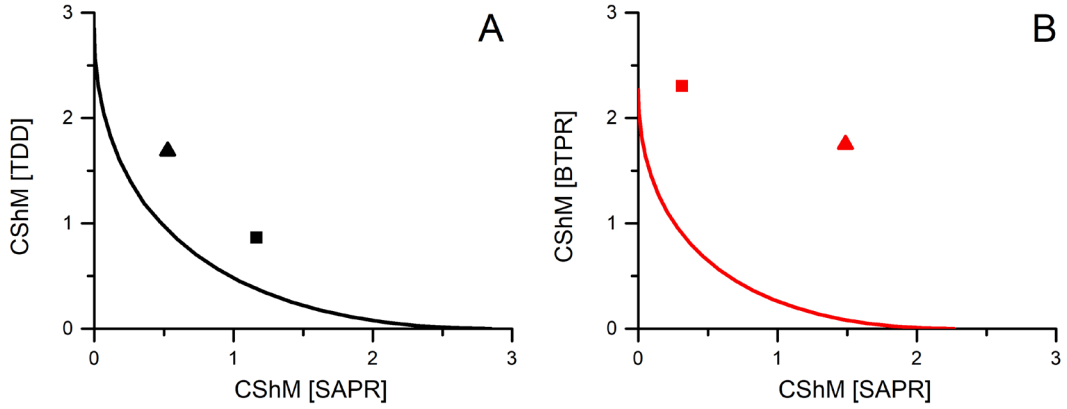

*Figure 3.4: (**A**) Shape map of $(HNEt_3)[Sm(\mathbf{dbm})_4]\cdot(EtOH)$ (black square) and *$(HNEt_3)[Sm(\mathbf{dbm})_4]$ (black triangle). (**B**) Shape map of $[Sm(\mathbf{dbm})_3(phen)]\cdot(EtOH)$ (red square) and *$[Sm(\mathbf{dbm})_3(phen)]$ (red triangle).*

**Experimental data in accordance with literature.[58, 81]*

A more distinct difference is present in the CShM values of the solvated and unsolvated $[Sm(\mathbf{dbm})_3(phen)]$ complex. Both complexes are closest in shape to a SAPR, however the solvated complex is far closer in shape to a SAPR than its next two closest shapes of TDD and BTPR. In comparison, the un-solvated complex was relatively evenly distorted between the three closest shapes of SAPR, TDD, and BTPR resulting in a highly distorted complex overall. The lack of distortion in the solvated complex may allow the coordinating ligands to pack closer together, which could explain the decreased bond lengths observed in Section 3.3.1.

3.4.2. Tribenzoylmethane Complexes

All phen and *d*-phen complexes maintained a consistent geometry that lay between a SAPR and a TDD, favouring the SAPR. The shape map of the **tbm** complexes is presented in Figure 3.5, showing the LEIP between the SAPR and TDD geometries. A consistent decrease in distortion was seen throughout the series, following the trend that smaller ionic radii result in less distorted coordination geometries.

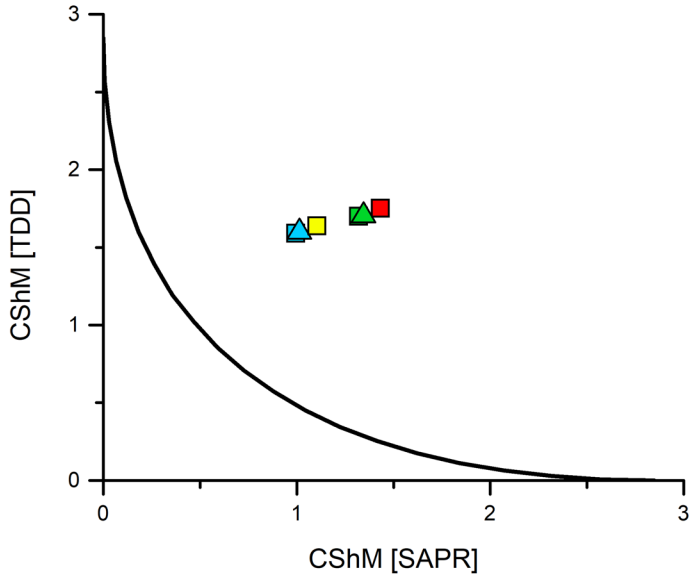

*Figure 3.5: Shape map of [Ln(**tbm**)$_3$(phen)] (square) and [Ln(**tbm**)$_3$(d-phen)] (triangle) for Ln = Sm^{3+} (red), Eu^{3+} (green), Yb^{3+} (blue), and Y^{3+} (yellow). Data for [Ln(**tbm**)$_3$(phen)] (Ln = Eu^{3+} and Yb^{3+}) was obtained from Abad Galàn, et al.*[4]

3.5. Photophysical Characterisation

As discussed in Section 2.5., the energy level of the triplet excited state for the coordinated ligand **tbm** lies high enough to provide effective sensitisation for Eu^{3+} and Yb^{3+}. This proves true for Sm^{3+} as well, where emission occurs from the $^4G_{5/2}$ excited state (~17,750 cm^{-1}).[82] **Dbm,** when coordinated, has a slightly lower triplet excited state energy (~20,580 cm^{-1})[67] than **tbm**, however it is still high enough to prevent BET from occurring. While phen has a higher triplet excited state (~21,050 cm^{-1})[83] than **dbm** and **tbm**, it lies close enough that it could affect

the sensitisation of the Ln^{3+} ion. If this proves true, then it is expected that differences will be seen in the photophysical properties of the deuterated and non-deuterated phen complexes.

$(HNEt_3)[Sm(\mathbf{dbm})_4]$ and $[Sm(\mathbf{dbm})_3(phen)]$ were measured in the solid-state. The phen and *d*-phen complexes were measured in the solid-state and a DCM solution at RT and 77 K. Quantum yields in solution for Sm^{3+} complexes were found to be below 0.1% and are not reported here. Solid-state quantum yields were unable to be measured for many of these complexes due to time constraints.

3.5.1. Dibenzoylmethane Complexes

Samarium

Sm^{3+} emission occurs from the $^4G_{5/2}$ excited state (~17,750 cm^{-1}) and is characterised by its orange-red colour.[82] Four peaks are typically observed in the visible region between 560 – 705 nm, which respectively correspond to the $^4G_{5/2} \rightarrow {}^6H_J$ transitions (J = 5/2 – 11/2) (Figure 3.6).[57, 82] The transition $^4G_{5/2} \rightarrow {}^6H_{5/2}$ is a MD transition, meaning its intensity does not vary much due to changes in symmetry. Conversely, the ED transition $^4G_{5/2} \rightarrow {}^6H_{9/2}$ is hypersensitive, causing its intensity to fluctuate with the coordination environment. As with Yb^{3+}, Sm^{3+} has an odd electron configuration ($4f^5$) allowing it to be classified as a Kramers ion. Unlike Yb^{3+} however, Sm^{3+} has multiple ground state J levels, each of which can undergo ligand field splitting resulting in a greater number of Stark states.

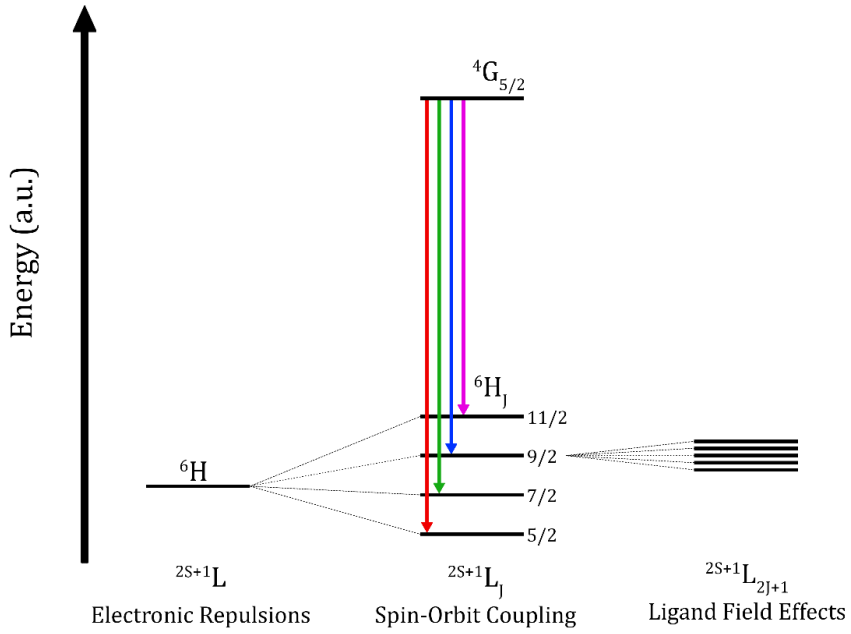

Figure 3.6: Energy level diagram of Sm^{3+}.

The typical Sm^{3+} emission bands resulting from the $^4G_{5/2} \rightarrow {}^6H_J$ transitions were observed in the emission spectra of the two **dbm** coordinated complexes, proving that sensitisation of the metal was effective. The excited state lifetime decay and overall photoluminescent quantum yield of these complexes as well as literature examples are presented in Table 3.5.

Table 3.5: Photophysical data of $(HNEt_3)[Sm(\mathbf{dbm})_4]\cdot(EtOH)$ and $[Sm(\mathbf{tbm})_3(phen)]\cdot(EtOH)$.

Complex	Medium	τ_{obs} (µs)	Φ_{Ln}^{L}(%)
$(HNEt_3)[Sm(\mathbf{dbm})_4]\cdot(EtOH)$	Solid-state	61	0.5
$[Sm(\mathbf{dbm})_3(phen)]\cdot(EtOH)$	Solid-state	55	–
*$[Sm(\mathbf{dbm})_3(phen)]$	Solid-state	41	5.7

**Experimental data in accordance with literature.*[81]

Previously, a $[Sm(\mathbf{dbm})_3(phen)]$ complex was reported to have a lifetime of 41 µs and a quantum yield of 5.7% in the solid-state.[81] Comparatively, the solvated complex reported here showed an elongated lifetime with a value of 55 µs (Figure 3.7). This increase in lifetime is quite interesting given the presence of EtOH should increase non emissive pathways, effectively quenching the excited state and consequently decreasing the luminescent lifetime. One potential cause for this is the difference in geometries observed in Section 3.3.1.,

however this is expected to affect the emission splitting pattern rather than the lifetime. Another alternative is the decreased distance between each monomer in the literature complex leading to cross relaxation, although given the smallest distance is 8.90 Å, cross relaxation pathways should be effectively prevented.[81]

The anionic complex possessed the longest luminescent lifetime (61 μs) out of these complexes but had a reduced quantum yield (0.5%) compared to the reported [Sm(**dbm**)$_3$(phen)]. While the reduced quantum yield is potentially due to the presence of EtOH, it is expected that EtOH would also reduce rather than increase the luminescent lifetime. However, given that the EtOH molecule is not directly coordinated to the Sm^{3+} centre it might not be affecting the luminescent properties in a significant manner. Assuming effects from EtOH are consistent between the two complexes allows the conclusion that a fourth **dbm** ligand improves the luminescent properties of the resulting complex more so than having phen coordinated.

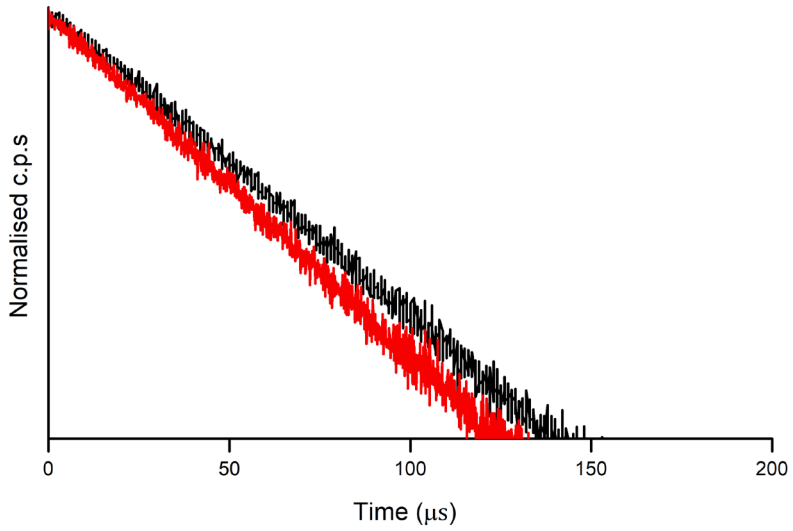

*Figure 3.7: Lifetime decay of (HNEt$_3$)[Sm(**dbm**)$_4$]·(EtOH) (black trace) and [Sm(**tbm**)$_3$(phen)]·(EtOH) (red trace). λ_{ex} = 350 nm.*

Shown in Figure 3.8 is the solid-state excitation and emission spectra of the two complexes, (HNEt$_3$)[Sm(**dbm**)$_4$]·(EtOH) and [Sm(**tbm**)$_3$(phen)]·(EtOH). A number of sharp peaks can be seen in the excitation spectra of both complexes which could arise from two sources. First is the Xe arc-lamp which is known to

produce sharp lines around 450 nm.[78] The second is the direct excitation of Sm^{3+}, in particular the sharp peaks at 398, 420, and 468 nm which could correspond to the $^6H_{5/2} \rightarrow {}^4K_{11/2}$, $^6H_{5/2} \rightarrow {}^6P_{5/2} + M_{19/2}$, and $^6H_{5/2} \rightarrow {}^4F_{5/2} + {}^4I_{13/2}$ transitions respectively.[84] The emission spectra of both complexes showed little J splitting from ligand field effects which potentially arises from their geometrical proximity to the LEIP as explored in Section 3.4.1. Only minimal peak shifts were observed, showing maxima of 564, 609, 650, and 713 nm for the anionic complex, and maxima of 565, 611, 647, and 708 nm for the phen coordinated complex.

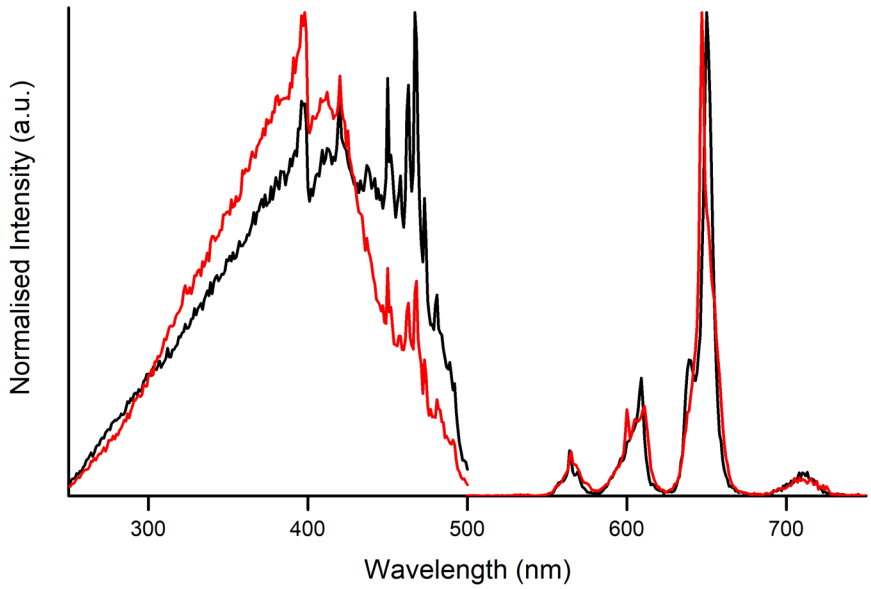

Figure 3.8: Excitation and emission spectra of $(HNEt_3)[Sm(\mathbf{dbm})_4]\cdot(EtOH)$ (black trace) and $[Sm(\mathbf{tbm})_3(phen)]\cdot(EtOH)$ (red trace) in the solid-state. λ_{ex} = 350 nm, λ_{em} = 650 nm.

3.5.2. Tribenzoylmethane Complexes

Both Sm^{3+} complexes displayed emission bands characteristic of Sm^{3+} resulting from the $^4G_{5/2} \rightarrow {}^6H_J$ transitions proving that sensitisation of the metal was effective (Figures 3.9 and 3.10). The excited state lifetime decay and overall photoluminescent quantum yield of these complexes are presented in Table 3.6.

*Table 3.6: Photophysical data of [Sm(**tbm**)$_3$(phen)] and [Sm(**tbm**)$_3$(d-phen)].*

Complex	Medium	τ_{obs} (µs)	Φ_{Ln}^{L} (%)
[Sm(**tbm**)$_3$(*d*-phen)]	Solid-state	129	--
	RT (DCM)	10	--
	77 K (DCM)	108 (30%) 203 (70%)	--
[Sm(**tbm**)$_3$(phen)]	Solid-state	80	4.0
	RT (DCM)	10	--
	77 K (DCM)	69 (34%) 135 (66%)	--

A shift in the excitation maximum of [Sm(**tbm**)$_3$(phen)] was observed in each measurement, likely owing to the rigidity and geometry of the complex in each medium. Secondary peaks can be seen in the DCM solution measurements, arising from secondary absorption bands present in the **tbm** ligands. In the emission spectra, different splitting patterns can be seen. The solid-state measurement showed the highest degree of splitting, with multiple peaks from different Stark states observable in each major peak. Comparitively, the 77 K and RT measurements show relatively smooth peaks with little sign of splitting. Emission from the ligand can be seen in the RT solution measurement, indicating that BET may be occurring between the ligand triplet excited state and the Sm^{3+} excited state. Cooling of the solution to 77 K removed the ligand emission, confirming that energy was being lost to BET.

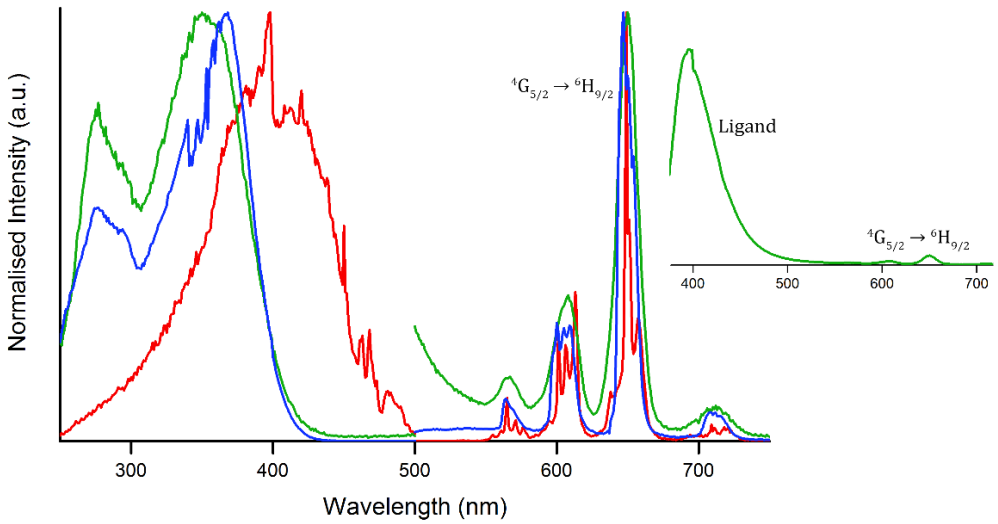

*Figure 3.9: Excitation and emission spectra of [Sm(**tbm**)$_3$(phen)] in the solid-state (red trace), a DCM solution at RT (green trace), and a DCM solution at 77 K (blue trace). λ_{ex} = 350 nm, λ_{em} = 650 nm.*

As with the Sm^{3+} complex, the *d*-phen complex saw a shift in excitation maximum from solid-state to solution, although the RT and 77 K measurements maintained almost identical excitation spectra. Splitting patterns of the solid-state measurements for both phen and *d*-phen complexes featured strong similarities in J-splitting and peak maximums, supporting the idea that both complexes are isostructural. The 77 K measurements also featured similar splitting patterns with the solid state measurements, indicating bothcomplexes adopted a similar degree of disorder to its crystalline structure upon freezing. The degree of splitting present demonstrates a high degree of distortion in the complex, backing up the observations made in Section 3.4.2. A heightened baseline was observable in the RT solution emission spectrum, suggesting BET may be occurring, although the severity of it is far less than observed in the phen complex.

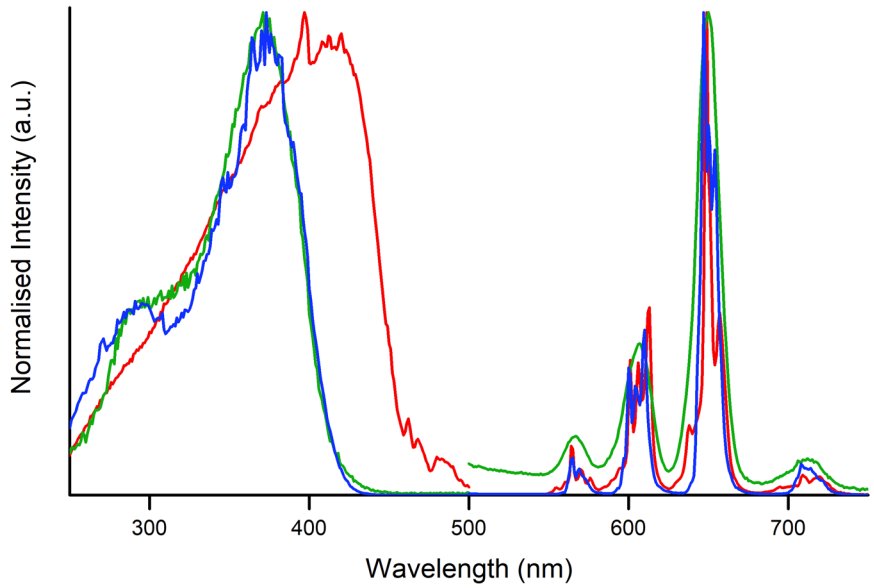

*Figure 3.10: Excitation and emission spectra of [Sm(**tbm**)$_3$(d-phen)] in the solid-state (red trace, λ_{ex} = 420 nm), a DCM solution at RT (green trace, λ_{ex} = 375 nm), and a DCM solution at 77 K (blue trace, λ_{ex} = 375 nm). λ_{em} = 650 nm.*

Both solid-state and RT solution measurements proved to be mono-exponential while the 77 K measurements were bi-exponential maintaining a similar ratio for each complex (~30:70) (Figure 3.11). Both RT solution lifetimes of the phen and *d*-phen were calculated as 10 µs and are significantly reduced in comparison to the solid-state and 77 K lifetimes. Presumably, the shortened lifetimes are due to BET quenching the desired radiative emission from the Sm^{3+} $^4G_{5/2}$ state. For the solid-state an increase of 49 µs was observed, from 80 µs (phen) to 129 µs (*d*-phen) whereas the 77 K measurement showed an increase of 39 µs for the lower percentage and 68 µs for the higher. The consistent increase in lifetime observed between the phen and *d*-phen complexes indicated that phen was affecting the luminescent properties, although quantum yield measurements would be required to state the full effect it may have on the sensitisation efficiency.

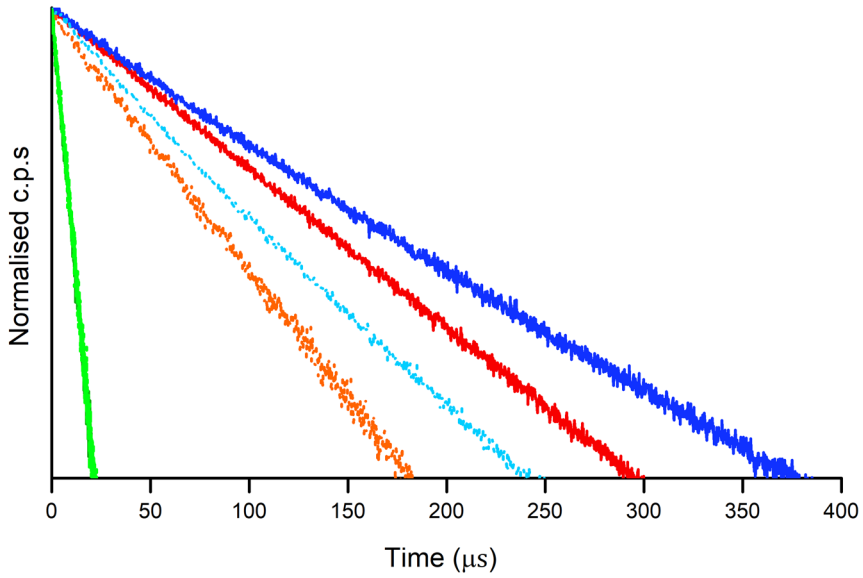

*Figure 3.11: Lifetime decay of [Sm(**tbm**)$_3$(d-phen)] (solid-state – solid red trace, DCM at RT – solid green trace, DCM at 77 K – solid blue trace) and [Sm(**tbm**)$_3$(phen)] (solid-state – dotted orange trace, DCM at RT – dotted lime trace, DCM at 77 K – dotted cyan trace). λ_{ex} = 420 nm (solid-state, d-phen), λ_{ex} = 375 nm (DCM at RT and 77 K, d-phen), λ_{ex} = 350 nm (phen).*

Europium

The innate splitting pattern of the $^5D_0 \rightarrow {}^7F_J$ (J = 0-4) transitions can be clearly seen in the emission spectra of [Eu(**tbm**)$_3$(*d*-phen)] (Figure 3.12). As with the Sm^{3+} *d*-phen complex, the RT and 77 K solution excitation spectra maintained the same maximum while the solid-state excitation spectrum was red shifted. The splitting pattern of the solid-state and 77 K emission spectra were relatively similar, confirming the higher degree of distortion observed in Section 3.4.2. Small signs of splitting could be seen in the RT solution, reminiscent of the patterns observed in the other spectra, however the peaks were more uniform overall due to the loss of rigidity in solution.

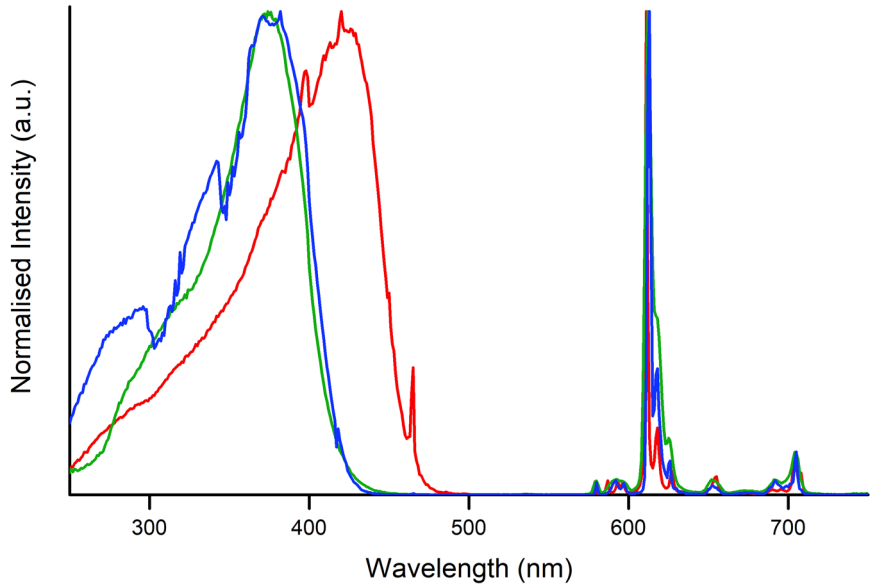

*Figure 3.12: Excitation and emission spectra of [Eu(**tbm**)$_3$(d-phen)] in the solid-state (red trace, λ_{ex} = 420 nm), a DCM solution at RT (green trace, λ_{ex} = 375 nm), and a DCM solution at 77 K (blue trace, λ_{ex} = 375 nm). λ_{em} = 615 nm.*

The excited state lifetime decay and quantum yield measurements of [Eu(**tbm**)$_3$(*d*-phen)] are given in Table 3.7 alongside values of the literature complex [Eu(**tbm**)$_3$(phen)].[67] Both the solid-state and RT solution lifetimes were mono-exponential, providing values of 542 µs and 132 µs respectively. The 77 K measurement was bi-exponential with a relatively even split between the two lifetimes of 452 µs (48%) and 704 µs (52%). Bar the 77 K measurement which

was reported as mono-exponential in the non-deuterated complex, the observed lifetimes were quite similar to the phen complex suggesting that phen does not have a significant impact in this system. This is further implied by the sensitisation efficiency of the RT solution being similarly poor in both complexes (phen = 0.6%, *d*-phen = 0.2%).

*Table 3.7: Photophysical data of [Eu(**tbm**)$_3$(phen)] and [Eu(**tbm**)$_3$(d-phen)].*

Complex	Medium	τ_{obs} (µs)	Φ_{Ln}^{L} (%)
[Eu(**tbm**)$_3$(*d*-phen)]	Solid-state	542	--
	RT (DCM)	132	0.2
	77 K (DCM)	452 (48%) 704 (52%)	--
*[Eu(**tbm**)$_3$(phen)]	Solid-state	550	45.0
	RT (DCM)	124	0.6
	77 K (DCM)	554	--

** Experimental data in accordance with literature.[67]*

Ytterbium

The Yb^{3+} *d*-phen complex presented the standard emission bands arising from its emissive $^2F_{5/2} \rightarrow {}^2F_{7/2}$ transition (Figure 3.13). As expected, its excitation spectra remained consistent with the previously presented *d*-phen complexes maintaining identical maxima for the solution spectra while the solid-state was red shifted. Small differences can be seen in the splitting patterns of the emission spectra. While three peaks are consistently seen, the maximum of the third peak is red shifted in the solid-state, extending the range of the emission band. Broadening of the emission band can be seen in the solid-state and RT solution spectra, evidence of thermally populated emissive states. Cooling to 77 K removes the thermal population of these states, resulting in sharper emission bands.

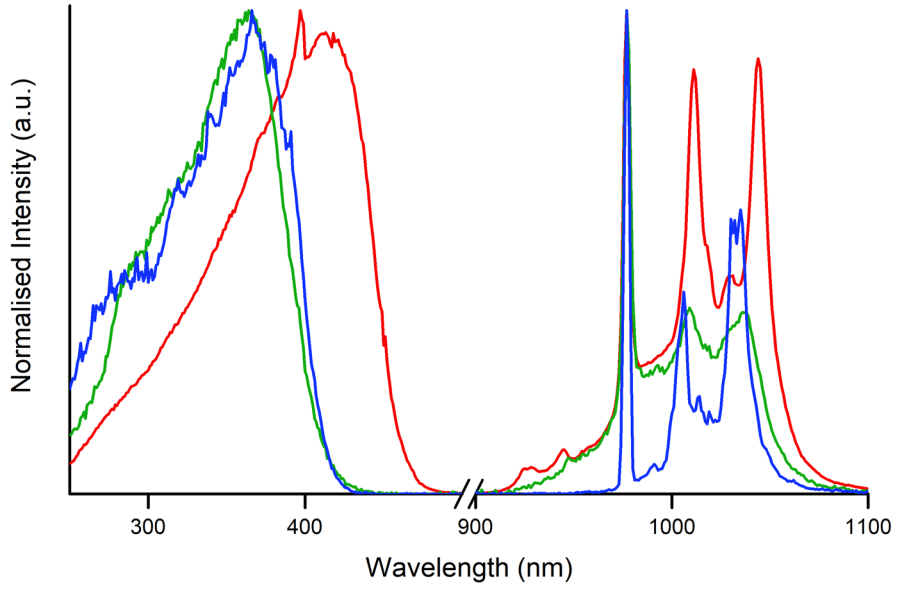

*Figure 3.13: Excitation and emission spectra of [Yb(**tbm**)$_3$(d-phen)] in the solid-state (red trace, λ_{ex} = 420 nm), a DCM solution at RT (green trace, λ_{ex} = 375 nm), and a DCM solution at 77 K (blue trace, λ_{ex} = 375 nm). λ_{em} = 977 nm.*

Shown in Table 3.8 is the luminescent lifetimes and quantum yields of the deuterated and non-deuterated Yb^{3+} complexes determined here and derived from the literature.[67] All lifetimes for the *d*-phen complex were mono-

exponential, following the pattern established by the non-deuterated complex (Figure 3.14).

*Table 3.8: Photophysical data of [Yb(**tbm**)$_3$(phen)] and [Yb(**tbm**)$_3$(d-phen)].*

Complex	Medium	τ_{obs} (µs)	Φ_{Ln}^{L}(%)
[Yb(**tbm**)$_3$(*d*-phen)]	Solid-state	40	--
	RT (DCM)	42	6.51
	77 K (DCM)	36	--
*[Yb(**tbm**)$_3$(phen)]	Solid-state	16	3.64
	RT (DCM)	18	1.16
	77 K (DCM)	16	--

** Experimental data in accordance with literature.[67]*

Unlike the previous deuterated complexes, a significant difference can be seen in the photophysical properties of the two Yb^{3+} complexes. The lifetimes of the *d*-phen complex are more than double those of the phen complex, ranging from 16 – 18 µs for phen compared to 36 – 42 µs for *d*-phen. Similarly, the quantum yield of the RT solution increased from 1.16% sensitisation efficiency to 6.51%. Interestingly the lifetime of the RT solution proved longest in both phen and *d*-phen complexes, contradicting the expected decrease due to increased molecular vibrations.

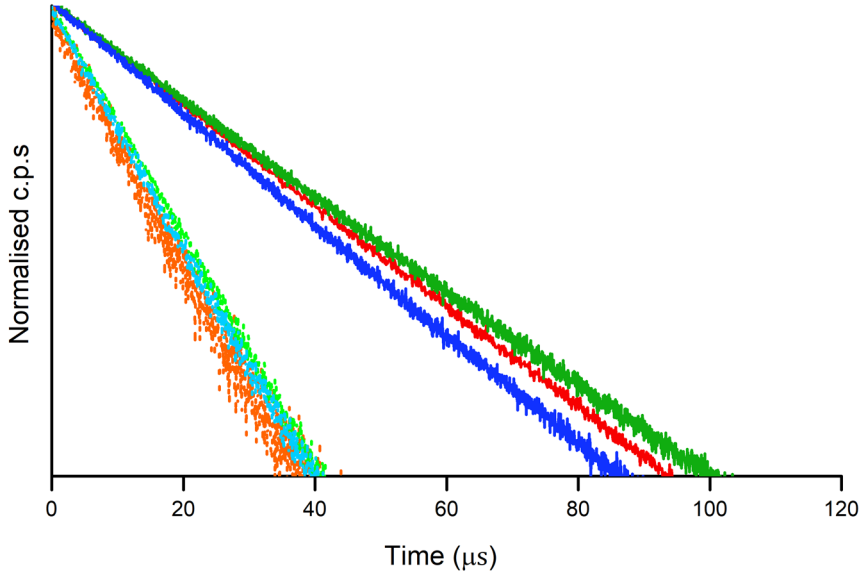

*Figure 3.14: Lifetime decay of [Yb(**tbm**)$_3$(d-phen)] (solid-state – solid red trace, DCM at RT – solid green trace, DCM at 77 K – solid blue trace) and *[Yb(**tbm**)$_3$(phen)] (solid-state – dotted orange trace, DCM at RT – dotted lime trace, DCM at 77 K – dotted cyan trace). λ_{ex} = 420 nm (solid-state, d-phen), λ_{ex} = 375 nm (DCM at RT and 77 K, d-phen), λ_{ex} = 350 nm (phen).*
**Experimental data obtained from Abad Galán, et al.[4]*

The increased values of the Yb^{3+} deuterated complex are quite interesting given the previous observations in the Sm^{3+} and Eu^{3+} complexes. The Eu^{3+} system showed little difference between the two complexes and while the Sm^{3+} complex saw some increase in the solid-state and 77 K measurements, neither of the changes seen in the Sm^{3+} complex compare to the scale of those observed in the Yb^{3+} complex. Based on these observations, it is hypothesised that phen is playing a part in the sensitisation of the Yb^{3+} and, to a lesser extent, Sm^{3+}.

A potential explanation for the observed changes in the Yb^{3+} complex lies within the theory of the antenna pathway. It was originally thought that because the energy of the triplet excited state of **tbm** was below that of phen (by ~350 cm^{-1}), then the excitation pathway will go *via* the **tbm** triplet excited state. This appears true for Ln^{3+} ions that possess small energy gaps with **tbm** and phen such as Eu^{3+} or Sm^{3+} (see Table 3.9 for energy gap values), where the ~350 cm^{-1} difference covers around 10% of the overall energy gap. However, the energy gap to the emissive Yb^{3+} ion is significantly greater, reaching ~10,504 cm^{-1} for **tbm** and ~10,850 cm^{-1} for phen (Table 3.9). At this level, the energy gap between the

triplet excited states of **tbm** and phen become negligible in comparison, suggesting sensitisation of the Yb^{3+} $^2F_{5/2}$ state could occur relatively efficiently from either ligand. Given sensitisation could be occurring from phen, replacement of the multiple C-H bonds on phen with the lower energy C-D bonds would in turn reduce multiphonon relaxation effects, enhancing the resulting photophysical properties.

Table 3.9: Energy gap between the Ln^{3+} emissive excited states and the ligand triplet excited states. All values are in wavenumbers (cm^{-1}).

	Sm^{3+} ($^4G_{5/2}$)	**Eu^{3+} ($^5D_1$)**	**Eu^{3+} ($^5D_0$)**	**Yb^{3+} ($^2F_{5/2}$)**
tbm	2,954	1,704	3,504	10,504
phen	3,300	2,050	3,850	10,850

Following the theory proposed, there should be no change in the Sm^{3+} complexes, however the results dictated otherwise. Given the presence of BET in the RT solution measurements it can be reasoned that the differences in the sensitisation pathways between Eu^{3+} and Sm^{3+} play a major factor in this process, although not enough information is present to make a conclusive statement.

3.5. Summary

This chapter sought to investigate whether 1,10-phenanthroline was impacting the photophysical properties of *β*-di- and *β*-tri- ketonate lanthanoid complexes, in particular those with the formula [Ln(**tbm**)$_3$(phen)]. The overall results indicate that phen does influence the properties of these complexes, although it appears to depend heavily on which Ln^{3+} is used.

Two **dbm** complexes were compared against one another; an anionic complex with the formula (HNEt$_3$)[Sm(**dbm**)$_4$]·(EtOH), and a neutral complex with the formula [Sm(**dbm**)$_3$(phen)]·(EtOH). The anionic complex showed elongated lifetimes compared to the phen coordinated complex, however it possessed remarkably poorer quantum yields than a literature complex with the formula [Sm(**dbm**)$_3$(phen)].[81] The decrease in quantum yield can be attributed to the EtOH solvent molecule which would increase multiphonon relaxation pathways, limiting the sensitisation efficiency. While these results showed promise, not enough information was recorded to allow for a thorough comparison between the two.

Next, *β*-triketonate complexes with the formula [Ln(**tbm**)$_3$(*d*-phen)] (Ln = Sm^{3+}, Eu^{3+}, Yb^{3+}) were investigated as a counterpart to a previously reported study conducted on complexes with the same formula, but with non-deuterated phen. It was found that the deuteration of the Yb^{3+} complex resulted in a significant increase in luminescent lifetimes and quantum yield. This was partially echoed by the Sm^{3+} complex which showed elongated lifetimes in the solid-state and 77 K measurements, however the Eu^{3+} complex did not exhibit any significant change in properties. From the information gathered, it can be reasoned that these observations are due to the energy gap between the triplet excited state of the ligands and the emissive excited states of the Ln^{3+}, where phen appears to have a greater impact on Ln^{3+} with lower emissive excited states. This would cause phen to have a much greater effect on NIR emitting lanthanoids such as Yb^{3+}, although further research is needed to see whether these observations hold true for Nd^{3+} and Er^{3+}.

Although it can be concluded that phen does affect the luminescent properties of *β*-triketonate complexes, not enough information is present to assess how this

effect manifests. Obtaining the solid-state quantum yields and extending the range of lanthanoids measured to Nd^{3+}, Er^{3+} would help to confirm the hypothesis presented here. Alternatively, time resolved spectroscopic studies could be carried out to further analyse the sensitisation pathway in order to distinguish why the Sm^{3+} complex showed changes while the Eu^{3+} system did not.

4.0. Di/Tri-naphthoyl Complexes

One complex presented in this chapter has been published, see Appendix 10.1. for the statement of contribution by others.

Abad Galán L., Wada S., Cameron L., Sobolev A. N., Hasegawa Y., Zysman-Colman E., Ogden M. I., Massi M.. *Dalton Trans.* **48**, 3768-3775 (2019) DOI: 10.1039/C8DT04749A

4.1. Introduction

This chapter continues research comparing *β*-diketonates and *β*-triketonates as antenna ligands for lanthanoid complexes. Following the publication of a series of **tnm** coordinated complexes with the formula [Ln(**tnm**)$_3$(DMSO)$_2$] (Ln = Nd^{3+}, Sm^{3+}, Eu^{3+}, Gd^{3+}, Yb^{3+}), work was attempted to isolate a matching series of complexes featuring **dnm**, rather than **tnm**. Presented here are three complexes with the formula [Ln(**dnm**)$_3$(DMSO)$_2$] (where Ln = Nd^{3+}, Eu^{3+}, Gd^{3+}), alongside a MeCN solvated complex, [Sm(**dnm**)$_3$(DMSO)$_2$]·(MeCN) and a **tnm** coordinated complex, [Sm(**tnm**)$_3$(DMSO)$_2$]. An analysis of the structural and photophysical complexes of these complexes will be presented along with comparisons between the **dnm** and **tnm** coordinated complexes.

*Crystals of [Sm(**dnm**)$_3$(DMSO)$_2$]·(MeCN)*

4.2. Synthesis

Isolation of **dnm**H was achieved by reacting sodium hydride and 2-acetonaphthanone with ethyl-2-naphthoate at 60 °C overnight in tetrahydrofuran (THF) (see Section 8.3. for experimental and spectroscopic information). Reacting the purified **dnm**H with sodium hydride and 2-naphthoyl chloride at 40 °C overnight in THF resulted in the formation of **tnm**H with further purification, after protonation, often proving unnecessary. This method was near-identical to the procedure followed for the synthesis of **tbm**H, although a change in solvent from ether to THF was required due to solubility issues with the naphthoyl groups in ether.

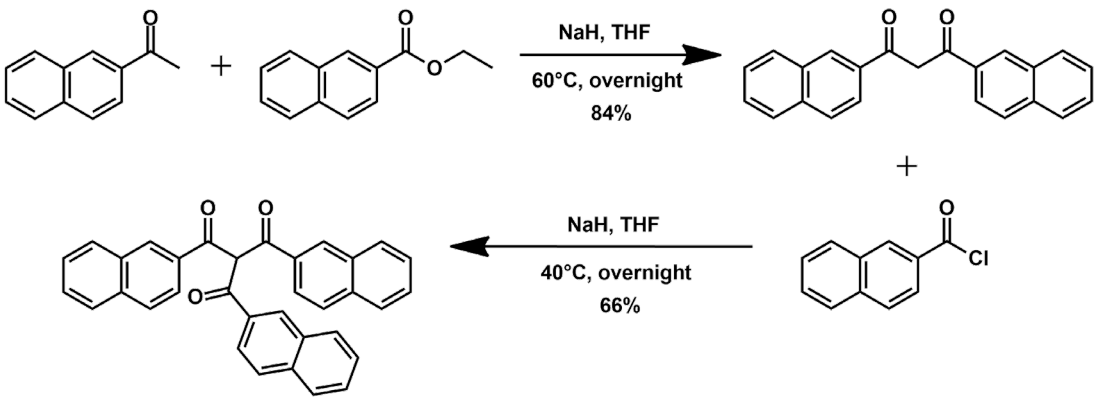

*Scheme 4.1: Synthetic pathway for the isolation of **dnm**H and **tnm**H.*

The **dnm** and **tnm** coordinated complexes were synthesised using the solvent layering method with DMSO and EtOH that was discussed in Section 2.2 (See Section 8.4.3 for experimental and spectroscopic information). One exception was observed in the case of [Sm(**dnm**)$_3$(DMSO)$_2$]·(MeCN) which was isolated using MeCN rather than EtOH for the second layer, leading to the solvated complex seen in Figure 4.2. This complexation method proved reliable in growing crystalline solids, often showing the formation of a single crystal after a few days.

4.3. X-Ray Diffraction Studies

All **dnm** complexes were octacoordinate; six coordination sites were occupied by the three bis-chelating **dnm** ligands while the remaining two were occupied by the monodentate DMSO ligands. Shown in Table 4.1 is the average Ln-O bond lengths as well as the Ln-Ln distance observed between monomers.

*Table 4.1: Selected inter- and intra- molecular distances (Å) of [Ln(**dnm**)$_3$(DMSO)$_2$] (Ln = Nd^{3+}, Eu^{3+}, Gd^{3+}) and [Sm(**dnm**)$_3$(DMSO)$_2$]·(MeCN). Refer to Figures 4.1 and 4.2 for the crystal structure. See Table A6 in Appendix 10.4.3. for individual bond lengths.*

Complex	Ln – O*	Ln – Ln
[Nd(**dnm**)$_3$(DMSO)$_2$]	2.42 (3)	7.605 (6)
[Eu(**dnm**)$_3$(DMSO)$_2$]	2.39 (3)	7.703 (5)
[Gd(**dnm**)$_3$(DMSO)$_2$]	2.38 (3)	7.845 (5)
[Sm(**dnm**)$_3$(DMSO)$_2$]·(MeCN) – 0.33 %	2.43 (4)	8.447 (5)
[Sm(**dnm**)$_3$(DMSO)$_2$]·(MeCN) – 0.66 %	2.43 (4)	
** Denotes averaged values.*		

The unsolvated **dnm** complexes proved to be isostructural, forming a crystal lattice from repeating monomer units shown in Figure 4.1. As expected from general Ln^{3+} complex trends, the average Ln-O bond length decreased as the size of the central atom decreased, starting from an average of 2.42 (3) Å for Nd^{3+} and reaching 2.38 (3) Å for Gd^{3+}. All Ln-Ln distances were below 8 Å suggesting that the emissive properties may be affected by cross relaxation between the Ln^{3+} ions.

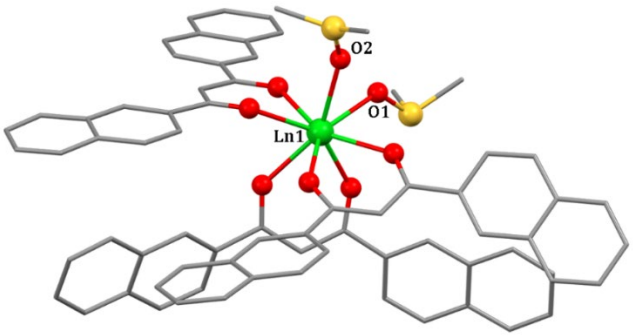

*Figure 4.1: Crystal structure of [Ln(**dnm**)$_3$(DMSO)$_2$] (Ln = Nd^{3+}, Eu^{3+}, Gd^{3+}). Hydrogen atoms omitted for clarity.*

Unlike the other **dnm** complexes, the Sm^{3+} complex was isolated with a MeCN molecule in the crystal lattice, leading to a different structural arrangement (Figure 4.2). Elongated Ln-O and Ln-Ln distances were observed due to this structural arrangement. As the Ln-Ln distance of 8.447 (5) Å was greater than the unsolvated complexes, non-radiative loss of energy due to cross relaxation should be prevented.

A disordered DMSO ligand can be seen at O2/O3 leading to altered geometrical shapes which will be explored further in Section 4.4. Disorder refers to the positional shift of a specific atom or molecule where it can occupy different conformations throughout the crystal lattice. Disordered molecules are often ignored as they do not tend to affect the shape or structural analysis of complexes. However, in this case the disordered DMSO ligand is directly coordinated to the metal centre, giving two different Sm-O distances (Sm-O2 = 2.455 (3) Å and Sm-O3 = 2.428 (4) Å) which can alter the shape of the first coordination sphere. The disordered molecule was observed in each position with a relative ratio of 1:2, leading to the 0.33% (O3) and 0.66% (O2) used to describe each orientation in tables and figures.

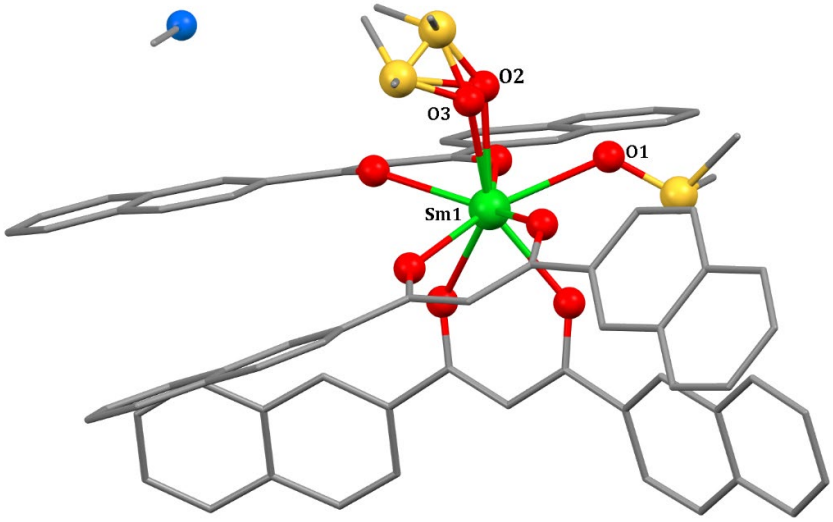

*Figure 4.2: Crystal structure of [Sm(**dnm**)$_3$(DMSO)$_2$]·(MeCN). Hydrogen atoms omitted for clarity.*

As with the varying **dnm** complexes, [Sm(**tnm**)$_3$(DMSO)$_2$] is octacoordinate, possessing six keto-O donor atoms from the **tnm** ligands and two O donor atoms by the DMSO ligands (Figure 4.3). The structure of this complex matched

previously reported complexes with the formula [Ln(**tnm**)$_3$(DMSO)$_2$] (Ln = Nd^{3+}, Eu^{3+}, Gd^{3+}, Yb^{3+}).[69] Shown in Table 4.3 is the selected inter- and intra- molecular distances observed in the crystal lattice.

*Table 4.3: Selected inter- and intra- molecular distances (Å) of [Sm(**tnm**)$_3$(DMSO)$_2$]. Refer to Figure 4.3 for the crystal structure.*

Measurement	Distance	Measurement	Distance
Sm1 – O1	2.373 (2)	Sm1 – O21	2.360 (2)
Sm1 – O2	2.370 (2)	Sm1 – O23	2.361 (2)
Sm1 – O11	2.436 (2)	Sm1 – O31	2.413 (2)
Sm1 – O13	2.373 (2)	Sm1 – O33	2.394 (2)
π – π	2.279	Sm1 – Sm1	10.706 (6)
Centroid – Centroid	4.989		

An inversion centre is present in the complex, forming a supramolecular dimer through π-π stacking of the naphthoyl groups (Figure 4.3), where the interplanar distance is 2.279 Å compared to the centroid-centroid distance of 4.989 Å. Ln-Ln distances of 10.706 (6) Å suggest the direct transfer of energy between the Sm^{3+} ions should be minimised. A general increase in Ln-Ln distances was observed between the **tnm** (10.706 (6) Å) and **dnm** (7.605 (6) – 8.447 (5) Å) complexes as expected for the bulkier ligand.

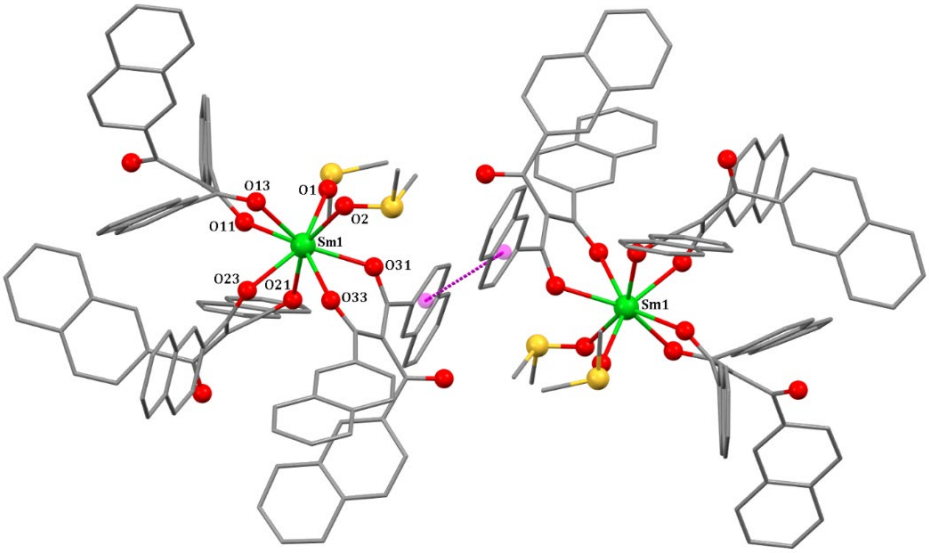

*Figure 4.3: Crystal structure of [Sm(**tnm**)$_3$(DMSO)$_2$]. Centroid-centroid distances are highlighted in magenta. Hydrogen atoms omitted for clarity.*

4.4. Shape Analysis

Using the equations proposed by Zabrodsky, *et al.*[76] and the software supplied by Casanova, *et al.*[26], the CShM values of the naphthoyl complexes were calculated and plotted against the LEIP as shown in Figure 4.4. The CShM values of the complexes is presented in Table 4.3.

*Table 4.3: CShM values of [Ln(**dnm**)$_3$(DMSO)$_2$] (Ln = Nd^{3+}, Eu^{3+}, Gd^{3+}), [Sm(**dnm**)$_3$(DMSO)$_2$]·(MeCN), and [Ln(**tnm**)$_3$(DMSO)$_2$] (Ln = Nd^{3+}, Sm^{3+}, Eu^{3+}, Gd^{3+}, Yb^{3+}).*

Complex	SAPR-8	TDD-8	BTPR-8
[Nd(**dnm**)$_3$(DMSO)$_2$]		0.470	2.210
[Eu(**dnm**)$_3$(DMSO)$_2$]		0.324	2.188
[Gd(**dnm**)$_3$(DMSO)$_2$]		0.321	2.180
[Sm(**dnm**)$_3$(DMSO)$_2$]·(MeCN) – 0.33 %		0.315	2.308
[Sm(**dnm**)$_3$(DMSO)$_2$]·(MeCN) – 0.66 %	2.333	0.404	
*[Nd(**tnm**)$_3$(DMSO)$_2$]	1.963	0.636	
[Sm(**tnm**)$_3$(DMSO)$_2$]	1.905	0.589	
*[Eu(**tnm**)$_3$(DMSO)$_2$]	1.923	0.563	
*[Gd(**tnm**)$_3$(DMSO)$_2$]	1.931	0.562	
*[Yb(**tnm**)$_3$(DMSO)$_2$]	1.872	0.497	

** Experimental data in accordance with literature.*[4]

The unsolvated **dnm** complexes were close to a TDD in shape, with their CShM values ranging from 0.470 to 0.321. BTPR was the next closest polyhedron, however the degree of distortion from this geometry was far greater due to the favoured TDD shape. A consistent decrease in CShM value was observed as the ionic radius of the metal decreased, matching the decrease in Ln-O bond lengths observed previously.

Similar to the unsolvated **dnm** complexes, both forms of the disordered **dnm** Sm^{3+} complex were closest in shape to a TDD. However, the 0.33% monomer was less distorted (CShM = 0.315) compared to the 0.66% monomer (CShM = 0.404). The next closest polyhedron for the distorted monomers also changed. The 0.33% monomer possessed a secondary promixity to a BTPR similar to the other

dnm complexes, whereas the 0.66% monomer was next closest to a SAPR, similar to the **tnm** complexes.

Overall, the **dnm** complexes, solvated or un-solvated possessed a low degree of distortion, suggesting the resulting photophysical spectra will not be heavily affected.

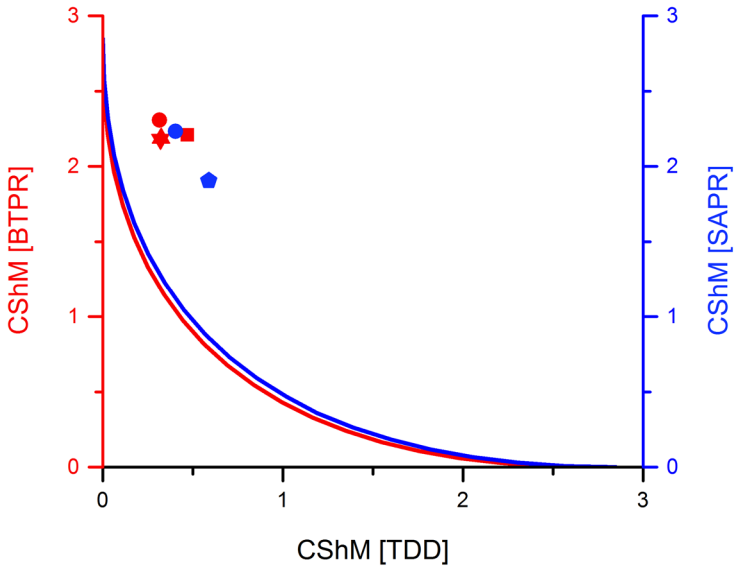

*Figure 4.4: Shape map of [Ln(**dnm**)$_3$(DMSO)$_2$], where Ln = Nd^{3+} (red square), Sm^{3+} (circle; 0.33% = red, 0.66% = blue), Eu^{3+} (red upright triangle), and Gd^{3+} (red upside-down triangle); and [Sm(**tnm**)$_3$(DMSO)$_2$] (blue pentagon).*

As with the **dnm** complexes and previously reported **tnm** complexes,[4] the Sm^{3+} **tnm** complex was closest in shape to a TDD. The CShM values of the **tnm** complexes were greater than the **dnm** complexes, showing an increase in distortion that likely arises from the third arm of the triketonate. However, the overall trend of decreasing distortion with decreasing ionic radii was clearly observed in the **tnm** complexes, with the CShm value of the Sm^{3+} complex lying between the CShM values of the Nd^{3+} and Eu^{3+} complexes.

4.5. Photophysical Characterisation

The energy levels of the triplet excited state for the two ligands **dnm** and **tnm** when coordinated have been previously reported at ~19,100 cm^{-1} and ~19,231 cm^{-1} respectively.[69, 85] This level suggests that sensitisation of Nd^{3+} ($^4F_{3/2}$ = ~11,111 cm^{-1}) will be efficient, whereas BET may be observed in the Sm^{3+} ($^4G_{5/2}$ = ~17,857 cm^{-1}) and Eu^{3+} ($^5D_0$ = ~17,241 cm^{-1}) complexes due to energy gaps smaller than ~3500 cm^{-1}. It is expected that sensitisation of Eu^{3+} will occur directly to the $^5D_0$ state, as the $^5D_1$ state lies either too close or higher than the triplet excited state of the ligands.

All complexes were measured in three different media; solid-state, acetonitrile solution at RT (10^{-5} M), and a frozen acetonitrile matrix at 77 K. Overall quantum yields in the solid-state for [Ln(**dnm**)$_3$(DMSO)$_2$] (Ln = Nd^{3+}, Eu^{3+}) were unable to be measured due to time constraints. Overall quantum yields in the solid-state and RT solution for the Sm^{3+} complexes were below 0.1% and are not reported here.

[Eu(dnm)$_3$(DMSO)$_2$]

The emission spectra of [Eu(**dnm**)$_3$(DMSO)$_2$] showcased the characteristic emission bands resulting from the $^5D_0 \rightarrow {}^7F_J$ (J = 0 – 4) transitions (Figure 4.5). Splitting of the ED transition ($^5D_0 \rightarrow {}^7F_2$, ~615 nm) is seen in the solid-state and 77 K measurements, suggesting the rigidity of the complexes in these media causes a greater degree of distortion than the RT solution. This is further supported by the different splitting patterns seen in the $^5D_0 \rightarrow {}^7F_1$ (~590 nm) transitions, where the solid-state emission can be seen split into two peaks, compared to the RT solution which adopts a single smoother peak.

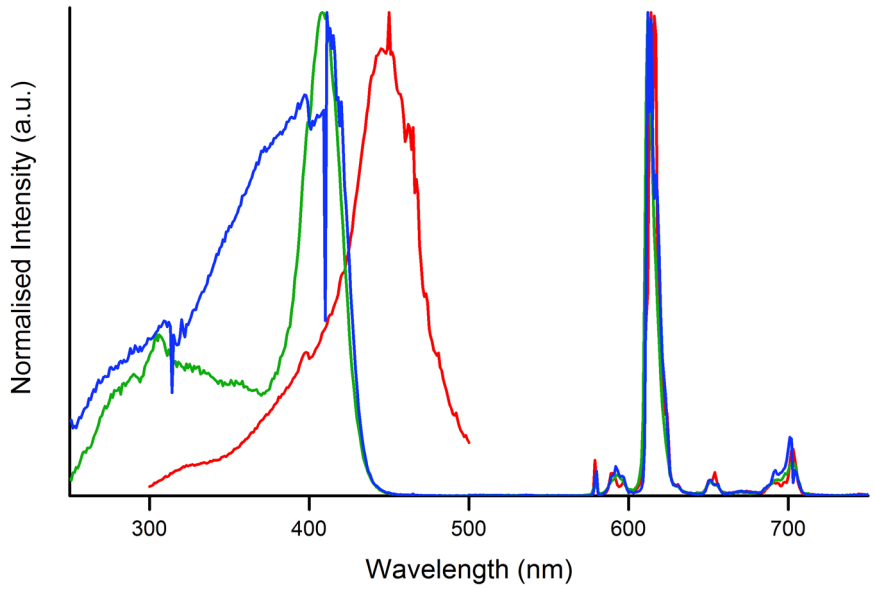

*Figure 4.5: Excitation and emission spectra of [Eu(**dnm**)$_3$(DMSO)$_2$] in the solid-state (red trace, λ_{ex} = 450 nm), a MeCN solution at RT (green trace, λ_{ex} = 410 nm), and a MeCN solution at 77 K (blue trace, λ_{ex} = 410 nm). λ_{em} = 615 nm.*

Shown in Table 4.4 is the excited state lifetime and overall quantum yields of [Eu(**dnm**)$_3$(DMSO)$_2$] and [Eu(**tnm**)$_3$(DMSO)$_2$] in each medium. For the **dnm** complex, both solid-state and RT solution lifetime measurements were mono-exponential, however the 77 K measurement was bi-exponential. The lifetime values followed the expected trend of the RT solution having the lowest lifetime at 33 µs, followed by the solid-state at 91 µs, and the 77 K measurement having the longest lifetimes of 400 µs (52%) and 696 µs (48%). Overall quantum yields for the RT solution proved to be quite poor, measuring an efficiency of 0.3%.

*Table 4.4: Photophysical data of [Eu(**dnm**)$_3$(DMSO)$_2$] and [Eu(**tnm**)$_3$(DMSO)$_2$].*

Complex	Medium	τ_{obs} (µs)	Φ_{Ln}^{L}(%)
[Eu(**dnm**)$_3$(DMSO)$_2$]	Solid-state	91	--
	RT (MeCN)	33	0.3
	77 K (MeCN)	400 (52%), 696 (48%)	--
*[Eu(**tnm**)$_3$(DMSO)$_2$]	Solid-state	117	9.0
	RT (MeCN)	20	0.2
	77 K (MeCN)	394	--

** Experimental data in accordance with literature.[69]*

A comparison of these values to the reported [Eu(**tnm**)$_3$(DMSO)$_2$][69] complex shows an increase in the lifetimes of the solutions at RT and 77 K, whereas a decrease is seen in the solid-state (Figure 4.6). Quantum yields of the **dnm** RT solution (0.3%) displayed a negligible increase from the **tnm** RT solution (0.2%), matching the observed increase in lifetime. However, the increase in quantum yields lies well within the error margins of the technique itself, preventing a conclusive statement of improved efficiency.

Although BETs are suspected to occur due to the energy gap between the triplet and emissive excited state, no clear evidence could be seen that suggests the presence of this effect. While it is likely that BET can occur in this complex, it does not appear to have a noticeable effect on its luminescent properties from current observations.

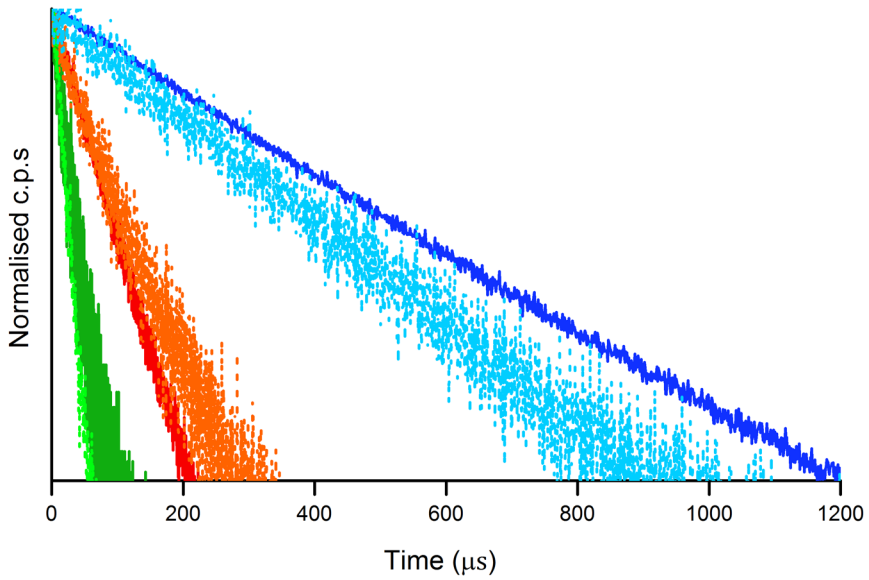

*Figure 4.6: Lifetime decay of [Eu(**dnm**)$_3$(DMSO)$_2$] (solid-state – solid red trace, MeCN at RT – solid green trace, MeCN at 77 K – solid blue trace) and *[Eu(**tnm**)$_3$(DMSO)$_2$] (solid-state – dotted orange trace, MeCN at RT – dotted lime trace, MeCN at 77 K – dotted turquoise trace). λ_{ex} = 440 nm (solid-state, **dnm**), λ_{ex} = 410 nm (MeCN at RT and 77 K, **dnm**), λ_{ex} = 350 nm (**tnm**).*

**Experimental data obtained from Abad Galán, et al.[69]*

[Nd(dnm)$_3$(DMSO)$_2$]

Nd^{3+} is one of the few lanthanoids to emit light solely in the NIR region. It possesses three emission bands around 900, 1060, and 1350 nm which result from the $^4F_{3/2} \rightarrow {}^4I_J$ (J = 9/2 – 13/2) transitions (Figure 4.7). As with Sm^{3+} and Yb^{3+}, Nd^{3+} is a Kramer's ion, possessing an odd electron configuration of $4f^3$, resulting in a halved number of Stark states.

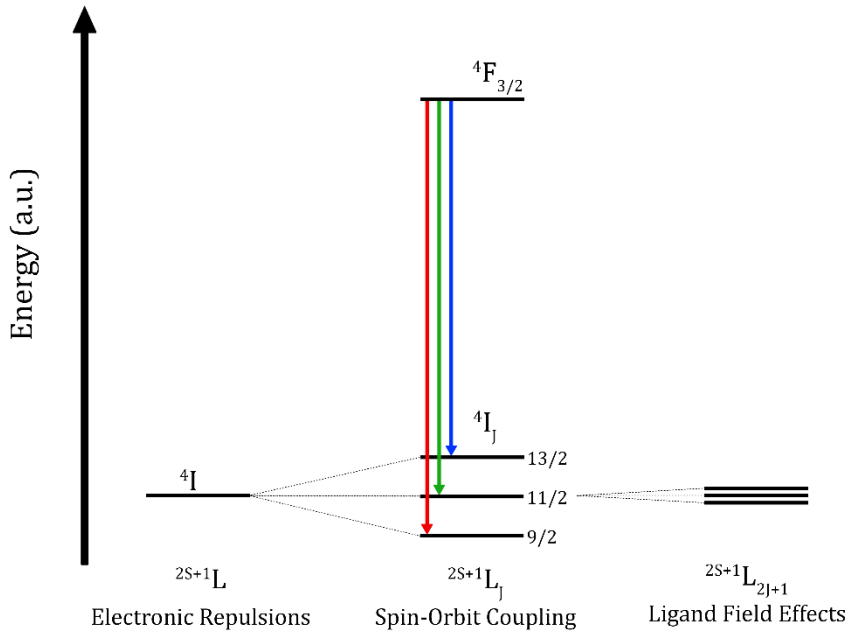

Figure 4.7: Energy level diagram of Nd^{3+}

The characteristic emission bands of Nd^{3+} resulting from the $^4F_{3/2} \rightarrow {}^4I_J$ (J = 9/2 – 13/2) transitions were present in the emission spectra of [Nd(**dnm**)$_3$(DMSO)$_2$] (Figure 4.8). All three transitions feature similar splitting patterns, proposing that the degree of distortion experienced in each medium were similar. Although the overall patterns follow the same trend, a shift in the peak maximum can be observed in the $^4F_{3/2} \rightarrow {}^4I_{11/2}$ transition ranging from 1056 nm (solid-state), to 1059 nm (MeCN, RT), to 1060 nm (MeCN, 77 K). While not a significant difference, this demonstrates that there is still an effect on the emissive properties due to structural changes.

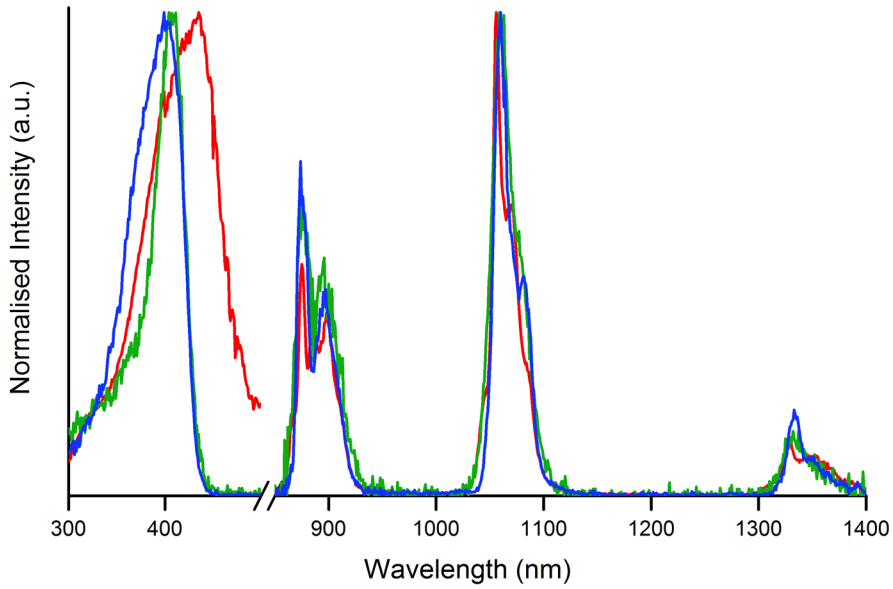

*Figure 4.8: Excitation and emission spectra of [Nd(**dnm**)$_3$(DMSO)$_2$] in the solid-state (red trace, λ_{ex} = 440 nm), a MeCN solution at RT (green trace, λ_{ex} = 410 nm), and a MeCN solution at 77 K (blue trace, λ_{ex} = 410 nm). λ_{em} = 1060 nm.*

The luminescent lifetime for this complex proved to be consistent across all three media, maintaining values around 10 µs for each (Table 4.5). Little difference was observed in the lifetimes between the **dnm** and **tnm** complexes, implying that the removal of a C-H oscillator did not have much effect on reducing non-radiative relaxation pathways.

*Table 4.5: Photophysical data of [Nd(**dnm**)$_3$(DMSO)$_2$] and [Nd(**tnm**)$_3$(DMSO)$_2$].*

Complex	Medium	τ_{obs} (µs)
[Nd(**dnm**)$_3$(DMSO)$_2$]	Solid-state	10
	RT (MeCN)	11
	77 K (MeCN)	10
*[Nd(**tnm**)$_3$(DMSO)$_2$]	Solid-state	10
	RT (MeCN)	10
	77 K (MeCN)	11

** Experimental data in accordance with literature.[69]*

Sm Naphthoyl Complexes

The two Sm^{3+} complexes presented the expected emission bands derived from the $^4G_{5/2} \rightarrow {}^6H_J$ (J = 5/2 – 11/2) transitions (Figures 4.9 and 4.10). An expected shift in the excitation bands was observed from solid-state to solution measurements for both complexes. The luminescent lifetimes of these complexes in each medium are presented in Table 4.6.

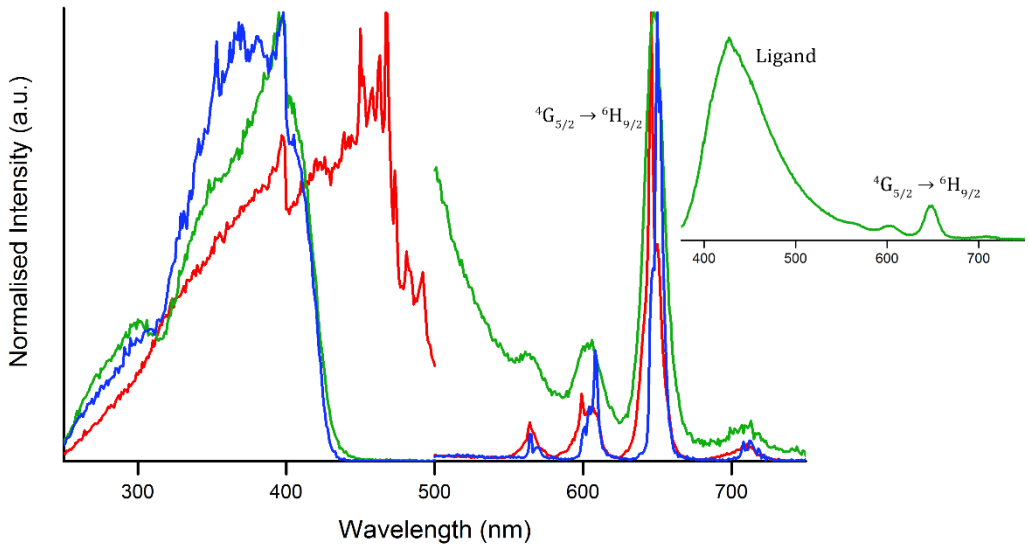

*Figure 4.9: Excitation and emission spectra of [Sm(**dnm**)$_3$(DMSO)$_2$]·(MeCN) in the solid-state (red trace), a MeCN solution at RT (green trace), and a MeCN solution at 77 K (blue trace). λ_{ex} = 350 nm, λ_{em} = 650 nm.*

As previously observed in the Sm^{3+} **dbm** complexes, several sharp bands can be seen in the excitation spectra of [Sm(**dnm**)$_3$(DMSO)$_2$]·(MeCN), likely arising from the Xe arc-lamp or direct excitation of Sm^{3+}. Emission from the **dnm** ligand can be seen in the RT solution measurement, presumably a result of BET occurring through thermal population. The lack of ligand emission in the 77 K emission spectra supports this idea, as cooling of the system would effectively suppress BET from occurring. Differences in the splitting patterns can be clearly seen between each medium, confirming the alteration of the coordination sphere upon dissolution.

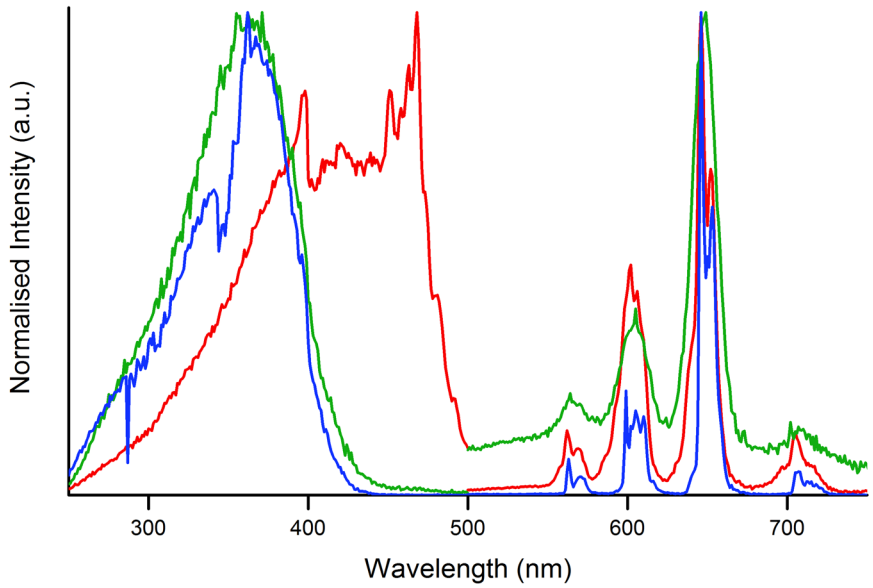

*Figure 4.10: Excitation and emission spectra of [Sm(**tnm**)$_3$(DMSO)$_2$] in the solid-state (red trace), a MeCN solution at RT (green trace), and a MeCN solution at 77 K (blue trace). λ_{ex} = 350 nm, λ_{em} = 650 nm.*

The excitation and emission spectra of the [Sm(**tnm**)$_3$(DMSO)$_2$] complex is very similar to the excitation and emission spectra of the **dnm** analogue. Emission from the **tnm** ligand can be seen in RT solution spectrum and sharp peaks are observed in the excitation spectrum, albeit fewer in number. The main differences between the spectra of the **dnm** and **tnm** complexes is seen in the splitting patterns from ligand field effects. In the **tnm** complex, all four peaks show increased splitting as they progress from the RT solution, to the solid-state, and to the frozen matrix. This is most clearly shown in the hypersensitive transition of $^4G_{5/2} \rightarrow {}^6H_{9/2}$ (~650 nm) which features a broadened single peak for the RT solution that splits into two for the solid-state and 77 K measurements. The increased splitting from **dnm** to **tnm** complexes was expected from the shape analysis, where the **tnm** complex was identified as having a greater degree of distortion than the β-diketonate analogue.

*Table 4.6: Photophysical data of [Sm(**dnm**)$_3$(DMSO)$_2$]·(MeCN) and [Sm(**tnm**)$_3$(DMSO)$_2$].*

Complex	Medium	τ_{obs} (μs)
[Sm(**dnm**)$_3$(DMSO)$_2$]·(MeCN)	Solid-state	9
	RT (MeCN)	9
	77 K (MeCN)	74 (66%), 46 (34%)
[Sm(**tnm**)$_3$(DMSO)$_2$]	Solid-state	8
	RT (MeCN)	9
	77 K (MeCN)	59 (16%), 142 (84%)

Excited state lifetimes of the two Sm complexes were mono-exponential for the solid-state and RT solutions, with values averaging around 9 μs (Figure 4.11, Table 4.6). The similarities between the solid-state and RT solution lifetimes suggest that even though ligand emission is not clearly seen in the solid-state spectra, non-radiative pathways are still favoured. Cooling to 77 K resulted in bi-exponential lifetimes, 74 μs (66%) and 46 μs (34%) for [Sm(**dnm**)$_3$(DMSO)$_2$]·(MeCN), compared to 59 μs (16%) and 142 μs (84%) for [Sm(**tnm**)$_3$(DMSO)$_2$]. Although an increase in luminescent lifetime is expected when measuring at 77 K, the extended lifetimes observed also attest to the inhibition of BET pathways seen in the other media. The increase in lifetime observed between the 77 K measurements of the **dnm** and **tnm** complexes indicates that the removal of the α-C-H oscillator is affecting the resulting emissions. However, the presence of BET in the solid state and RT solution measurements makes it difficult to observe whether this same effect is occuring in these media.

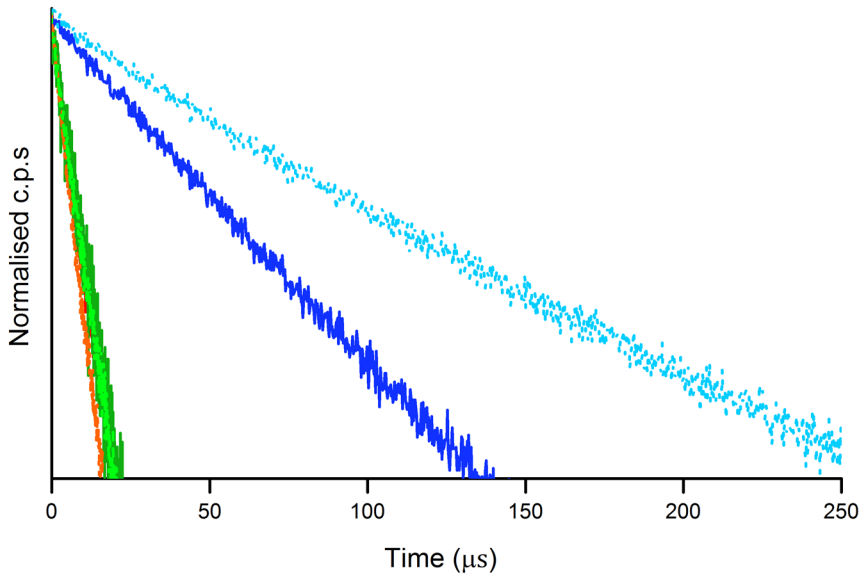

*Figure 4.11: Lifetime decay of [Sm(**dnm**)$_3$(DMSO)$_2$]·(MeCN) (solid-state – solid red trace, MeCN at RT – solid green trace, MeCN at 77 K – solid blue trace) and [Sm(**tnm**)$_3$(DMSO)$_2$] (solid-state – dotted orange trace, MeCN at RT – dotted lime trace, MeCN at 77 K – dotted cyan trace). λ_{ex} = 350 nm.*

4.6. Summary

Five new complexes were presented in this chapter, both starting and continuing a trend of isostructural Ln^{3+} complexes using naphthoyl derivatives of the *β*-di- and *β*-tri- ketonates. [Sm(**tnm**)$_3$(DMSO)$_2$] was proven to match a range of previously reported Ln^{3+} complexes with the same formula, for Ln = Nd^{3+}, Eu^{3+}, Gd^{3+}, and Yb^{3+}.[69] However, strong non-radiative relaxation pathways from BET were present due to a low energy gap between the triplet and emissive excited state of the ligand and Sm^{3+}.

The four [Ln(**dnm**)$_3$(DMSO)$_2$] (Ln = Nd^{3+}, Sm^{3+}, Eu^{3+}, Gd^{3+}) complexes proved to possess similar coordination geometry, with the exception of the Sm^{3+} complex, which was isolated as an acetonitrile solvate with a more distorted coordination sphere. The luminescent properties of these complexes were similar to their *β*-triketonate counterparts; however, a lack of quantum yield measurements make it difficult to conclude this with certainty.

Future work for this series includes the measurement of quantum yields for the solid-state as well as the isolation and full photophysical characterisation of [Yb(**dnm**)$_3$(DMSO)$_2$]. Analysis of these will allow for a comprehensive comparison to be made between the **dnm** and **tnm** complexes, in turn improving understanding of the effect caused by the α-C-H oscillator on these systems.

5.0. Bis-ketonates

5.1. Introduction

This chapter presents the synthesis of a new ligand, bis-tribenzoylmethane (Scheme 5.1, **Btbm**H_2) as well as the structural and photophysical investigation of two new bis-dibenzoylmethane (**Bdbm**H_2) complexes with the formula; [Ln_2(**Bdbm**)$_3$(phen)$_2$] (Ln = Eu^{3+}, Yb^{3+}). While the luminescent properties of **Bdbm**H_2 as a ligand in lanthanoid complexes had been previously investigated, no crystal structure had been reported, preventing further analysis on the coordination and geometry of these complexes.

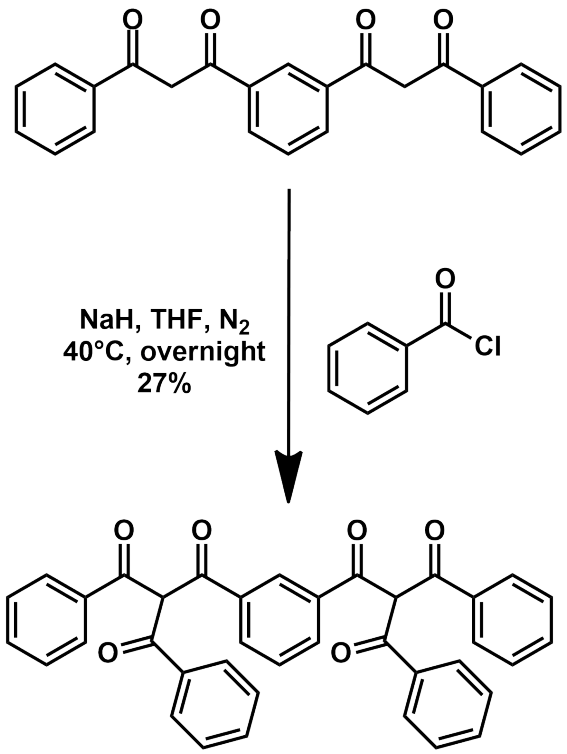

*Scheme 5.1: Synthetic pathway for the isolation of **Btbm**H_2 from **Bdbm**H_2*

5.2. Synthesis

The ligand **Bdbm**H_2 was synthesised using a modified version of the procedure reported by Bassett, *et al.*[86]. Dimethyl isophthalate and sodium hydride were combined in THF before adding acetophenone and heating at reflux overnight. Yields of this ligand were consistently lower than the value reported by Bassett, *et al.* suggesting the synthetic procedure requires further optimisation.

Synthesis of the ligand **Btbm**H_2 was eventually achieved using similar reagents and conditions to those used for the synthesis of **tnm**H. Dry THF was used with a minimal amount of sodium hydride and the solution was heated at a lower temperature. During the isolation of **Btbm**H_2, aqueous acids (hydrochloric and acetic acid, 1-5 M) were used to protonate the newly synthesised molecule, however a number of undesirable effects occurred upon the addition of the acid. These included the loss of solubility, the formation of unwanted side products, and what appeared to be decomposition of the **Btbm**H_2 ligand. Although no study was undertaken to confirm this final suggestion, decomposition of specific β-triketonates has been reported by Abad Galán[4] as a relatively consistent phenomena when deprotonated in protic solvents. To reduce the water content, which was the suspected cause of these issues, more concentrated acids were utilised, but the end result was typically the same. Switching to a non-aqueous acid (trifluoroacetic acid) for protonating the α-C gave positive results, allowing for the successful isolation of the ligand as confirmed *via* ^{1}H NMR, ^{13}C NMR, and high resolution mass spectrometry (see Section 8.3.).

Isolation of single crystals for **Bdbm** coordinated Ln^{3+} complexes was originally attempted using similar conditions to those of the DMSO solvated **tbm** complexes discussed in Section 2.2. The goal was to obtain complexes with the molecular formula $[Ln_2(\mathbf{Bdbm})_3(DMSO)_x]$ (where x = 1-4) to compare their luminescent properties against the DMSO solvated **tbm** complexes. However, the complexes proved to be poorly soluble, causing a powdery precipitate to form upon the layering of EtOH onto DMSO. Different systems were trialled to overcome this issue, such as switching EtOH for other solvents, freezing the DMSO before layering with EtOH to slow down interface interactions, and dissolving the complex components in a minimal amount of hot DMSO (150 °C)

and allowing to cool over several days. None of these methods proved successful, resulting in either a solid powder or no precipitate at all. Eventually a modified version of the evaporation method showed success, with the full method detailed in Section 8.4.3. By combining the ligands **Bdbm**H_2 and phen with a Ln^{3+} salt, and NEt_3 in THF and heating at reflux overnight the complex was allowed to form *via* surface reactions with the insoluble Ln^{3+} salt. Allowing the filtered solution to slowly evaporate consistently afforded needle-like crystals with X-Ray diffraction analysis proving the formation of complexes with the formula $[Ln_2(\mathbf{Bdbm})_3(phen)_2]$ (Ln = Eu^{3+}, Yb^{3+}).

5.3. X-Ray Diffraction Studies

Analysis of the crystallised **Bdbm** complexes revealed dinuclear structures featuring two eight coordinate Ln^{3+} ions where the **Bdbm** ligands acted as bridges, joining the two metal centres in a single complex. The dinuclear complex is symmetrical around a 2-fold rotation axis, with the Ln^{3+} coordination sphere comprising of two phen-N atoms and the remaining six sites belonging to the keto-O atoms of the **Bdbm** ligands. The crystal structure can be seen in Figure 5.1 while selected distances of the two **Bdbm** complexes are presented in Table 5.1.

*Table 5.1: Selected inter- and intra- molecular distances (Å) of [Ln_2(**Bdbm**)$_3$(phen)$_2$] (Ln = Eu^{3+}, Yb^{3+}). See Figure 5.1 for crystal structure.*

Measurement	[Eu_2(Bdbm)$_3$(phen)$_2$]	[Yb_2(Bdbm)$_3$(phen)$_2$]
Ln – N008	2.598 (6)	2.525 (5)
Ln – N009	2.590 (1)	2.547 (6)
Ln – O002	2.363 (5)	2.290 (4)
Ln – O003	2.347 (6)	2.279 (4)
Ln – O004	2.353 (5)	2.279 (4)
Ln – O005	2.332 (7)	2.259 (4)
Ln – O006	2.351 (6)	2.261 (4)
Ln – O007	2.335 (6)	2.261 (4)
Average Ln – N	2.594 (4)	2.54 (1)
Average Ln – O	2.35 (1)	2.2 (1)
Ln – Ln	7.986 (9)	7.983 (9)
Ln – Ln'	10.005 (7)	9.9278 (5)

' *Denotes intermolecular Ln atom.*

As expected from previous trends the average Ln-O and Ln-N bond lengths decreased in proportion with the ionic radii of the metal centres. The intramolecular Ln-Ln distance consistently remained around 7.98 (1) Å, presumably due to the distance being determined by the length of the **Bdbm** ligand. This length suggests that concentration quenching may occur in this complex, however there is no efficient method in which to prevent this without

altering the structure of the **Bdbm** ligand itself. The intermolecular Ln-Ln' distances were greater than 9 Å in both complexes.

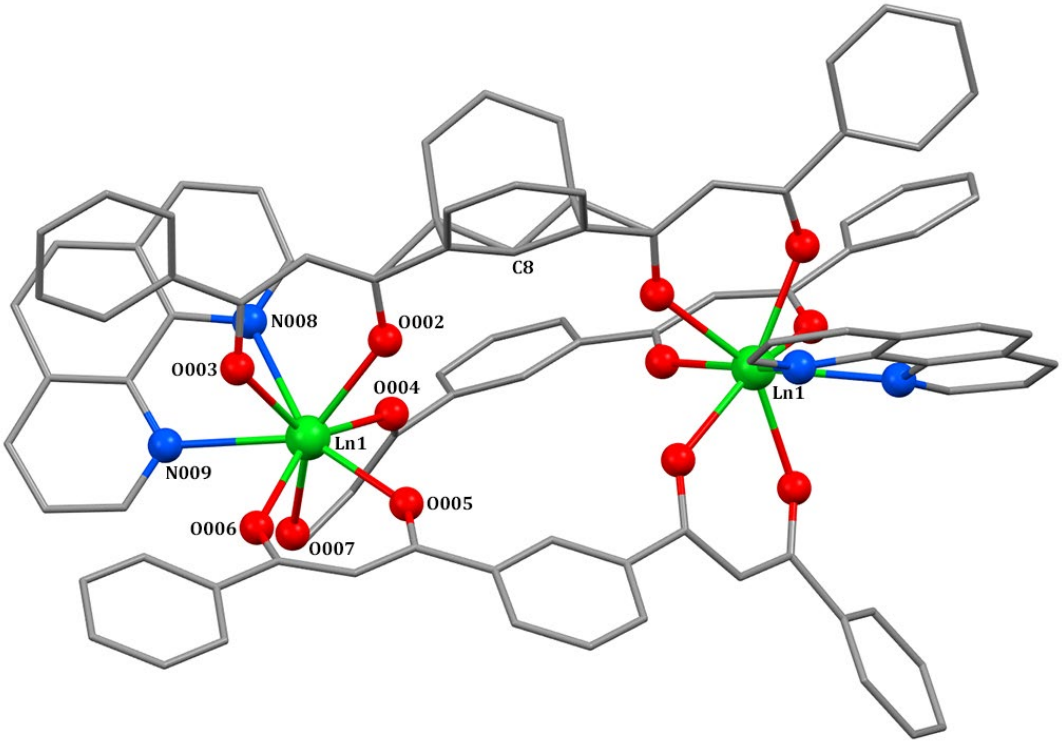

*Figure 5.1: Crystal structure of [Ln_2(**Bdbm**)$_3$(phen)$_2$] (Ln = Eu^{3+}, Yb^{3+}). Hydrogen atoms omitted for clarity.*

Two of the three **Bdbm** ligands displayed a helical twist in their coordination, rotating in the same orientation. Originating from the central phenyl ring, a curvature of almost 45° is achieved by one diketonate arm whilst a relatively planar structure is maintained by the other. Two phen molecules, lying on planes almost perpendicular to one another, are the likely cause of the helical twist as steric effects prevent a planar alignment of the **Bdbm** ligands. The third **Bdbm** ligand was situated between the two phen molecules and maintained a relatively planar conformation, however, the central aromatic ring is disordered about the 2-fold rotation axis, with C8 position on the axis.

5.4. Shape Analysis

Shape analysis of the coordination spheres showed that both complexes lay closest in shape to a SAPR, with their CShM values given in Table 5.2 and their position relative to the LEIP shown in Figure 5.2.

*Table 5.2: CShM values of [Ln_2(**Bdbm**)$_3$(phen)$_2$] (Ln = Eu^{3+}, Yb^{3+}).*

	SAPR	TDD	BTPR
[Eu_2(**Bdbm**)$_3$(phen)$_2$]	0.945	2.078	2.247
[Yb_2(**Bdbm**)$_3$(phen)$_2$]	0.608	2.152	1.977

While both complexes lay closest to a SAPR, their next closest shape varied; TDD was next closest for the Eu^{3+} complex, whereas BTPR was next closest for the Yb^{3+} complex. However, the overall CShM values for the TDD and BTPR geometries were quite close suggesting that a change in secondary geometries will be seen throughout the Ln^{3+} series. The drop in CShM value (SAPR) from the Eu^{3+} (0.945) to Yb^{3+} (0.608) complex remained consistent with decreases seen in the [Ln(**tbm**)$_3$(phen)] (Ln = Eu^{3+}, Yb^{3+}, Table 3.4) complexes continuing the trend of decreasing ionic radii resulting in less distorted complexes.

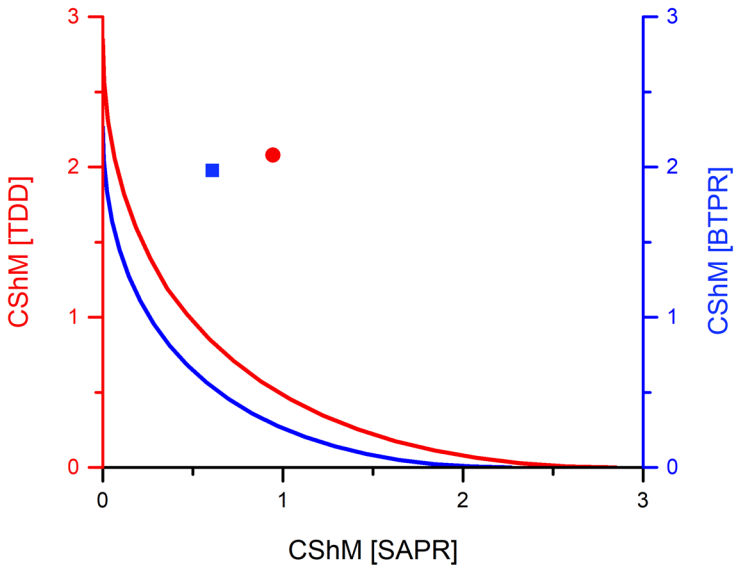

*Figure 5.2: Shape map of [Ln_2(**Bdbm**)$_3$(phen)$_2$] for Ln = Eu^{3+} (circle) and Yb^{3+} (square).*

5.5. Photophysical Characterisation

Measurement of the triplet excited state of **Bdbm** was previously reported by Basset, *et al.*[86] to lie at ~20,408 cm^{-1}. This places it slightly lower than **dbm** (~20,580 cm^{-1}) and **tbm** (~20,620 cm^{-1}) yet higher than **dnm** (~19,100 cm^{-1}) and **tnm** (~19,231 cm^{-1}) suggesting that the sensitisation of Eu^{3+} and Yb^{3+} should be effective.

Both complexes were measured in the solid-state and in a DCM solution (10^{-5} M) at RT and 77 K. Overall quantum yields in solution were measured by applying the optically dilute method reported by Crosby and Demas[87] using $[Ru(bpy)_3Cl_2]$ in H_2O (3 x 10^{-6} M) as a reference. Overall quantum yields for the solid-state were unable to be measured due to time constraints.

$[Eu_2(Bdbm)_3(phen)_2]$

The excitation and emission spectra of $[Eu_2(\mathbf{Bdbm})_3(phen)_2]$ affirmed sensitation of Eu^{3+} was occurring due to the presence of its distinct emission bands (Figure 5.3). Although a shift in excitation maxima from solid-state to solution is expected in Ln^{3+} complexes, this phenomenon was not observed here. A maximum of 400 nm was consistent for each excitation spectra, although the solid state excitation band was broader compared to the RT and 77 K bands. As with the excitation bands of **tbm** coordinated complexes in a RT solution, two distinct peaks were observed, although the separation seen in the **Bdbm** complex showed better resolution than in previous examples.

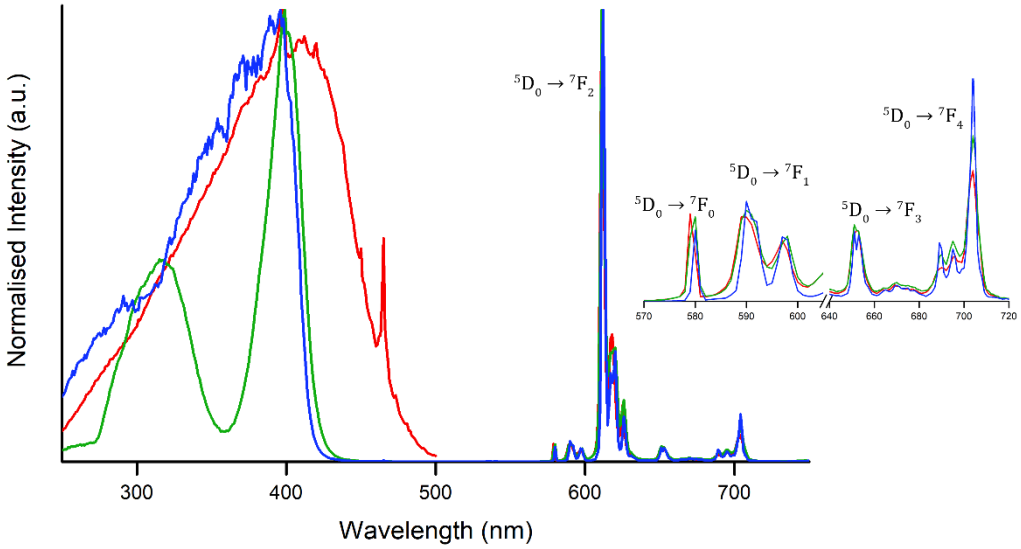

*Figure 5.3: Excitation and emission spectra of [Eu$_2$(**Bdbm**)$_3$(phen)$_2$] in the solid-state (red trace), a DCM solution at RT (green trace), and a DCM solution at 77 K (blue trace). λ_{ex} = 400 nm, λ_{em} = 615 nm.*

Little change is seen in the splitting pattern for each emission spectrum, implying the coordination geometry of the complex remains the same in the solid-state and in solution. This runs contrary to most β-di- and β-tri- ketonate complexes which tend to experience an increased degree of flexibility in solution resulting in different splitting patterns. It is likely that the cause of this observation is the di-nuclear chelating nature of a single **Bdbm** ligand. Due to the steric effects introduced from **Bdbm** coordination, the geometry of the complex has more rigidity in solution leading to the similar splitting patterns observed.

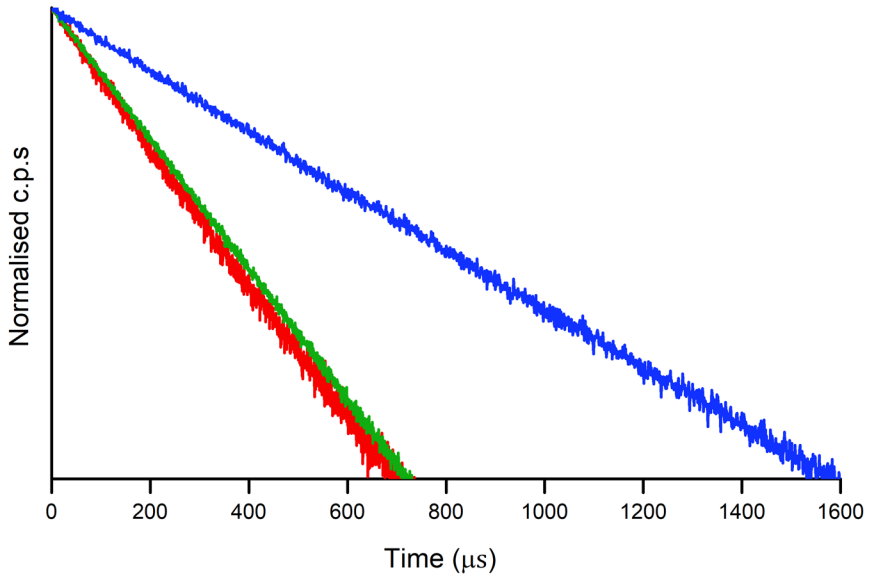

*Figure 5.4: Lifetime decay of [Eu$_2$(**Bdbm**)$_3$(phen)$_2$] in the solid-state (red trace), a DCM solution at RT (green trace), and a DCM solution at 77 K (blue trace). λ_{ex} = 400 nm.*

Shown in Figure 5.4 is the luminescent lifetime decay of [Eu$_2$(**Bdbm**)$_3$(phen)$_2$] in the solid-state, a RT DCM solution, and a DCM solution frozen at 77 K. The lifetime and quantum yield values are displayed in Table 5.3. The RT solution lifetime was mono-exponential while both solid-state and 77 K measurements were bi-exponential, with the longer lifetime having a relative percentage higher than 80%. Surprisingly, the lifetime of the complex in solution at RT (314 μs) was nearly equal to the solid-state (336 μs, 83%). A quantum yield of 7.5% was recorded for the RT solution showing a significant increase over similar phen and **dbm/tbm** complexes. The increased lifetime and quantum yield for the RT solution measurements further confirm the structural stability of this complex in solution, as the typically seen decrease in these values arise from the increased flexibility of complexes in solution, leading to more favourable non-radiative decay pathways. Although the solid-state measurements of the **Bdbm** complex featured shorter lifetimes than the previously reported [Eu(**dbm**)$_3$(phen)],[67] [Eu(**tbm**)$_3$(phen)],[67] and [Eu(**tbm**)$_3$(*d*-phen)] complexes (Table 3.6, Section 3.5.2.), an almost threefold increase was seen for the lifetime of the complex in solution (RT). This was heightened further for the quantum yield which showed a fivefold increase compared to the **dbm** complex.

*Table 5.3: Photophysical data of [Eu_2(**Bdbm**)$_3$(phen)$_2$] and [Eu_2(**Bdbm**)$_3$(X)$_?$].*

Complex	Medium	τ_{obs} (µs)	Φ_{Ln}^{L}(%)
[Eu_2(**Bdbm**)$_3$(phen)$_2$]	Solid-state	184 (17%), 336 (83%)	--
	RT (DCM)	314	7.5
	77 K (DCM)	447 (14%), 748 (86%)	--
*[Eu_2(**Bdbm**)$_3$(X)$_?$]	RT (DMF)	220	5.0
	77 K (DMF)	460	--
	RT (MeOH)	200	--
	77 K (MeOH)	350	--
	RT (MeOD)	300	--
	77 K (MeOD)	650	--

* *Experimental data in accordance with literature.*[86]

Although no crystal structures of a **Bdbm** coordinated lanthanoid complex have been previously reported, photophysical data of [Eu_2(**Bdbm**)$_3$] has been reported by Basset, *et al*.[86] with their reported lifetimes and quantum yield shown in Table 5.3. A quantum yield of 5.0% was reported for the DMF solution, a value lower than the phen complex reported here. The lifetime of the phen complex also proved longer than the measurements done on the reported, with the measurements in deuterated methanol (MeOD) showing the closest lifetime values. Though solvent ligands are not shown in the formula of the reported complex, the study concluded that there were up to three solvent molecules coordinated to each Eu^{3+} ion, with these being H_2O for the DMF measurements and MeOH/MeOD for the others. However, the decreased lifetime and quantum yield of the reported complex, compared to the phen complex, supports the idea that solvent molecules are present in the first coordination sphere, as they would enhance non-radiative pathways resulting in the reduced luminescent properties observed.

[Yb_2(Bdbm)$_3$(phen)$_2$]

Shown in Figure 5.5 is the excitation and emission spectra of [Yb_2(**Bdbm**)$_3$(phen)$_2$], where the unique emission of Yb^{3+} is clearly seen. Compared to the Eu^{3+} complex, a shift is seen in the excitation maxima from 400 nm (Eu^{3+}) to 390 nm (Yb^{3+}), with a more distinct shift seen in the solid-state maximum (414 nm). Two peaks can again be seen in the RT solution excitation spectrum, although the separation of these two peaks is not as distinct as the Eu^{3+} complex.

The emission spectra of each medium were consistent, showing three distinct peaks caused by the splitting of the J states from ligand field effects, although a fourth smaller peak can be seen in the 77 K emission spectrum. Hot bands were present in the solid-state and RT solution measurements caused by emission from thermally populated states. Cooling the complex to 77 K effectively removed the presence of these hot bands, providing sharper and more clearly defined emission peaks.

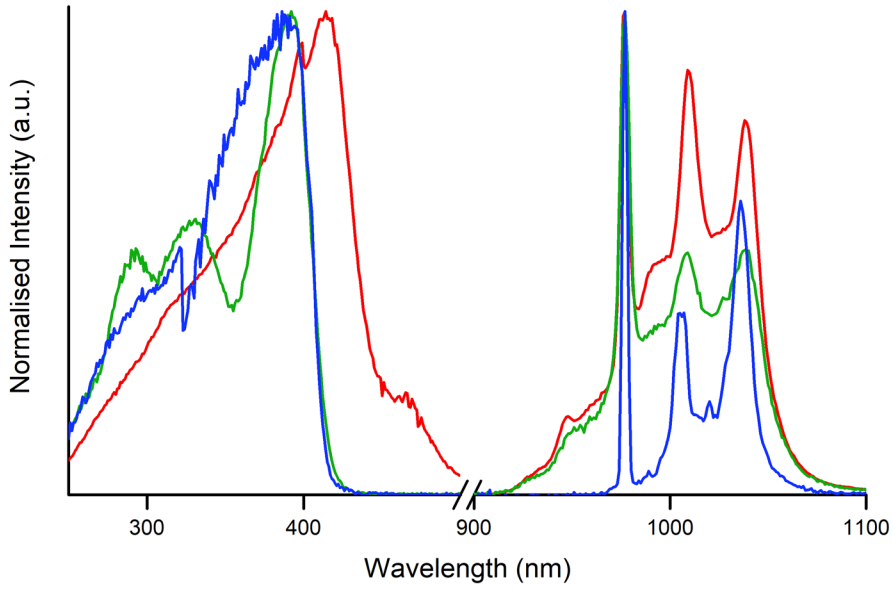

*Figure 5.5: Excitation and emission spectra of [Yb_2(**Bdbm**)$_3$(phen)$_2$] in the solid-state (red trace), a DCM solution at RT (green trace), and a DCM solution at 77 K (blue trace). λ_{ex} = 390 nm, λ_{em} = 977 nm.*

The luminescent lifetimes of the Yb^{3+} complex displayed a consistent increase from the solid-state (11 µs) to RT solution (12 µs) to 77 K (13 µs) with these values and the luminescent quantum yield presented in Table 5.4. Overall, these values were quite low, matching those of the previously reported [Yb(**dbm**)$_3$(phen)], and lower than the triketonate counterpart, [Yb(**tbm**)$_3$(phen)].[67] A decrease in quantum yield compared to the previously reported complexes was also observed, with a value of 0.5% being recorded for the **Bdbm** complex, compared to 0.87% for the **dbm** complex and 1.16% for the **tbm** complex.

*Table 5.4: Photophysical data of [Yb$_2$(**Bdbm**)$_3$(phen)$_2$].*

Complex	Medium	τ_{obs} (µs)	Φ_{Ln}^{L} (%)
[Yb$_2$(**Bdbm**)$_3$(phen)$_2$]	Solid-state	11	--
	RT (DCM)	12	0.60
	77 K (DCM)	13	--
*[Yb(**dbm**)$_3$(phen)]	Solid-state	11	2.91
	RT (DCM)	13	0.87
	77 K (DCM)	10	--
*[Yb(**tbm**)$_3$(phen)]	Solid-state	16	3.64
	RT (DCM)	18	1.16
	77 K (DCM)	16	--

** Experimental data in accordance with literature.[67]*

Given the observations made in Section 3.5.2., the shorter lifetimes observed in the **Bdbm** complex likely arise from the coordination of phen. Although the triplet excited state of the **Bdbm** ligand is lower than **tbm** and **dbm**, the overall difference is still insignificant compared to the energy gap overcome for the sensitisation of Yb^{3+}. To further investigate these complexes, in particular the increased properties observed in the Eu^{3+} RT solution measurements, the coordination of *d*-phen should be attempted. This would offer deeper insight into the effect of phen on these systems, whilst simultaneously furthering the investigation into the luminescent properties of **Bdbm** complexes.

5.6. Summary

A new ligand and two new complexes were presented in this chapter, paving the way for a new aspect of exploration in the field of lanthanoid *β*-triketonate complexes.

Isolation of the new molecule **Btbm**H_2 was eventually achieved using a modified version of previously reported *β*-triketonate synthetic procedures, but the compound is suspected to be unstable in protic solvents. Although time constraints hindered an investigation into the stability of this ligand in different solvents it is a recommend pathway for future research. A stronger focus on future work for this ligand lies in the crystallisation of new Ln^{3+} complexes, allowing for studies on their structural and photophysical properties. This will allow for comparisons between the *β*-di- and *β*-tri- ketonates to further one of the overarching goals of this research.

The two new complexes [Eu_2(**Bdbm**)$_3$(phen)$_2$] and [Yb_2(**Bdbm**)$_3$(phen)$_2$] maintained consistent structural properties, showing expected decreases in bond lengths and distortion with smaller ionic radii. Attempts to crystallise these complexes with solvent molecules as co-ligands proved fruitless. However, the addition of phen as a co-ligand resulted in readily formed crystalline products. The successful isolation of a solvent coordinated complex remains a target however, as the formation of such a complex would offer insight into the behavior of these complexes.

Unlike previous the *β*-di- and *β*-tri- ketonate ligands presented here which formed mononuclear complexes, the bis-ketonate structure of **Bdbm**H_2 allowed the formation of dinuclear complexes that exhibited a helical twist in their crystalline structure. These complexes appeared to possess greater stability in solution, however solution studies *via* NMR spectroscopy would be necessary to state this with any certainty. Increased structural stability in solution was also suggested by the improved photophysical properties observed in the Eu^{3+} RT solution measurements. Excited state lifetimes were similar in value to the solid-state measurements and a significant increase in luminescent quantum yields were observed compared to previously reported Eu^{3+} complexes. However, the benefits observed in the visible emitting Eu^{3+} complex were not observed in the

NIR emitting Yb^{3+} complex, which possessed photophysical properties similar to that of [Yb(**dbm**)$_3$(phen)]. As the structure and stability of the complex appears to have less of an effect on NIR emitting lanthanoids, it suggests that these Ln^{3+} systems are more heavily affected by alternative factors, such as quenching or poor sensitisation. Given the intramolecular Ln-Ln distances were shown to be less than 8 Å, there is a chance that cross relaxation can occur. Alternatively, the unremarkable luminescent properties could arise from the coordination of phen, as explored in Chapter 3. Overall, it will be interesting to investigate the luminescent properties of **Btbm** coordinated complexes as the increase in luminescent properties from [Yb(**tbm**)$_3$(phen)] to [Yb(**dbm**)$_3$(phen)] appeared to derive from the removal of a C-H oscillator and there remains the possibility that a similar situation could be observed here.

6.0. NMR Studies

6.1. Introduction

Analysis of lanthanoid complexes *via* ^{1}H NMR spectroscopy is complicated by two main issues. First is the paramagnetic nature of most Ln^{3+}, causing faster relaxation times which results in poorer resolution and broadening of observable peaks.[88] Second is their unique ligand field and coordination effects. Depending on the environment it is possible for ligands to exchange in solution which can also cause peak broadening. Another potential effect of coordination on the ligands is significant peak shifts. This effect is more pronounced in certain lanthanoids, but all exhibit these effects to some degree.[88-89]

Despite these issues, there are exceptions that make ^{1}H NMR studies possible. For example, La^{3+} and Lu^{3+} are diamagnetic, and Sm^{3+}, despite its paramagnetic nature, induces less peak broadening and shifts than the other paramagnetic Ln^{3+} allowing relatively clean ^{1}H NMR spectra to be recorded. Lastly, Y^{3+} can be used. As a diamagnetic ion, Y^{3+} possesses similar coordination chemistry to the lanthanoids, and has an ionic radius akin to Ho^{3+} making it an ideal point of comparison between the two extremes of the lanthanoids, La^{3+} (largest) and Lu^{3+} (smallest).[75]

This chapter presents a preliminary investigation into the coordination of *β*-di- and *β*-tri- ketonates in solution. Through identification and understanding of the chemical shifts and peak broadening exhibited by the different Ln^{3+} complexes, it is hoped that a reliable method will be found for confirming whether or not the coordination of a desired complex is maintained in solution.

The ^{1}H NMR spectra presented here are split into two sections based upon their relative co-ligands; DMSO or phen. All uncoordinated ligand spectra shown in this chapter were deprotonated with excess NEt_3 prior to analysis to more accurately represent their chemical nature when coordinated. Deuterated acetonitrile was used as the solvent for all solutions.

6.2. DMSO Co-Ligands

[La(tbm)$_3$(DMSO)$_2$]

Shown in Figure 6.1 is the ^{1}H NMR spectrum of [La(**tbm**)$_3$(DMSO)$_2$] (black trace) overlaid with the spectrum of **tbm** (red trace). Trace amounts of **tbm** can be seen in the complex spectrum, hinting that some form of ligand disassociation is occurring within solution. The large apparent (appt) triplets (7.25 – 7.05 ppm, black trace) show signs of broadening suggesting they belong to the coordinated **tbm** ligands; however, a detailed analysis is not feasible due to the same broadening effect.

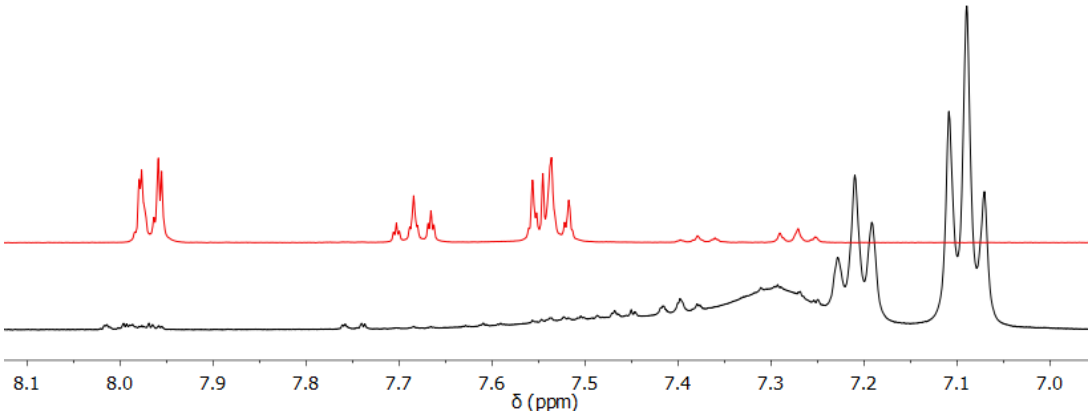

*Figure 6.1: ^{1}H NMR spectra of the complex [La(**tbm**)$_3$(DMSO)$_2$] (black trace) and **tbm** (red trace).*

[Lu(tbm)$_3$(DMSO)(EtOH)]

Shown in Figure 6.2 is the ^{1}H NMR spectrum of [Lu(**tbm**)$_3$(DMSO)(EtOH)] (black trace) overlaid with the spectrum of **tbm** (red trace). Due to peak broadening, assignment of the complex spectrum peaks was unachievable. While no free ligand can be seen in the complex spectrum suggesting the ligands have remained coordinated, the broadened peaks at 7.30, 7.25, and 7.10 ppm (black trace) could be a result of a slow ligand exchange within the solution, alongside coordination effects. It is possible these peaks are related to the three main multiplets in the **tbm** spectrum (7.97, 7.69, 7.54 ppm, red trace), however the broadening of these peaks makes detailed interpretation difficult.

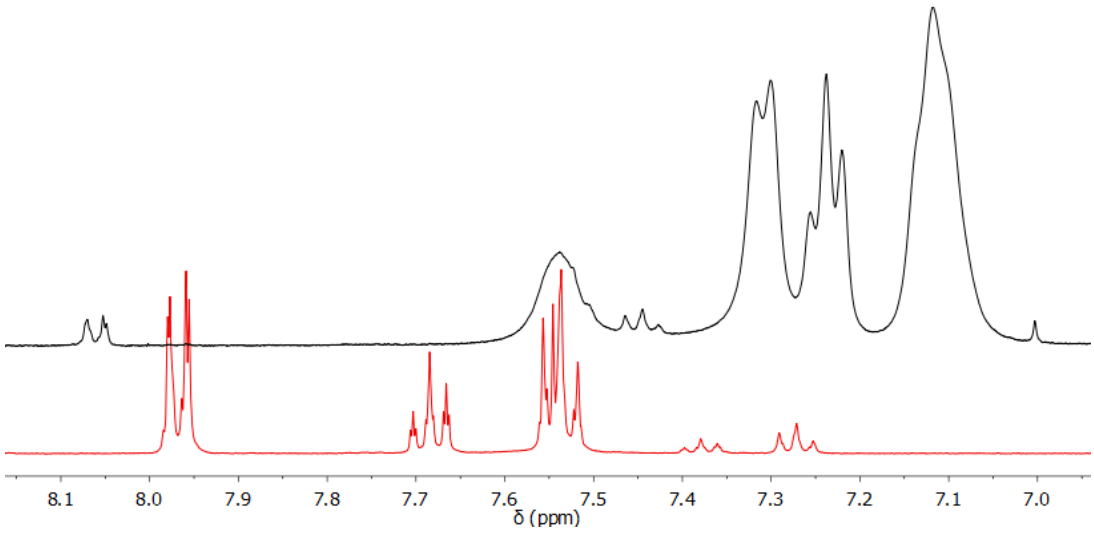

*Figure 6.2: ^{1}H NMR spectra of the complex [Lu(**tbm**)$_3$(DMSO)(EtOH)] (black trace) and **tbm** (red trace).*

[Sm(dnm)$_3$(DMSO)$_2$]

Shown in Figure 6.3 is the ^{1}H NMR spectrum of the complex [Sm(**dnm**)$_3$(DMSO)$_2$] (black trace) overlaid with the spectrum of **dnm** (red trace). The peaks present can be split into two groups; those that overlap with the deprotonated **dnm** and those that do not. The non-overlapping peaks present in the complex spectrum likely belong to the coordinated **dnm** ligand; however, their relative integration values did not match the expected ratios making them difficult to identify.

Conversely, the overlapping peaks shared the same chemical shift and integration values, indicating the presence of uncoordinated **dnm** molecules. It is unlikely that the peaks in the complex come from additional **dnm** molecules, instead implying a ligand exchange is occurring in solution. The loss of resolution in the complex spectrum further supports this, although no definitive conclusions can be made from the available data.

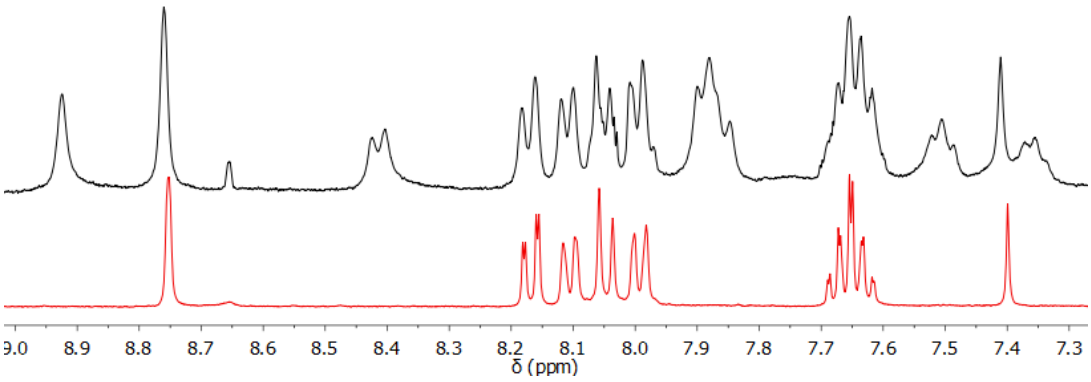

*Figure 6.3 ^{1}H NMR spectra of the complex [Sm(**dnm**)$_3$(DMSO)$_2$] (black trace) and **dnm** (red trace).*

[Sm(tnm)$_3$(DMSO)$_2$]

Shown in Figure 6.4 is the ^{1}H NMR spectrum of the complex [Sm(**tnm**)$_3$(DMSO)$_2$] (black trace) overlaid with the spectrum of **tnm** (red trace). Assignment of relevant peaks was made difficult due to the peak broadening exhibited by the complex. As such, no major similarities could be identified, although minor similarities can be seen in the form of the small peaks present in both ^{1}H NMR spectra around ~8.70 and ~8.10-7.95 ppm. The existence of these peaks implies the presence of free **tnm** molecules in the complex spectrum. However, determining whether this indicates an exchange of ligands as suggested by the [Sm(**dnm**)$_3$(DMSO)$_2$] spectrum would require an investigation beyond the scope of this work.

The broad peaks seen throughout the spectra likely relate to coordinated **tnm** signals due to the similarity in their chemical shifts, although the lack of resolution makes it difficult to get clear integration values or identify the peaks by the splitting pattern.

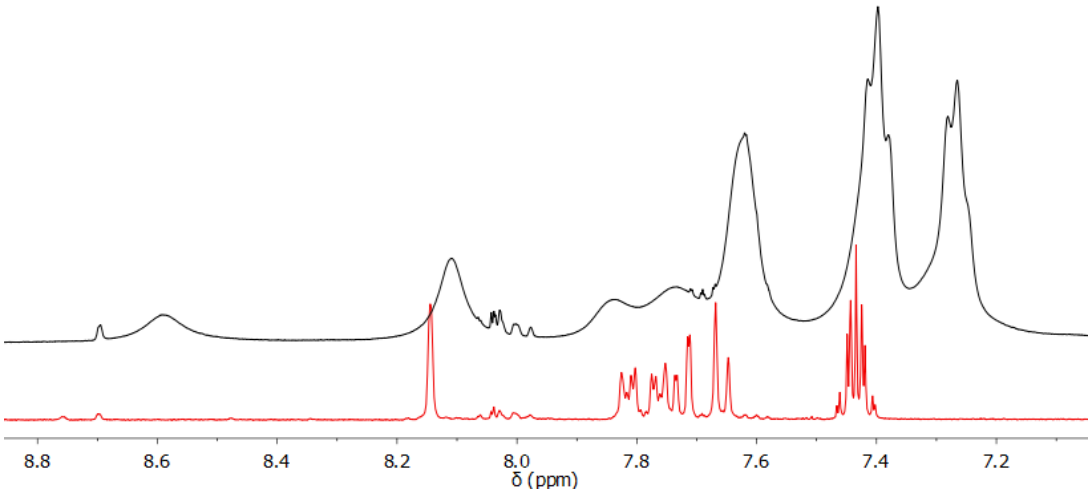

*Figure 6.4: ^{1}H NMR spectra of the complex [Sm(**tnm**)$_3$(DMSO)$_2$] (black trace) and **tnm** (red trace).*

[Y(tbm)$_3$(DMSO)(H$_2$O)]·(EtOH)

Shown in Figure 6.5 is the ^{1}H NMR spectrum of the complex [Y(**tbm**)$_3$(DMSO)(H$_2$O)]·(EtOH) (black trace) overlaid with the spectrum of **tbm** (red trace). Small peaks present in the complex spectrum indicate trace amounts of the deprotonated ligand are present in an uncoordinated state. The strong appt triplets (~7.25 – 7.00 ppm, black trace) appear to be a shifted form of the weaker appt triplets (~7.40 – 7.25 ppm, red trace) due to a similar integration ratio (1:2) and a distance of 1.1 ppm between the central peak of each appt triplet. Unfortunately, the broad peak (~7.30 ppm, black trace) could not be resolved, preventing further analysis on this complex.

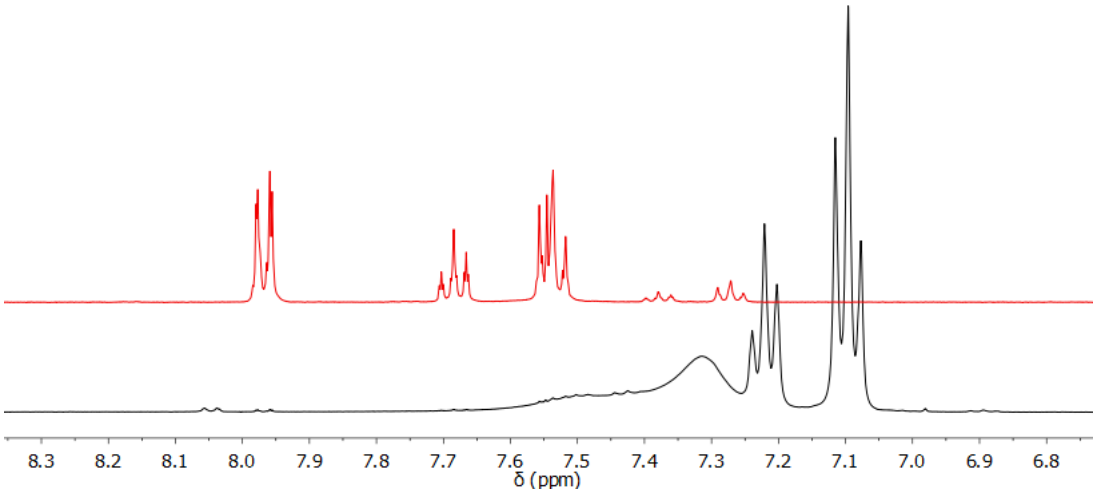

*Figure 6.5: ^{1}H NMR spectra of the complex [Y(**tbm**)$_3$(DMSO)(H$_2$O)]·(EtOH) (black trace) and **tbm** (red trace).*

6.3. Phen Co-Ligands

[Sm(dbm)$_3$(phen)]·(EtOH)

Shown in Figure 6.6 is the ^{1}H NMR spectra of the complex [Sm(**dbm**)$_3$(phen)]·(EtOH) (black trace), overlaid with the spectra of **dbm** (red trace) and phen (green trace) with the chemical shift (ppm) and relative integration values presented in Table 6.1.

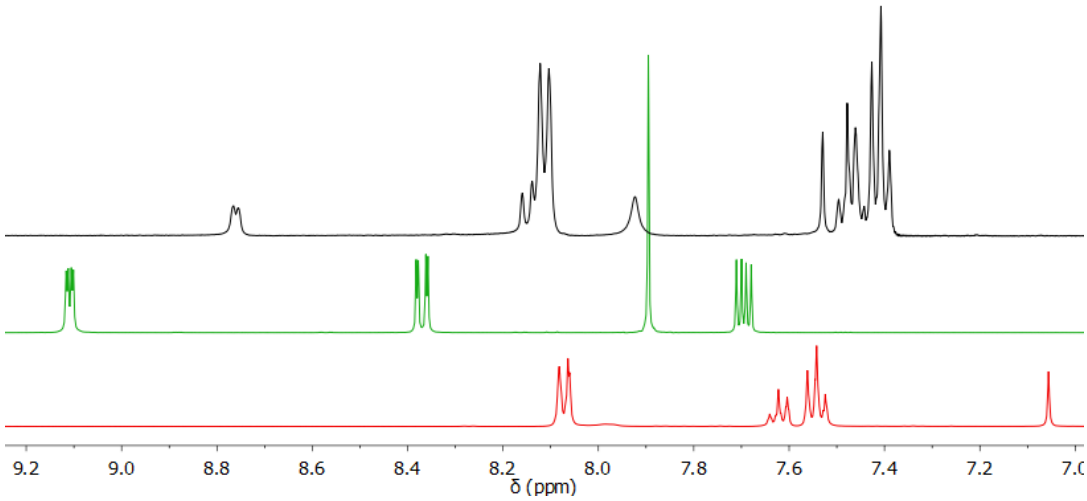

*Figure 6.6: ^{1}H NMR spectra of [Sm(**dbm**)$_3$(phen)]·(EtOH) (black trace), **dbm** (red trace), and phen (green trace).*

Phen (green trace) has four peaks in the ^{1}H NMR spectrum all of which integrate for 2H; two appt doublet of doublets (9.55 and 8.52 ppm), one singlet (7.90 ppm), and a four peak multiplet (7.70 ppm). Of these, two can be clearly identified in the complex spectrum; the singlet (7.53 ppm, 2H, black trace) and the appt doublet of doublets (8.76 ppm, 2H, black trace) which matches the less shielded doublet of doublets present in phen. The second doublet of doublets can be seen partially covered by the appt doublet in the complex spectrum at 8.15 ppm. The final multiplet cannot be clearly seen, however the integration of the multiplet around 7.51 – 7.39 ppm (20H, black trace) suggests it is a combination of the phen multiplet (7.70 ppm, 2H, green trace) and the two appt triplets of the deprotonated **dbm** (7.62 and 7.54 ppm, red trace). Factoring in the threefold integration increase for the three coordinated **dbm** ligands gives an expected integration count of 6H (appt t, 7.62 ppm, red trace) and 12H (appt t,

7.54 ppm, red trace), which combined with the 2H multiplet (7.70 ppm, green trace) of phen gives the 20H observed in the complex multiplet.

*Table 6.1: ^{1}H NMR peak integrations and shift (δ = ppm) for the complex [Sm(**dbm**)$_3$(phen)]·(EtOH) and the ligands phen and **dbm**. See Figure 6.6 for spectra.*

[Sm(**dbm**)$_3$(phen)]·(EtOH)		phen		**dbm**	
Peak	δ / integration	Peak	δ / integration	Peak	Δ / integration
Appt d	8.76 / 2H	Appt dd	9.11 / 2H	Appt d	8.07 / 4H
Appt d	8.15 / ~2H	Appt dd	8.37 / 2H	Appt t	7.62 / 2H
Appt d	8.11 / ~11H	s	7.90 / 2H	Appt t	7.54 / 4H
br s	7.92 / 3H	m	7.70 / 2H	s	7.06 / 1H
s	7.53 / 2H	--	--	--	--
m	7.51-7.39 / ~20H	--	--	--	--

The remaining peaks present in the complex spectrum are the strong appt doublet (8.11 ppm, 11H) and the broad singlet (7.92 ppm, 3H). From the relative integration, position, and peak shape, the appt doublet in the **dbm** spectrum (8.07 ppm, 4H) appears to relate to the appt doublet in the complex spectrum (8.11 ppm, ~11H). However, an accurate integration value could not be obtained due to the peak overlap observed in the complex spectrum. More interesting is the broad singlet (8.11 ppm, black trace) which can be determined as the α-H singlet from the **dbm** spectrum (7.06 ppm, 1H). The proximity of the H atom to the Sm^{3+} atom and the resonance experienced by the coordinated ligand is potentially responsible for the large downfield shift shown in the complex spectrum. Similarly, the broadening of the peak could also be due to these effects.

The overall lack of peak broadening exhibited by this complex compared to the solvent coordinated complexes could be due to the addition of phen. Bidentate co-ligands provide more stability to the coordination sphere of a complex than monodentate ligands, meaning the addition of phen could be preventing shifts in geometry that would affect the resulting ^{1}H NMR spectra.

[Sm(tbm)$_3$(phen)]

Shown in Figure 6.7 is the ^{1}H NMR spectrum of the complex [Sm(**tbm**)$_3$(phen)] (black trace), overlaid with the spectra of **tbm** (red trace) and phen (green trace). Given the splitting pattern, relative integration, and lack of change in chemical shift of the three strong multiplets in the complex spectrum (7.97, 7.69, 7.54 ppm, black trace), it is likely they belong to uncoordinated **tbm** molecules. This implies that the free molecules potentially originated from the complex, subsequently disassociating when in solution.

Aside from the three main multiplets, no other peaks could be clearly identified due to a lack of resolution and unknown integration values. From the splitting pattern the weak appt doublet at 7.79 ppm (black trace) could be related to phen, however this could not be proven. Similarly, the small multiplets from 7.40 - 7.00 ppm (black trace) could be related to the small multiplets seen at 7.38 and 7.27 ppm (red trace), however no clear relation can be determined.

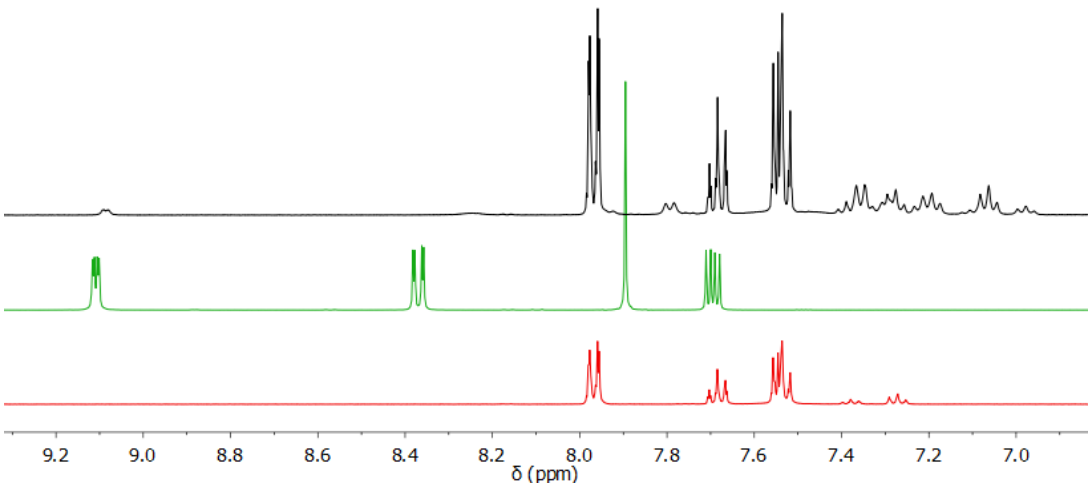

*Figure 6.7: ^{1}H NMR spectra of the complex [Sm(**tbm**)$_3$(phen)] (black trace), **tbm** (red trace) and phen (green trace).*

[Y(tbm)$_3$(phen)]

Shown in Figure 6.8 is the ^{1}H NMR spectrum of [Y(**tbm**)$_3$(phen)] (black trace) overlaid with the spectra of **tbm** (red trace) and phen (green trace). Unlike the other Y^{3+} complex presented here, there is a clear correlation between the coordinated and uncoordinated ligands.

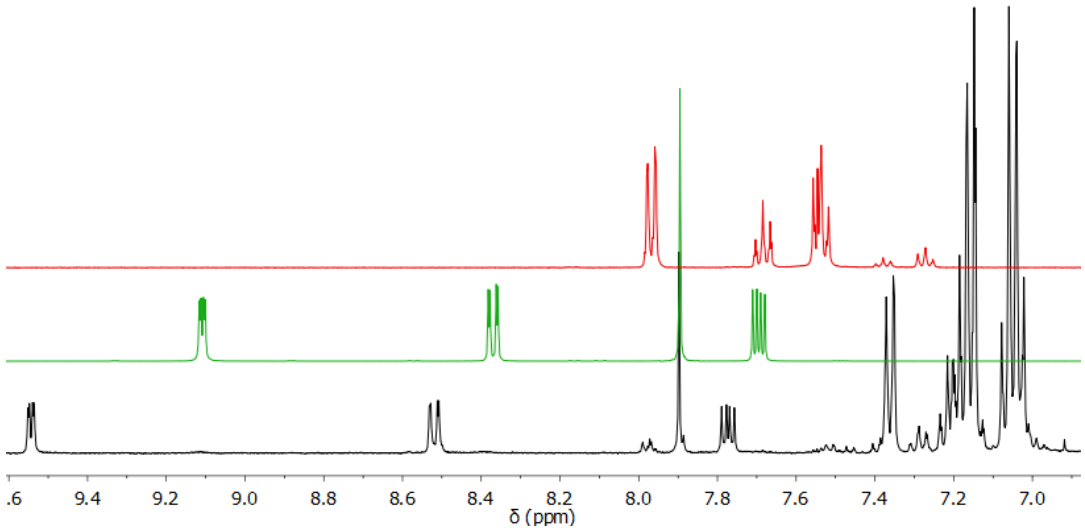

*Figure 6.8: ^{1}H NMR spectra of the complex [Y(**tbm**)$_3$(phen)] (black trace), **tbm** (red trace) and phen (green trace).*

Presented in Table 6.2 is the integration and chemical shift of the peaks present in Figure 6.8. As previously mentioned, phen has four peaks present in a ^{1}H NMR spectrum, each of which integrate for two hydrogen atoms, reflective of its symmetrical shape. All four of these peaks are visible in the complex spectrum with the same integration and at a higher ppm, except for the singlet which did not experience a shift.

*Table 6.2: ^{1}H NMR peak integrations and shift (δ) for the complex [Y (**tbm**)$_3$(phen)] and the ligands, phen and **tbm**. See Figure 6.8 for spectra.*

	[Y(tbm)$_3$(phen)]	phen	tbm
Peak	**δ (ppm) / integration**	**δ (ppm) / integration**	**δ (ppm) / integration**
Appt dd	9.55 / 2H	9.11 / 2H	--
Appt dd	8.52 / 2H	8.37 / 2H	--
s	7.90 / 2H	7.90 / 2H	--
m	7.77 / 2H	7.70 / 2H	--
m	7.36 / 6H	--	7.97 / 6H
m	7.17 / 18H	--	7.69 / 3H
m	7.05 / 18H	--	7.54 / 6H

Compared to the downfield shift experienced by coordinated phen, the coordinated **tbm** ligands experienced a general upfield shift. As there are three individual **tbm** molecules coordinated to the lanthanoid it was expected to see a threefold increase in the integration values of the **tbm** signals relative to the phen signals. Although this increase was observed, the initial assignment of peaks in the complex spectrum did not match the expected integration. The doublet-like multiplet at 7.36 ppm (6H, black trace) was initially thought to be the doublet-like multiplet at 7.97 ppm (6H, red trace). However, comparison of the integration values revealed no increase, suggesting this was not the case. The two multiplets (7.17 and 7.05 ppm, black trace) integrated to 18H, indicating that they belong to the previously mentioned multiplet (7.97 ppm, 6H, red trace) and the multiplet at 7.54 ppm (6H, red trace). No peaks could be clearly related to the multiplet at 7.69 ppm (3H, red trace), but given the noise present from 7.40 - 7.00 ppm, it is possible that they could be hidden by the other signals.

6.5. Summary

The main issue hindering analysis of the ^{1}H NMR spectra presented here was the loss of resolution due to peak broadening. This appeared most frequently in complexes that possessed monodentate solvent ligands such as DMSO, H_2O, or EtOH, and while it was possible to loosely correlate coordinated to uncoordinated peaks, as shown in the analysis of the [Yb(**tbm**)$_3$(DMSO)(H_2O)]·(EtOH) spectrum, more detailed studies would be needed to make definitive assignments.

Conversely, the incorporation of phen tended to improve the resulting ^{1}H NMR spectra, negating the issues mentioned previously, although this was not always the case, as demonstrated by the missing peaks in the [Sm(**tbm**)$_3$(phen)] spectrum. These observations are most likely due to the difference in coordination between phen and solvent coordinated complexes. As monodentate ligands, solvent molecules such as DMSO, H_2O, or EtOH are likely to undergo more rapid exchange in solution than other bidentate ligands. Although acetonitrile is a weak coordinating solvent for lanthanoids, it's possible that an exchange of solvent ligands was occurring, affecting the coordination sphere of the complex and thus adversely affecting the resulting spectra. Comparatively, phen as a bidentate ligand has a stronger coordination than solvent molecules, making it less likely that an exchange of ligands would occur.

In cases where the assignment of peaks was possible, work was done to determine whether a correlation between the coordinated and uncoordinated ligands was possible. This was only achievable for two complexes, [Sm(**dbm**)$_3$(phen)] and [Y(**tbm**)$_3$(phen)] with the location and shift of the coordinated phen peaks compared to the uncoordinated phen peaks being shown in Table 6.3. Given that NMR signals vary depending on molecular geometry, it is not surprising that the singlet from phen, which corresponds to the H atoms furthest removed from the donor atoms, seemingly maintains a chemical shift around 7.90 ppm. Although the remaining peaks shifted in different directions, downfield for the Y^{3+} complex or upfield for the Sm^{3+} complex, it was still possible to identify the related peaks, suggesting these complexes maintained their coordination upon dissolution.

*Table 6.3: Comparison of the peak locations of phen in the ^{1}H NMR spectra of the isolated ligand versus the two complexes; [Sm(**dbm**)$_3$(phen)] and [Y(**tbm**)$_3$(phen)]. Values given in δ (ppm).*

	[Sm(dbm)$_3$(phen)]			[Y(tbm)$_3$(phen)]	
Peak	**Shift**	**Complex**	**Phen**	**Complex**	**Shift**
Appt dd	0.35	8.76	9.11	9.55	0.44
Appt dd	0.22	8.15	8.37	8.52	0.15
s	0.02	7.92	7.90	7.90	0.00
m	0.19 – 0.31	7.51 – 7.39	7.70	7.77	0.07

In conclusion, the coordination of monodentate solvent molecules made the analysis of lanthanoid complexes *via* ^{1}H NMR spectroscopy difficult to achieve. The origin of this is most likely the exchange of solvent ligands within the solution. Coordination of a bidentate ancillary ligand, phen, improved the resolution of the resulting spectra, allowing for confirmation of the coordination sphere of a complex, however this did not always prove reliable.

To further investigate this phenomenon, complexes with alternative bidentate co-ligands such as bipyridine could be explored to see whether the improved spectral resolution was due to phen itself, or the replacement of two monodentate ligands with a bidentate ligand. Variable temperature NMR measurements could be utilised, increasing and decreasing the temperature of the sample to alter ligand exchange rates. Alternative NMR spectroscopy techniques could also be used, diffusion ordered spectroscopy (DOSY) for example, provides information about the diffusion coefficients of individual species in the solution. Analysis using this technique could be used to determine whether an exchange of ligands is occurring in complexes, especially in the case of solvent coordinated complexes, where a ligand exchange could occur with the deuterated solvent.

7.0. Summary and Future Work

The research presented in this thesis was conducted in order to extend the currently known pool of information about lanthanoid *β*-triketonate complexes. The structural and photophysical characterisation of 25 new Ln^{3+} complexes is presented here, alongside the synthesis of a new ligand that will see future use in this field. Previous investigations into this field focused on the effect of the *β*-triketonate ligand, looking at modifications to the structure of the ligand and the resulting complexes. To act as a counterpart, the research presented here focused on the effect of the co-ligands that were often found coordinated to the Ln^{3+} complexes alongside the *β*-triketonate ligands.

Initial work began on the isolation of lanthanoid complexes with the formula [Ln(**tbm**)$_3$(DMSO)$_2$], following the goal of investigating the difference in characteristics against a series of complexes with the formula [Ln(**tnm**)$_3$(DMSO)$_2$] and [Ln(**tbm**)$_3$(phen)]. By comparing the differing solvent, ancillary, and *β*-triketonate ligands against each other, it was hoped to deepen the understanding of what role each ligand plays in the overall sensitisation of the Ln^{3+} centre. Unfortunately, the isolation of [Ln(**tbm**)$_3$(DMSO)$_2$] complexes proved more difficult than expected, instead resulting in multiple complexes with the formula [Ln(**tbm**)$_3$(DMSO)(EtOH)] or [Ln(**tbm**)$_3$(DMSO)(H_2O)]·(EtOH). These complexes proved isostructural when solvated with H_2O, however solvation with EtOH presented structural differences based upon the size of the central Ln^{3+}. Although these structures highlighted the difficulties of isolating specifically solvated Ln^{3+} complexes, the successful formation of [Ln(**tnm**)$_3$(DMSO)$_2$] (Ln = La^{3+}, Sm^{3+}) proved that it was possible to achieve the desired complex, leaving pathways open for future research into this field.

Next began the investigation of 1,10-phenanthroline as a co-ligand in *β*-triketonate complexes. Although initially chosen for their stability and accessibility, initial complexes with the formula [Ln(**tbm**)$_3$(phen)] presented poorer luminescent properties than expected. This led to the question, “was phen affecting the photophysical properties of these complexes?”. Through an investigation utilising deuterated phen in complexes with the same molecular formula of [Ln(**tbm**)$_3$(*d*-phen)] (Ln = Sm^{3+}, Eu^{3+}, Yb^{3+}), the photophysical

properties of the *d*-phen complexes were shown to change significantly depending on the coordinated Ln^{3+}. In the case of Yb^{3+}, luminescent lifetimes more than doubled while the quantum yield increased by a factor of ~4. This was mirrored to a minor degree by Sm^{3+} which saw elongated lifetimes, although a lack of data hindered a comparison of the quantum yields. Comparitively, the Eu^{3+} complex saw no significant changes, indicating the presence of phen has a greater effect on NIR emitting lanthanoids over visible emitting lanthanoids. However, to conclude this with any certainty, Nd^{3+} and Er^{3+} will need to be investigated alongside further quantum yield studies into the existing compounds. While this study focused on **tbm** coordinated complexes, the napthoyl derivatives presented in Chapter 4 provide another area of exploration with regards to the effect on phen. Experiments for the isolation of crystalline complexes with the formula [Ln(**tnm**)$_3$(phen)] were attempted. Although ultimately unsuccessful, the isolation of a series of complexes with **tnm**H and phen coordinated could lead to more evidence on the effect of phen, as well as another comparative series with phen and *d*-phen complexes.

Breaking away from synthesising *β*-triketonate complexes, the isolation of *β*-diketonate complexes with the formula [Ln(**dnm**)$_3$(DMSO)$_2$] was investigated. This series acted as a counterpart to a series of *β*-triketonate complexes with the formula [Ln(**tnm**)$_3$(DMSO)$_2$]. Studies of the difference in luminescent properties between the **dnm** and **tnm** complexes was undertaken in order to better understand the effect created by the removal of the α-C-H oscillator on the luminescent properties of emissive Ln^{3+}. Although five new complexes were presented, there was no conclusive evidence to suggest that the *β*-triketonate systems showed consistent improvement from the *β*-diketonate systems. The Sm^{3+} complexes were effectively quenched by BET processes and while the *β*-diketonate Eu^{3+} complex showed improvement in a solution at RT and 77K, the *β*-triketonate Eu^{3+} complex was better in the solid-state. The Nd^{3+} complex showed no improvement between the two complexes, although this could be due to a poor overall excitation efficiency. Unfortunately, the Yb^{3+} *β*-diketonate complex was unable to be isolated within the time frame of this research, however, in order to complete this series of comparisons, a detailed analysis of the [Yb(**dnm**)$_3$(DMSO)$_2$] complex is needed, leaving more work for the future.

To continue exploring new β-triketonate systems, the synthesis of a new ligand, bis-tribenzoylmethane (**Btbm**H_2), was attempted. Though the desired compound was successfully synthesised, no Ln^{3+} complexes incorporating this ligand could be isolated within the time available. Isolation of Ln^{3+} complexes utilising the β-diketonate precursor of **Btbm**H_2, bis-dibenzoylmethane (**Bdbm** H_2), was attempted, resulting in the isolation of two complexes. Possessing the formula [Ln_2(**Bdbm**)$_3$(phen)$_2$] (Ln = Eu^{3+}, Yb^{3+}) these complexes were the first Ln-**Bdbm** complexes to be crystallographically characterised. These helical dinuclear complexes appeared to be more rigid than comparable mononuclear complexes when dissolved in solution. The Yb^{3+} complex saw little change in its photophysical properties compared to its **dbm**-phen counterpart, although this could be due to the presence of phen quenching the emission. Comparitively, the Eu^{3+} complex saw interesting changes in the photophysical properties. Although possessing a shorter lifetime in the solid-state than the counterpart **dbm**-phen and **tbm**-phen complexes, the Eu^{3+} complex showed a significantly elongated lifetime and increased quantum yields in a RT solution, likely due to the increased rigidity provided by the complex structure. These preliminary results suggest that the bis-ketonate series may produce interesting results for future solution phase measurements, particularly for visible emitters. Although one of the main research goals is the isolation of a series of complexes possessing **Bdbm** and **Btbm** ligands for further comparisons between the β-di- and β-tri- ketonates. Another avenue of interest lies within the structural properties of the bis-ketonate ligands. The formation of a helical crystal structure for the **Bdbm** complex suggests a similar crystalline structure could be formed with **Btbm**H_2. However, the inclusion of the third keto-O arm leaves room for different structural formations to occur as shown by the **tbm** based tetranuclear assemblies discussed in Section 1.6. Following the synthetic methods used for the tetranuclear assemblies may prove successful, leading to interesting and new organometallic complexes.

Lastly, a side study was made into the coordination of Ln^{3+} complexes in solution. Known for their flexible geometry in solution and difficulty in obtaining interpretable NMR spectra, this study sought to determine whether it was possible to identify that the coordination sphere of a known Ln^{3+} complex had

remained intact upon dissolution *via* ^{1}H NMR spectroscopy. By investigating La^{3+}, Lu^{3+}, Sm^{3+}, and Y^{3+} complexes with varying ligand systems, it was concluded that identification of a complexes coordination sphere *via* ^{1}H NMR was partially achievable. For complexes with monodentate solvent ligands, interpretation of the resulting NMR spectra proved difficult, whereas those complexes with bidentate phen ligands were often interpretable. It appeared that the coordination of more stable bidentate ligands allows for the interpretation of these systems, however only phen was investigated, resulting in a sample pool that was too small to draw any conclusions.

8.0. Methodology

8.1. General Procedures

All reagents and solvents were purchased from chemical suppliers at high purity and used without further purification unless specified. Dry and pure THF was obtained using a PureSolv MD5 solvent purification system from Innovative Technology Incorporated. The following molecules were previously reported: tribenzoylmethane (**tbm**H),[12] dinaphthoylmethane (**dnm**H),[90] trinaphthoylmethane (**tnm**H),[69] bis-dibenzoylmethane (**Bdbm**H_2).[86] Hydrated $LnCl_3$ (Ln = La^{3+}, Pr^{3+}, Nd^{3+}, Sm^{3+}, Eu^{3+}, Gd^{3+}, Tb^{3+}, Dy^{3+}, Er^{3+} Yb^{3+}, Lu^{3+}) were prepared by dissolving Ln_2O_3 in HCl (5 M) and concentrating *in vacuo*. Hydrated $Y(NO_3)_3$ was obtained from chemical suppliers and used as received. DMSO solvated $Ln(NO_3)_3$ (Ln = Sm^{3+}, Eu^{3+}, Gd^{3+} Yb^{3+}, Y^{3+}) was prepared by dissolving hydrated $Ln(NO_3)_3$ in DMSO (15 eq.) with ethanol and water before concentrating *in vacuo*.

Melting points were recorded on a VWR-IA9100 instrument using open ended capillaries.

Infrared (IR) spectra were collected using FTIR-ATR, on a PerkinElmer Spectrum Two™ Infrared Spectrometer. IR spectra were recorded from 4000 to 0 cm^{-1} with the intensities of the bands being reported as weak (w), medium (m), strong (s), or broad (br).

Nuclear magnetic resonance (NMR) spectra were recorded using a Bruker Avance 400 spectrometer (400 MHz for ^1H, 101 MHz for ^{13}C) at 298 K. All data was acquired and processed using MestReNova v12.01 software. Chemical shifts were recorded on the δ scale relative to the deuterated solvent.

Elemental analysis was performed by Robert Herman and Dr Chiara Caporale at Curtin University. Results were obtained with a standard PE 2400 CHN Elemental Analyser. The combustion tube packing was supplied with the instrument and consisted of the following components: EA-1000 (chromium oxidiser), silver tungstate on magnesium oxide and silver vanadate. PerkinElmer Copper Plus (+) and Cuprox were used in the reduction tube. Unless otherwise noted in the discussion, the compounds were sampled in standard fashion using

tin capsules for non-volatile materials. Between 1 and 2 mg of sample were weighed with a PerkinElmer AD-6 Autobalance.

Heated electro spray ionisation - high resolution mass spectrometry (HESI-HRMS) was ran by Dr Frankie Busetti at Edith Cowan University using a Thermo Scientific Q-Exactive Orbitrap mass spectrometer (Thermo Fisher Scientific Corporation, Waltham USA). Stock solutions were prepared by dissolving 1 mg of compound into 1 mL of MeCN. Solutions were diluted down to 10 ng/mL in MeOH containing 0.1% formic acid and infused at 3 µL/min into the mass spectrometer using a built-in syringe pump. Full calibration of the LTQ Orbitrap XL in the 70 – 3000 m/z range was conducted prior to measurement with the positive and negative ion calibration solutions provided by Thermo Scientific (Australia). Optical lenses were optimised with the positive calibration solution prior to each batch of samples. For increased mass accuracy on the Q-Exactive Orbitrap mass spectrometer, a plasticizer interfering peak present in the background (n-butyl benzenesulfonamide, $C_6H_5SO_2NH(CH_2)_3$, $[M+H]^+$ = 214.0896 m/z), was used for the lock mass function. The screening analysis was conducted operating the Q-Exactive Orbitrap mass spectrometer in full scan mode from 70 – 1000 m/z with a mass resolution of 70.000 (@ 200 m/z). A mass resolution of 17.500 (@200 m/z) was used for fragmentation experiments. For substance identification the deviation of the measure mass was compared against the theoretical mass (<2 ppm, relative error). To confirm elemental composition, the measured isotope pattern was also compared with that obtained from the isotopic simulation. Data was processed using the Xcalibur QualBrowser software.

Mercury 3.10.3 was used to to measure all inter- and intra-molecular distances as well as generate the crystallographic images presented in this thesis.

CShM values were obtained by exporting the x,y,z coordinates of a given crystal from Mercury 3.10.3, setting the metal centre of the complex as the centre of the axis. The x,y,z, coordinates were then entered into Shape Version 2.1, a program which uses Eq 2.1 (Section 2.4.1.) to compare the position of coordinating atoms relative to the position of vertices on a corresponding ideal polyhedron.

8.2. Spectroscopic Measurements

Absorption spectra were recorded at room temperature using a Perkin Elmer Lambda 35 UV/Vis spectrometer. Molar absorptivity determination was verified by linear least-squares fit of values obtained from at least three independent solutions at varying concentrations with absorbance of less than 1.0 for each absorption band.

Uncorrected steady-state emission and excitation spectra were recorded using an Edinburgh FLSP980-stm spectrometer equipped with a 450 W xenon arc lamp, double excitation and emission monochromators, a Peltier cooled Hamamatsu R928P photomultiplier (185–850 nm), and a Hamamatsu R5509-42 photomultiplier for detection of NIR radiation (800–1400 nm).[4] Emission and excitation spectra were corrected for source intensity (lamp and grating) and emission spectral response (detector and grating) by a calibration curve supplied with the instrument. Solid-state quantum yields were measured with the use of an integrating sphere coated with BenFlect.[91] For the overall quantum yield of Yb^{3+} complexes the use of both NIR and visible detectors was required. Therefore, a correction factor to calculate the ratio between the measured quantum yield and a reported sample needed to be applied. [Yb(phen)$(tta)_3$], where tta is thenoyltrifluoroacetone, possesses a quantum yield of 1.6% in toluene and was used as the reference.[92] Overall quantum yields in solution were determined following the optically dilute method proposed by Crosby and Demas,[87] using Equation 8.1.

$$\Phi_s = \Phi_r \left(\frac{I_s}{I_r}\right)\left(\frac{A_r}{A_s}\right)\left(\frac{n_s}{n_r}\right)^2 \qquad 8.1$$

Where Φ_r is the photoluminescent quantum yield of the reference, I is the integrated area under the emission spectrum, A is the absorbance, and n the refractive index of the solvent. The subscripts s and r refer to the sample and reference. For Sm^{3+} and Eu^{3+} the standard $[Ru(bpy)_3]Cl_2$ in H_2O (3×10^{-6} M, Φ = 2.8%) was used. For Nd^{3+} and Yb^{3+} the standard [Yb$(tta)_3$(phen)] in toluene (10^{-5} M, Φ = 1.6%) was used. Absorption and emission spectra of each complex were measured at 375 or 390 nm using 10^{-5} M solutions of DCM or MeCN under the

same experimental conditions as the standard. Experimental uncertainties are estimated to be ± 15% for quantum yields.

Excited-state decays (τ) were recorded on the same Edinburgh FLSP980-stm spectrometer using a microsecond flashlamp. The precision of fit was assessed by minimizing the reduced χ^2 function and by visual inspection of the weighted residuals. Experimental uncertainties are estimated to be ± 8% for lifetime determinations.

To record the luminescence spectra at 77 K, the samples were placed in quartz tubes (2 mm diameter) and inserted in a special quartz Dewar filled with liquid nitrogen. All solvents used in the preparation of solutions for the photophysical investigations were of spectrometric grade.

8.3. Ligand Synthesis

Tribenzoylmethane (tbmH)

Adapted from Reid, *et al.*[12]

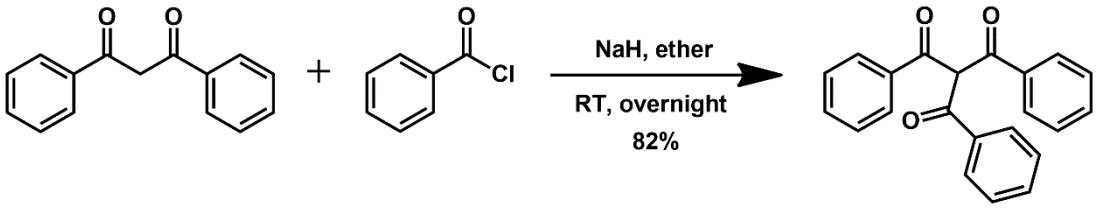

Sodium hydride (0.54 g, 60% mineral oil dispersion, 13 mmol) was added to ether (30 mL) and stirred for 15 minutes. A solution of **dbm**H (1.0 g, 4.5 mmol) in ether (5 mL) was added dropwise to the suspension and stirred for 15 minutes. A solution of benzoyl chloride (1.0 mL, 8.9 mmol) in ether (5 mL) was added to the reaction mixture dropwise before stirring at RT overnight. The reaction mixture was concentrated *in vacuo*. Hydrochloric acid (1 M) was added to the solid and stirred until the colour changed from yellow to white before filtering to collect a white product. The product was purified *via* recrystallisation from ethanol. 1.2 g (82%). M.p. 228-230 °C (lit. 221-223 °C).[5] ^{1}H NMR (400 MHz, Chloroform-*d*): δ (ppm) 7.95 – 7.92 (m, 6H), 7.62 – 7.58 (m, 3H), 7.49 – 7.44 (m, 6H), 7.13 (s, 1H). ATR-IR (cm^{-1}): *v* = 3064 w, 1668 s, 1595 m, 1581 w, 1448 m, 1324 w, 1285 s, 1194 m, 1181 m, 1000 m, 939 w, 840 m, 763 m, 691 m, 593 m.

Dinaphthoylmethane (dnmH)

Adapted from Yang, *et al.*[90]

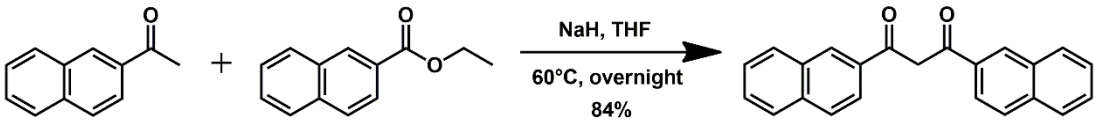

Sodium hydride (0.71 g, 60% mineral oil dispersion, 18 mmol) was added to THF (40 mL) and stirred for 15 minutes. A solution of ethyl 2-naphthoate (1.8 g, 8.9 mmol) in THF (5 mL) was added dropwise to the suspension and stirred for 15 minutes. A solution of 2-acetonaphthone (0.75 g, 4.4 mmol) in THF (5 mL) was added to the reaction mixture dropwise before heating at 60 °C overnight. The reaction mixture was cooled to room temperature and concentrated *in vacuo*. Hydrochloric acid (1 M) was added to the solid and stirred until the colour changed to yellow/mustard before extracting with ethyl acetate, drying over magnesium sulfate and concentrating *in vacuo* to yield a golden glitter like solid. The product was purified *via* recrystallisation from ethanol. 1.2 g (84% yield). M.p. 167-169 °C. ^{1}H NMR (400 MHz, DMSO-d_6): δ (ppm) 8.90 (s, 2H), 8.28 – 8.25 (appt dd, 2H), 8.18 – 8.16 (m, 2H), 8.12 – 8.10 (m, 2H), 8.06 – 8.04 (m, 2H), 7.72 – 7.64 (m, 6H). ATR-IR (cm^{-1}): *v* = 3054 w, 1597 w, 1521 w, 1496 w, 1429 w, 1386 w, 1188 w, 1130 w, 1064 w, 951 w, 919 w, 834 w, 824 w, 786 m, 768 w, 740 w, 715 w, 477 w.

Trinaphthoylmethane (tnmH)

Adapted from Abad Galán, *et al.*[69]

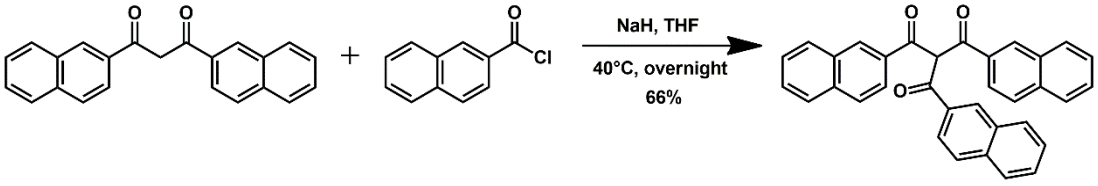

TnmH was synthesised using a modified version of the **tbm**H procedure. THF was used as a solvent instead of ether, and the mixture was heated at 40 °C overnight, all other steps remained the same. The masses used were; **dnm**H (0.62 g, 1.9 mmol), 2-naphthoyl chloride (0.72 g, 3.8 mmol), NaH (0.23 g, 60% mineral oil dispersion, 5.7 mmol). The final product was a creamy white solid. 0.60 g (66%). M.p. 286-287 °C (lit. 289-291 °C).[4] ^{1}H NMR (400 MHz, DMSO-d_6): δ

(ppm) 8.96 (s, 3H), 8.67 (s, 1H), 8.11 – 8.02 (m, 12H), 7.73 – 7.69 (m, 3H), 7.64 – 7.60 (m, 3H). ATR-IR (cm^{-1}): *v* = 3061 w, 1673 s, 1660 s, 1627 m, 1598 w, 1470 m, 1354 m, 1292 s, 1240 w, 1179 m, 1122 m, 1008 w, 948 w, 927 w, 908 w, 861 w, 820 m, 741 m, 665 w, 628 w, 584 w, 471 w.

Bis-dibenzoylmethane (BdbmH$_2$)

Adapted from Basset, *et al.*[86]

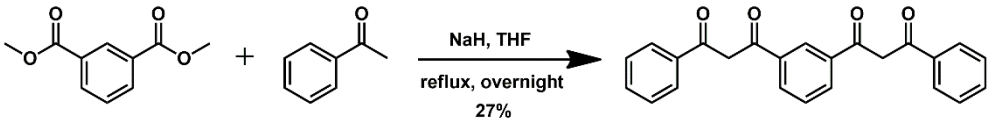

Sodium hydride (2.1 g, 60% mineral oil dispersion, 52 mmol) was added to THF (50 mL) and stirred for 15 minutes. A solution of dimethyl isophthalate (2.0 g, 10 mmol) in THF (15 mL) was added to the suspension and stirred for 30 minutes. Acetophenone (3.0 mL, 26 mmol) was added dropwise before heating at reflux overnight. The reaction mixture was cooled to room temperature and ethanol (5 mL) was added before stirring for 5 min at room temperature. Hydrochloric acid (3 M) was added until the solution colour had changed from dark brown to yellow/orange. The solid was collected *via* vacuum filtration and recrystallised from ethanol, yielding a dark brown powder. 1.0 g (27%). M.p. 178 °C. ^{1}H NMR (400 MHz DMSO-d_6): δ (ppm) 8.77 (br s, 1H), 8.44 (dd, J = 8.0, 1.8 Hz, 2H), 8.22 (appt d, 4H), 7.78 (appt t, 1H), 7.69 (appt t, 2H), 7.60 (appt t, 4H), 7.48 (s, 2H). ATR-IR (cm^{-1}) *v* = 3076 w, 1597 s, 1515 s, 1471 s, 1270 w, 1237 w, 1211 m, 1095 w, 1067 w, 1023 w, 999 w, 906 w, 755 s, 691 w, 676 w.

Bis-tribenzoylmethane (BtbmH$_2$)

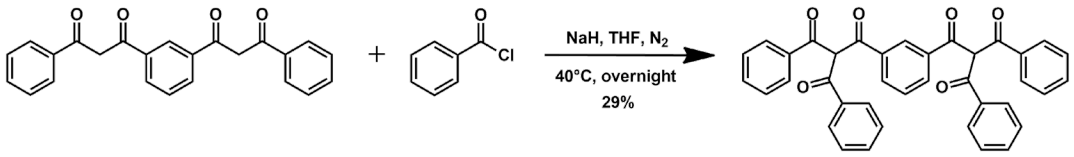

Sodium hydride (0.10 g, 60 % mineral oil dispersion, 2.4 mmol) was added to dry THF (30 mL) and stirred for 15 minutes under a nitrogen atmosphere. A solution of **Bdbm**H$_2$ (0.30 g, 0.81 mmol) in dry THF (10 mL) was added to the suspension

and stirred for 30 minutes. A solution of benzoyl chloride (0.28 mL, 2.4 mmol) in dry THF (10 mL) was added dropwise before heating overnight at 40 °C. The reaction mixture was cooled to room temperature and ethanol (2 mL) was added before stirring for 5 min at room temperature. Trifluoroacetic acid (1.5 mL) was slowly added whilst stirring vigorously. The solution was concentrated *in vacuo* before purifying *via* recrystallization with THF and hexane, yielding a pale-creamy white powder. 0.14 g (29 % yield). M.p. 223 °C. ^{1}H NMR (400 MHz DMSO-d_6): δ (ppm) 8.59 (br s, 1H), 8.33 (dd, J = 8.0, 1.8 Hz, 2H), 8.26 (s, 2H), 8.01 (appt d, 8H), 7.78 (appt t, 1H), 7.68 (appt t, 4H), 7.54 (appt t, 8H). ^{13}C NMR (100 MHz DMSO-d_6): δ (ppm) 193.8 (C=O), 193.4 (C=O), 135.9 (*Ar*), 135.3 (*Ar*), 134.2 (*Ar*-H), 133.9 (*Ar*-H), 130.0 (*Ar*-H), 129.0 (*Ar*-H), 128.7 (*Ar*-H), 128.4 (*Ar*-H), 65.4 (C-H). ATR-IR (cm^{-1}): *v* = 3060 w, 1692 m, 1667 s, 1594 m, 1555 m, 1447 m, 1323 w, 1279 s, 1181 m, 1151 m, 1048 w, 1000 w, 986 w, 839 w, 794 w, 763 w, 685 m, 596 m, 585 m. HRMS (HESI): $[M+H]^+$ Calculated for $C_{38}H_{26}O_6$, requires: 579.1802; found: 579.1800.

8.4. Lanthanoid Complexation and Crystal Growth

Three general procedures were used for the synthesis of the lanthanoid complexes and subsequent growth of single crystals. These procedures utilised a range of solvents (EtOH, MeOH, DMSO, MeCN, acetone, ether, THF), various ligands (**dbm**H, **tbm**H, **dnm**H, **tnm**H, **Bdbm**H_2, **Btbm**H_2, phen, *d*-phen), and three different Ln^{3+} salts; $Ln(Cl)_3(H_2O)_x$ and $Ln(NO_3)_3(H_2O)_x$, La-Nd, x = 6 or 7, Sm-Lu, x = 6; and $Ln(NO_3)_3(DMSO)_y$, La-Sm, y = 4, Eu-Lu, y = 3. Where possible, characterisation in the form of M.p., IR spectroscopy, and elemental analysis were carried out.

8.4.1. General Procedure 1: Dissolution

Adapted from Abad Galan, *et al.*[69]

The Ln^{3+} salt (10-15 mg), ligand (~3 eq.), and triethylamine (~6 eq.) were dissolved in DMSO (minimal amount) at RT. A secondary solvent (EtOH, MeCN, ether) was carefully added to the solution forming two layers. The system was sealed from the atmosphere and allowed to slowly mix over a few days affording yellow crystals. In instances where crystals did not form, the solution was opened to the atmosphere and allowed to slowly evaporate which occasionally resulted in crystal growth.

[Dy(tbm)$_3$(DMSO)(H$_2$O)]·(EtOH)

Ln^{3+}: $Dy(Cl)_3(H_2O)_6$ (11 mg, 2.9 x 10^{-5} mol). Ligand: **tbm**H (28 mg, 8.5 x 10^{-5} mol). NEt_3 (25 µL, 1.8 x 10^{-4} mol). Solvents: DMSO, EtOH. Yield: 6.0 mg (15%). M.p. 166-169 °C. ATR-IR (cm^{-1}): *ν* = 3404 m, 3057 w, 3026 w, 1630 w, 1596 m, 1585 m, 1547 s, 1447 m, 1360 s, 1314 m, 1293 m, 1280 m, 1178 w, 1155 w, 1073 w, 1027 w, 1011 w, 968 w, 924 w, 896 m, 821 w, 782 w, 746 m, 692 m, 678 w, 667 w, 633 w, 616 w, 563 w, 550 w, 421 w. Elemental analysis calc (%) for $C_{70}H_{59}O_{12}SDy$: C, 65.34; H, 4.62; N, 0; found: C, 64.26; H, 4.48; N, 0.32.

[Er(tbm)$_3$(DMSO)(EtOH)]

Ln^{3+}: $Er(Cl)_3(H_2O)_6$ (26 mg, 6.8 x 10^{-5} mol). Ligand: **tbm**H (39 mg, 1.2 x 10^{-4} mol). NEt_3 (20 µL, 1.4 x 10^{-4} mol). Solvents: DMSO, EtOH. Yield: 9.0 mg (18%). M.p. 160-162 °C. ATR-IR (cm^{-1}): *ν* = 3409 w, 3056 w, 1584 m, 1548 s, 1447 m, 1363 s, 1314 m, 1279 m, 1178 w, 1154 w, 1073 w, 1027 w, 1012 w, 967 w, 924 w, 896 m, 821 w, 782 w, 744 w, 691 w, 677 w, 666 w, 639 w, 551 w, 425 w. Elemental analysis calc (%) for $C_{70}H_{57}O_{11}SEr$: C, 65.10; H, 4.60; N, 0; found: C, 64.91; H, 4.43; N, 0.

[Eu(dnm)$_3$(DMSO)$_2$]

Ln^{3+}: $Eu(Cl)_3(H_2O)_6$ (20 mg, 5.5 x 10^{-5} mol). Ligand: **dnm**H (41 mg, 1.3 x 10^{-4} mol). NEt_3 (40 µL, 2.9 x 10^{-4} mol). Solvents: DMSO, EtOH. Yield: 21 mg (39%). M.p. 158-160 °C. ATR-IR (cm^{-1}): *ν* = 3054 w, 1629 w, 1598 m, 1583 m, 1557 m, 1514 m, 1494 s, 1444 s, 1403 s, 1340 m, 1289 m, 1230 w, 1182 w, 1154 w, 1128 w, 1099 w, 1010 m, 956 w, 916 w, 866 w, 827 w, 786 m, 763 w, 737 w, 708 w, 594 w, 509 w, 467 w. Elemental analysis calc (%) for $C_{73}H_{57}O_8S_2Eu$: C, 68.59; H, 4.49; N, 0.; found: C, 66.93; H, 4.30; N, 0.04.

[Eu(tbm)$_3$(DMSO)(H$_2$O)]·(EtOH)

Ln^{3+}: Eu(Cl)$_3$(H$_2$O)$_6$ (20 mg, 5.5 x 10^{-5} mol). Ligand: **tbm**H (40 mg, 1.2 x 10^{-4} mol). NEt$_3$ (20 µL, 1.4 x 10^{-4} mol). Solvents: DMSO, EtOH. Yield: 28 mg (53%). M.p. 171-173 °C. ATR-IR (cm^{-1}): *v* = 3401 w (br), 3057 w, 1629 w, 1584 m, 1544 s, 1447 m, 1359 s, 1313 m, 1292 m, 1278 m, 1178 w, 1155 w, 1073 w, 1027 w, 1011 w, 967 w, 924 w, 895 m, 821 w, 782 w, 745 w, 692 m, 677 w, 666 w, 632 w, 616 w, 562 w, 549 w, 418 w. Elemental analysis calc (%) for $C_{70}H_{59}O_{12}SEu$: C, 65.88; H, 4.66; N, 0; found: C, 65.04; H, 4.44; N, 0.16.

[Gd(dnm)$_3$(DMSO)$_2$]

Ln^{3+}: Gd(Cl)$_3$(H$_2$O)$_6$ (22 mg, 5.9 x 10^{-5} mol). Ligand: **dnm**H (53 mg, 1.6 x 10^{-4} mol). NEt$_3$ (50 µL, 3.6 x 10^{-4} mol). Solvents: DMSO, EtOH. Yield: 55 mg (78%). M.p. 147-148 °C. ATR-IR (cm^{-1}): *v* = 3054 w, 1584 m, 1557 m, 1495 s, 1445 s, 1403 s, 1340 m, 1289 m, 1184 w, 1128 w, 1009 m, 956 w, 786 m, 764 w, 708 w. Elemental analysis calc (%) for $C_{73}H_{57}O_8S_2Gd$: C, 68.31; H, 4.48; N, 0; found: C, 66.60; H, 4.61; N, 0.01.

[La(tbm)$_3$(DMSO)$_2$]

Ln^{3+}: La(Cl)$_3$(H$_2$O)$_7$ (14 mg, 3.8 x 10^{-5} mol). Ligand: **tbm**H (28 mg, 8.5 x 10^{-4} mol). NEt$_3$ (25 µL, 1.8 x 10^{-4} mol). Solvents: DMSO:EtOH (1:1), ether. Yield: 12 mg (25%). M.p. 181-183 °C. ATR-IR (cm^{-1}): *v* = 3056 w, 3023 w, 2918 w, 1640 m, 1594 m, 1548 s, 1447 m, 1359 s, 1313 m, 1275 m, 1153 w, 1073 w, 1005 m, 959 w, 924 w, 893 m, 820 m, 780 m, 745 m, 694 m, 630 w, 562 w, 543 w. Elemental analysis calc (%) for $C_{70}H_{57}O_{11}S_2La$: C, 65.83; H, 4.50; N, 0; found: C, 66.08; H, 4.27; N, 0.07.

[La(tbm)$_3$(DMSO)(EtOH)]

Ln^{3+}: La(Cl)$_3$(H$_2$O)$_7$ (19 mg, 5.1 x 10^{-5} mol). Ligand: **tbm**H (45 mg, 1.4 x 10^{-4} mol). NEt$_3$ (25 µL, 1.8 x 10^{-4} mol). Solvents: DMSO, EtOH. Yield: 6.0 mg (11%). M.p. 182-184 °C. ATR-IR (cm^{-1}): *v* = 3585 w, 3523 w, 3056 w, 3023 w, 1641 w, 1582 m, 1547 s, 1447 m, 1357 s, 1313 m, 1275 m, 1152 w, 1073 w, 1026 w, 1006 w, 963 w, 925 w, 894 m, 821 w, 781 w, 748 w, 961 m, 665 w, 629 w, 615 w, 562 w, 544 w. Elemental analysis calc (%) for $C_{70}H_{57}O_{11}S_2La$: C, 65.83; H, 4.50; N, 0; found: C, 65.98; H, 4.51; N, 0.05.

[Lu(tbm)$_3$(DMSO)(EtOH)]

Ln^{3+}: $Lu(Cl)_3(H_2O)_6$ (13 mg, 3.3 x 10^{-5} mol). Ligand: **tbm**H (26 mg, 7.9 x 10^{-5} mol). NEt_3 (25 µL, 1.8 x 10^{-4} mol). Solvents: DMSO, EtOH. Yield: 15 mg (35%). M.p. 154-156 °C. ATR-IR (cm^{-1}): *ν* = 3413 w (br), 3056 w, 1585 m, 1550 s, 1447 m, 1363 s, 1314 m, 1279 m, 1155 w, 1073 w, 1012 w, 968 w, 924 w, 896 m, 822 w, 782 w, 746 w, 691 w, 634 w, 551 w, 425 w. Elemental analysis calc (%) for $C_{70}H_{57}O_{11}SLu$: C, 65.62; H, 4.48; N, 0; found: C, 63.88; H, 4.04; N, 0.10.

[Nd(dnm)$_3$(DMSO)$_2$]

Ln^{3+}: $Nd(Cl)_3(H_2O)_7$ (12 mg, 3.2 x 10^{-5} mol). Ligand: **dnm**H (27 mg, 8.3 x 10^{-5} mol). NEt_3 (50 µL, 3.6 x 10^{-4} mol). Solvents: DMSO, EtOH. Yield: 22 mg (63%). M.p. 162-163 °C. ATR-IR (cm^{-1}): *ν* = 3054 m, 1629 w, 1597 m, 1583 m, 1557 m, 1494 s, 1443 s, 1396 s, 1339 m, 1288 m, 1229 w, 1182 w, 1153 w, 1128 w, 1099 w, 1008 m, 956 w, 866 w, 827 w, 786 m, 737 w, 707 w, 594 w, 467 w. Elemental analysis calc (%) for $C_{73}H_{57}O_8S_2Nd$: C, 69.01; H, 4.52; N, 0; found: C, 67.84; H, 4.28; N, 0.09.

[Sm(dnm)$_3$(DMSO)$_2$]

Ln^{3+}: $Sm(Cl)_3(H_2O)_6$ (15 mg, 4.1 x 10^{-5} mol). Ligand: **dnm**H (39 mg, 1.2 x 10^{-4} mol). NEt_3 (20 µL, 1.4 x 10^{-4} mol). Solvents: DMSO, MeCN. Yield: 30 mg (53%). M.p. 142-143 °C. ATR-IR (cm^{-1}): *ν* = 3054 w, 1629 w, 1599 m, 1584 m, 1557 m, 1516 m, 1495 s, 1445 s, 1403 s, 1340 m, 1288 w, 1189 w, 1127 w, 1010 m, 956 m, 916 w, 856 w, 827 w, 786 m, 763 m, 734 w, 708 w, 594 w, 509 w, 467 w. Elemental analysis calc (%) for $C_{73}H_{57}O_8S_2Sm$: C, 68.67; H, 4.50; N, 0; found: C, 67.60; H, 4.02; N, 0.11.

[Sm(tbm)$_3$(DMSO)$_2$]

Ln^{3+}: $Sm(Cl)_3(H_2O)_6$ (10 mg, 2.7 x 10^{-5} mol). Ligand: **tbm**H (26 mg, 7.9 x 10^{-5} mol). NEt_3 (20 µL, 1.4 x 10^{-4} mol). Solvents: DMSO, EtOH:ether (1:1). Further measurements were unable to be made due to re-dissolution of the sample after x-ray diffraction analysis.

[Sm(tnm)$_3$(DMSO)$_2$]

Ln^{3+}: $Sm(NO_3)_3(DMSO)_4$ (11 mg, 1.7 x 10^{-5} mol) . Ligand: **tnm**H (23 mg, 4.8 x 10^{-5} mol). NEt_3 (8.0 µL, 5.7 x 10^{-5} mol). Solvents: DMSO, EtOH. Yield: 18 mg (63%).

M.p. 214-216 °C. ATR-IR (cm^{-1}): *v* = 3054 w, 1622 w, 1540 s, 1505 w, 1465 w, 1433 w, 1373 s, 1333 m, 1242 w, 1151 w, 1112 m, 1020 m, 962 w, 907 m, 862 w, 819 m, 793 m, 756 w, 730 w, 508 w, 476 m. Elemental analysis calc (%) for $C_{106}H_{75}O_{11}S_2Sm$: C, 73.2; H, 4.35; N, 0; found: C, 70.89; H,4.38; N, 0.11.

[Tb(tbm)$_3$(DMSO)(H$_2$O)]·(EtOH)

Ln^{3+}: $Tb(Cl)_3(H_2O)_6$ (16 mg, 4.3 x 10^{-5} mol). Ligand: **tbm**H (40 mg, 1.2 x 10^{-4} mol). NEt_3 (35 µL, 2.5 x 10^{-4} mol). Solvents: DMSO, EtOH. Yield: 21 mg (40%). M.p. 166-168 °C. ATR-IR (cm^{-1}): *v* = 3594 w, 3392 w(br), 3056 w, 3023 w, 1981 w, 1638 m, 1583 s, 1595 s, 1548 s, 1448 m, 1361 s, 1314 m, 1277 s, 1153 w, 1073 w, 1011 m, 967 w, 923 w, 895 m, 821 w, 781 w, 747 m, 692 m, 665 w, 632 w, 616 w, 547 w. Elemental analysis calc (%) for $C_{70}H_{59}O_{12}STb$: C, 65.52; H, 4.63; N, 0; found: C, 65.05; H, 4.36; N, 0.35.

[Yb(tbm)$_3$(DMSO)(H$_2$O)]·(EtOH)

Ln^{3+}: $Yb(Cl)_3(H_2O)_6$ (15 mg, 3.9 x 10^{-5} mol). Ligand: **tbm**H (37 mg, 1.1 x 10^{-4} mol). NEt_3 (30 µL, 2.2 x 10^{-4} mol). Solvents: DMSO, EtOH. Yield: 20 mg (42%). M.p. 135-137 °C. ATR-IR (cm^{-1}): *v* = 3410 w, 3057 w, 1585 m, 1549 s, 1447 m, 1361 s, 1314 m, 1279 m, 1155 w, 1073 w, 1012 w, 969 w, 924 w, 896 m, 821 m, 782 m, 745 m, 691 m, 634 w, 552 w, 426 w.

[Y(tbm)$_3$(DMSO)(H$_2$O)]·(EtOH)

Ln^{3+}: $Y(NO_3)_3(DMSO)_3$ (11 mg, 2.2 x 10^{-5} mol). Ligand: **tbm**H (18 mg, 5.5 x 10^{-5} mol). NEt_3 (25 µL, 1.8 x 10^{-4} mol). Solvents: DMSO, EtOH. Yield: 14 mg (66%). M.p. 164-166 °C. ATR-IR (cm^{-1}): *v* = 3402 w, 3057 w, 3026 w, 1631 w, 1585 m, 1549 s, 1447 m, 1361 s, 1314 m, 1293 m, 1279 m, 1178 w, 1155 w, 1073 w, 1027 w, 1012 w, 969 w, 924 w, 869 m, 821 w, 782 w, 745 w, 692m, 677 w, 667 w, 633 w, 616 w, 564 w, 550 w, 425 w. Elemental analysis calc (%) for $C_{70}H_{59}O_{12}Y$: C, 69.30; H, 4.90; N, 0; found: C, 68.96; H, 4.62; N, 0.10.

8.4.2. General Procedure 2: Evaporation

Adapted from Abad Galán, *et al.*[67]

The Ln^{3+} salt (10-15 mg), ligand (~3 eq.), and triethylamine (~6 eq.) were dissolved in a volatile solvent (EtOH or acetone) at ~10-20 °C below the boiling point. Either phen (~1 eq.), *d*-phen, (~1 eq.) or DMSO (5 drops) were added to the mixture and stirred for ~30 min. The system was filtered to remove remnant solid and left partially open to the atmosphere, allowing the solvent to slowly evaporate, affording yellow crystals.

[Eu(tbm)$_3$(*d*-phen)]

Ln^{3+} $Eu(NO_3)_3(DMSO)_3$ (17 mg, 3.0 x 10^{-5} mol). Ligand: **tbm**H (26 mg, 7.9 x 10^{-5} mol), *d*-phen (4.9 mg, 2.6 x 10^{-5} mol). NEt_3 (30 µL, 2.2 x 10^{-4} mol). Solvents: EtOH. Yield: 3.0 mg (8%). M.p. 252-253 °C. ATR-IR (cm^{-1}): *v* = 3058 w, 1642 m, 1583 m, 1538 s, 1448 m, 1367 s, 1276 m, 1155 w, 1073 w, 1028 w, 1013 w, 896 m, 824 w, 778 w, 743 w, 690 w, 615 w, 554 w.

[Pr(tbm)$_3$(DMSO)(EtOH)]

Ln^{3+}: $Pr(Cl)_3(H_2O)_7$ (17 mg, 4.6 x 10^{-5} mol). Ligand: **tbm**H (44 mg, 1.3 x 10^{-4} mol). NEt_3 (35 µL, 2.5 x 10^{-4} mol). Solvents: EtOH, DMSO (5 drops). Yield: 33 mg (60%). M.p. 182-184 °C. ATR-IR (cm^{-1}): *v* = 3587 w, 3525 w, 3057 w, 3024 w, 1644 w, 1593 m, 1583 m, 1547 s, 1447 m, 1357 s, 1313 m, 1276 m, 1152 w, 1074 w, 1026 w, 1006 w, 964 w, 924 w, 894 m, 821 w, 781 w, 748 w, 693 m, 665 w, 629 w, 615 w, 563 w, 544 w, 420 w. Elemental analysis calc (%) for $C_{70}H_{57}O_{11}SPr$: C, 67.41; H, 4.61; N, 0; found: C, 66.79; H, 4.39; N, 0.05.

(HNEt$_3$)[Sm(dbm)$_4$]·(EtOH)

Ln^{3+}: $Sm(NO_3)_3(DMSO)_4$ (10 mg, 1.50 x 10^{-5} mol). Ligand: **dbm**H (15 mg, 6.7 x 10^{-5} mol). NEt_3 (9.0 µL, 6.5 x 10^{-5} mol). Solvents: EtOH. Yield: 10 mg (56%). M.p. 160-161 °C. ATR-IR (cm^{-1}): *v* = 3059 w, 1595 s, 1550 m, 1515 s, 1476 m, 1455 m, 1393 m, 1280 m, 1220 m, 1068 m, 1023 m, 940 w, 746 m, 721 m, 581 m, 507 m, 511 w.

[Sm(dbm)$_3$(phen)]·(EtOH)

Ln^{3+}: $Sm(Cl)_3(H_2O)_6$ (18 mg, 4.9 x 10^{-5} mol). Ligand: **dbm**H (27 mg, 1.2 x 10^{-4} mol), phen (7.9 mg, 4.4 x 10^{-5} mol). NEt_3 (30 µL, 2.2 x 10^{-4} mol). Solvents: EtOH. Yield: 8.0 mg (19%). ATR-IR (cm^{-1}): *v* = 3058 w, 1593 s, 1547 s, 1514 s, 1477 s, 1456 s,

1405 s, 1308 m, 1219 m, 1067 m, 1023 m, 940 w, 841 m, 719 m, 687 m, 608 m, 503 w.

[Sm(tbm)$_3$(*d*-phen)]

Ln^{3+} $Sm(NO_3)_3(DMSO)_4$ (17 mg, 2.6 x 10^{-5} mol). Ligand: **tbm**H (25 mg, 7.6 x 10^{-5} mol), *d*-phen (4.8 mg, 2.5 x 10^{-5} mol). NEt_3 (25 µL, 1.8 x 10^{-4} mol). Solvents: EtOH. Yield: 3.0 mg (8%). M.p. 254-256 °C. ATR-IR (cm^{-1}): *v* = 3063 w, 3027 w, 1642 m, 1583 m, 1538 s, 1448 m, 1367 s, 1276 m, 1154 w, 1074 w, 896 m, 824 w, 782 w, 743 w, 690 w.

[Sm(tbm)$_3$(phen)]

Ln^{3+}: $Sm(Cl)_3(H_2O)_6$ (16 mg, 4.4 x 10^{-5} mol). Ligand: **tbm**H (40 mg, 1.2 x 10^{-4} mol), phen (7.8 mg, 4.3 x 10^{-5} mol). NEt_3 (30 µL, 2.2 x 10^{-4} mol). Solvents: Acetone. Yield: 15 mg (28%). M.p. 227-229 °C. ATR-IR (cm^{-1}): *v* = 3058 w, 1641 m, 1582 m, 1537 s, 1448 m, 1366 s, 1276 m, 1176 w, 1154 w, 1072 w, 1013 w, 896 m, 844 w, 824 w, 779 w, 743 m, 729 w, 692 m, 615 w, 554 w. Elemental analysis calc (%) for $C_{78}H_{53}O_9N_2Sm$: C, 71.37; H, 4.07; N, 2.13.; found: C, 72.58; H, 3.69; N, 1.81.

[Yb(tbm)$_3$(*d*-phen)]

Ln^{3+}: $Yb(NO_3)_3(DMSO)_3$ (20 mg, 3.4 x 10^{-5} mol). Ligand: **tbm**H (29 mg, 8.8 x 10^{-5} mol), *d*-phen (4.8 mg, 2.5 x 10^{-5} mol). NEt_3 (30 µL, 2.2 x 10^{-4} mol). Solvents: EtOH. Yield: 3.0 mg (10%). M.p. 251-252 °C. ATR-IR (cm^{-1}): *v* = 3058 w, 1643 m, 1583 m, 1534 s, 1448 m, 1370 s, 1276 m, 1155 w, 1073 w, 1028 w, 922 w, 897 m, 825 w, 780 w, 743 w, 691 m, 615 w, 557 w.

[Y(tbm)$_3$(phen)]

Ln^{3+}: $Y(NO_3)_3(H_2O)_6$ (14 mg, 4.0 x 10^{-5} mol). Ligand: **tbm**H (27 mg, 8.2 x 10^{-5} mol), phen (5.5 mg, 3.1 x 10^{-5} mol). NEt_3 (40 µL, 2.9 x 10^{-4} mol). Solvents: EtOH. Yield: 25 mg (72%). M.p. 260-261 °C. ATR-IR (cm^{-1}): *v* = 3059 w, 1643 m, 1583 m, 1539 s, 1449 m, 1369 s, 1310 m, 1276 m, 1176 w, 1155 w, 1073 w, 1027 w, 1014 w, 921 w, 896 m, 864 w, 844 w, 825 w, 811 w, 780 w, 743 m, 729 w, 693 m, 667 w, 615 w, 555 w, 418 w. Elemental analysis calc (%) for $C_{78}H_{53}O_9N_2Y$: C, 74.88; H, 4.27; N, 2.24; found: C, 73.70; H, 4.13; N, 2.41.

8.4.3. General Procedure 3: Bis-Ketonate Evaporation

Ln^{3+} salt (10-20 mg), **Bdbm**H (~1.5 eq.), phen (~1 eq.) and triethylamine (~6 eq.) were added to THF (20 mL) and heated at reflux over 24 hours. The resulting solution was cooled to room temperature, filtered to remove remnant solid and left partially open to the atmosphere, allowing the solvent to evaporate affording yellow to colourless long needle-like crystals.

[Eu_2(Bdbm)$_3$(phen)$_2$]

Ln^{3+}: $Eu(NO_3)_3(DMSO)_3$ (21 mg, 3.7 x 10^{-5} mol). Ligand: **Bdbm**H_2 (26 mg, 7.0 x 10^{-5} mol), phen (6.8 mg, 3.8 x 10^{-5} mol). NEt_3 (75 µL, 5.4 x 10^{-4} mol). Solvents: THF. Reaction time/temp: 24 hr, reflux. Yield: 3.0 mg (8%). Decomposes 290 °C. ATR-IR (cm^{-1}): *v* = 3054 w, 1593 s, 1549 s, 1506 s, 1470 s, 1449 s, 1386 s (br), 1304 m, 1202 w, 1052 w, 1025 w, 841 w, 729 w, 699 w, 606 w, 508 w.

[Yb_2(Bdbm)$_3$(phen)$_2$]

Ln^{3+}: $Yb(NO_3)_3(DMSO)_3$ (21 mg, 3.5 x 10^{-5} mol). Ligand: **Bdbm**H_2 (24 mg, 6.5 x 10^{-5} mol), phen (6.8 mg, 3.8 x 10^{-5} mol). NEt_3 (75 µL, 5.4 x 10^{-4} mol). Solvents: THF. Reaction time/temp: 24 hr, 70 °C. Yield: 5.0 mg (8%). Decomposes 294 °C. ATR-IR (cm^{-1}): *v* = 3065 w, 2921 w, 1771 w, 1596 s, 1554 s, 1511 s, 1471 s, 1451 s, 1392 s (br), 1307 m, 1203 m, 1066 w, 1025 w, 841 w, 754 w, 730 w, 702 w, 618 w, 519 w.

8.5. Crystallographic Data

Crystallographic data for structures were collected at the University of Western Australia by Dr. Alexandre Sobolev, Dr Stephen Moggach, and Prof. Mark Ogden. The following section is split in two based upon the method and programs used by each researcher to process the crystallographic data.

8.5.1. Structures by Dr Alexandre Sobolev

Data was collected at 100(2) K on an Oxford Diffraction Xcalibur or Gemini ultra-diffractometer fitted using Mo Kα or Cu Kα radiation**.** Following absorption

corrections and solution by direct methods, the structures were refined against *F*2 with full-matrix least-squares using the program SHELXL-97 or SHELX-2014.323. Unless stated below, anisotropic displacement parameters were employed for all non-hydrogen atoms and hydrogen atoms were added at calculated positions and refined by use of a riding model with isotropic displacement parameters based on those of the parent atom. Details on selected individual crystal structure determinations and refinements are given below. All structures were refined by Dr Alexandre Sobolev.

$(HNEt_3)[Sm(dbm)_4]\cdot(EtOH)$

Empirical formula $C_{68}H_{66}NO_9Sm$, MW = 1191.56. Crystal size 0.211 × 0.197 × 0.172 mm^3. Monoclinic, space group $P2_1$ (No. 4), a = 8.9137(1), b = 25.9037(2), c = 25.3445(2) Å, β = 90.038(1)°, V = 5851.99(9) Å^3, Z = 4, ρ_c = 1.352 g cm^{-3}, μ = 1.062 mm^{-1}. F_{000} = 2460, MoKα radiation, λ = 0.71073 Å, T = 100(2) K, $2\theta_{max}$ = 64.7°, 121795 reflections collected, 38742 unique (R_{int} = 0.0328). Final *GooF* = 1.000, $R1$ = 0.0388, $wR2$ = 0.1049, R indices based on 36875 reflections with $I > 2\sigma(I)$ (refinement on F^2), $|\Delta\rho|_{max}$= 1.9(1) e Å^{-3}, 1434 parameters, 198 restraints. Lp and absorption corrections applied. Absolute structure parameter = 0.004(2).[93]

$[Sm(dbm)_3(phen)]\cdot(EtOH)$

Empirical formula $C_{59}H_{47}N_2O_7Sm$, MW = 1046.33. Crystal size 0.146 × 0.037 × 0.037 mm^3. Monoclinic, space group $P2_1/c$ (No. 14), a = 19.3200(1), b = 10.5944(1), c = 22.8673(2) Å, β = 91.850(1)°, V = 4678.13(6) Å^3, Z = 4, ρ_c = 1.486 g cm^{-3}, μ = 9.902 mm^{-1}. F_{000} = 2132, CuK radiation, λ = 1.54178 Å, T = 100(2) K, $2\theta_{max}$ = 134.6°, 53333 reflections collected, 8360 unique (R_{int} = 0.0592) Final *GooF* = 1.001, $R1$ = 0.0408, $wR2$ = 0.0936, R indices based on 6919 reflections with $I > 2\sigma(I)$ (refinement on F^2), $|\Delta\rho|_{max}$= 1.23(9) e Å^{-3}, 624 parameters, 0 restraints. Lp and absorption corrections applied.

$[Sm(dnm)_3(DMSO)_2]$

Empirical formula $C_{75}H_{60}NO_8S_2Sm$, MW = 1317.71. Crystal size 0.241 × 0.204 × 0.146 mm^3. Triclinic, space group P-1 (No. 2), a = 9.3899(2), b = 17.6726(4), c =

18.9448(4) Å, α = 100.683(2), β = 90.856(2), γ = 94.744(2)°, V = 3077.23(12) Å^3, Z = 2, ρ_c = 1.422 g cm^{-3}, μ = 1.082 mm^{-1}. F_{000} = 1350, MoKα radiation, λ = 0.71073 Å, T = 100(2) K, 2θ_{max} = 65.4°, 38137 reflections collected, 20262 unique (R_{int} = 0.0380). Final *GooF* = 1.001, R1 = 0.0484, wR2 = 0.1064, R indices based on 16883 reflections with $I > 2\sigma(I)$ (refinement on F^2), $|\Delta\rho|_{max}$= 4.1(1) e Å^{-3}, 800 parameters, 63 restraints. Lp and absorption corrections applied.

[Sm(tbm)$_3$(DMSO)$_2$]

Empirical formula $C_{70}H_{57}O_{11}S_2Sm$, MW = 1288.62. Crystal size 0.245 × 0.185 × 0.088 mm^3. Monoclinic, space group $C2/c$ (No. 15), a = 50.7015(6), b = 10.8803(1), c = 23.8289(3) Å, β = 108.004(1)°, V = 12501.5(3) Å^3, Z = 8, ρ_c = 1.369 g cm^{-3}, μ = 1.066 mm^{-1}. F_{000} = 5272, MoKα radiation, λ = 0.71073 Å, T = 100(2) K, 2θ_{max} = 65.5º, 139737 reflections collected, 21831 unique (R_{int} = 0.0474). Final *GooF* = 1.001, R1 = 0.0352, wR2 = 0.0808, R indices based on 17815 reflections with $I > 2\sigma(I)$ (refinement on F^2), $|\Delta\rho|_{max}$= 0.83(8) e Å^{-3}, 814 parameters, 51 restraints. Lp and absorption corrections applied.

[Sm(tbm)$_3$(phen)]

Empirical formula $C_{78}H_{53}N_2O_9Sm$, MW = 1312.57. Crystal size 0.326 × 0.189 × 0.064 mm^3. Triclinic, space group P-1 (No. 2), a = 10.6145(2), b = 13.5998(2), c = 21.3632(3) Å, α = 93.150(1), β = 102.221(1), γ = 95.281(1)°, V = 2992.41(8) Å^3, Z = 2, ρ_c = 1.457 g cm^{-3}, μ = 1.047 mm^{-1}. F_{000} = 1338, MoKα radiation, λ = 0.71073 Å, T = 100(2) K, 2θ_{max} = 65.4°, 65271 reflections collected, 20269 unique (R_{int} = 0.0374). Final *GooF* = 1.001, R1 = 0.0302, wR2 = 0.0688, R indices based on 18160 reflections with $I > 2\sigma(I)$ (refinement on F^2), $|\Delta\rho|_{max}$= 1.08(9) e Å^{-3}, 811 parameters, 0 restraints. Lp and absorption corrections applied.

[Sm(tnm)$_3$(DMSO)$_2$]

Empirical formula $C_{217}H_{168}O_{26}S_5Sm_2$, MW = 3652.50. Crystal size 0.273 × 0.192 × 0.059 mm^3. Triclinic, space group P-1 (No. 2), a = 13.2079(4), b = 17.3573(5), c = 20.7486(6) Å, α = 89.751(2), β = 75.806(3), γ = 85.757(2)°, V = 4598.4(2) Å^3, Z = 1, ρ_c = 1.319 g cm^{-3}, μ = 0.759 mm^{-1}. F_{000} = 1882, MoKα radiation, λ = 0.71073 Å, T = 100(2) K, 2θ_{max} = 64.8°, 96497 reflections collected, 30304 unique (R_{int} = 0.0599). Final *GooF* = 1.001, R1 = 0.0533, wR2 = 0.1214, R indices based on 23713

reflections with $I > 2\sigma(I)$ (refinement on F^2), $|\Delta\rho|_{max}$= 1.9(1) e Å^{-3}, 1446 parameters, 378 restraints. Lp and absorption corrections applied.

[Yb(tbm)$_3$(DMSO)(H$_2$O)]·(EtOH)

Empirical formula $C_{70}H_{59}O_{12}SYb$, MW = 1297.27. Crystal size 0.243 × 0.201 × 0.045 mm^3. Triclinic, space group P-1 (No. 2), a = 12.6131(3), b = 14.0125(4), c = 17.4550(4) Å, α = 99.361(2), β = 98.071(2), γ = 101.650(2)°, V = 2932.92(13) Å^3, Z = 2, ρ_c = 1.469 g cm^{-3}, μ = 1.695 mm^{-1}. F_{000} = 1322, MoKα radiation, λ = 0.71073 Å, T = 100(2) K, $2\theta_{max}$ = 64.6°, 34956 reflections collected, 18977 unique (R_{int} = 0.0376). Final $GooF$ = 1.001, $R1$ = 0.0398, $wR2$ = 0.0868, R indices based on 16563 reflections with $I > 2\sigma(I)$ (refinement on F^2), $|\Delta\rho|_{max}$= 1.9(1) e Å^{-3}, 767 parameters, 8 restraints. Lp and absorption corrections applied.

8.5.2. Structures by Dr Stephen Moggach and Prof. Mark Ogden

Data was collected at 100(2) K on an Oxford Diffraction Xcalibur, Ruby, or Gemini ultra-diffractometer fitted using Mo Kα or Cu Kα radiation.Structures were solved with the XT structure solution program using the Intrinsic Phasing solution method and by using Olex2 as the graphical interface. The model was refined with version 2018/13 of ShelXL using Least Squares minimisation. Data reduction, scaling and absorption corrections were performed using CrysAlisPro (Rigaku, V1.171.40.53). All non-hydrogen atoms were refined anisotropically. Hydrogen and deutetrium atom positions were calculated geometrically and refined using the riding model. Details on selected individual crystal structure determinations and refinements are given below. All structures were refined by Dr Stephen Moggach and Prof. Mark Ogden.

[Dy(tbm)$_3$(DMSO)(H$_2$O)]·(EtOH)

$C_{35}H_{29.5}Dy_{0.5}O_6S_{0.5}$, M_r = 643.36, triclinic, P-1 (No. 2), a = 12.6634(3) Å, b = 14.0667(3) Å, c = 17.4776(4) Å, α = 99.467(2) °, β = 98.170(2) °, γ = 101.749(2)°, V = 2956.46(12) Å^3, T = 94.4(7) K, Z = 2, Z' = 0, μ(MoK$_\alpha$) = 1.364, 57424

reflections measured, 19813 unique (R_{int} = 0.0498) which were used in all calculations. The final wR_2 was 0.0767 (all data) and R_1 was 0.0394 (I > 2(I)).

[Er(tbm)$_3$(DMSO)(EtOH)]

$C_{70}H_{57}ErO_{11}S$, M_r = 1216.52, triclinic, *P*-1 (No. 2), a = 11.1193(2) Å, b = 11.9004(3) Å, c = 24.5613(4) Å, α = 77.031(2)°, β = 79.6900(10)°, γ = 65.523(2)°, V = 2868.93(11) Å^3, T = 94.9(8) K, Z = 2, Z' = 0, μ(MoK$_\alpha$) = 1.561, 183610 reflections measured, 19920 unique (R_{int} = 0.0408) which were used in all calculations. The final wR_2 was 0.0728 (all data) and R_1 was 0.0305 (I > 2(I)).

[Eu$_2$(Bdbm)$_3$(phen)$_2$]

$C_{96}H_{64}N_4O_{12}Eu_2$, monoclinic, C 2/c (No. 15), a = 31.0368(9) Å, b = 19.7158(5) Å, c = 16.8254(4) Å, α = 90°, β = 100.663(3)°, γ = 90°, V = 10117.9(4) Å^3, Z = 4, Z' = 0, R_1 was 0.0762 (I > 2(I)).

[Eu(dnm)$_3$(DMSO)$_2$]

$C_{73}H_{57}EuO_8S_2$, M_r = 1278.26, triclinic, *P*-1 (No. 2), a = 9.2838(2) Å, b = 17.3262(4) Å, c = 20.0193(4) Å, α = 105.813(2)°, β = 90.268(2)°, γ = 93.125(2)°, V = 3093.05(12) Å^3, T = 95.3(3) K, Z = 2, Z' = 1, μ(MoK$_\alpha$) = 1.138, 99335 reflections measured, 21460 unique (R_{int} = 0.0606) which were used in all calculations. The final wR_2 was 0.1445 (all data) and R_1 was 0.0574 (I > 2(I)).

[Eu(tbm)$_3$(DMSO)(H$_2$O)]·(EtOH)

$C_{70}H_{59}EuO_{12}S$, M_r = 1276.19, triclinic, *P*-1 (No. 2), a = 12.7607(2) Å, b = 14.3047(2) Å, c = 17.3038(2) Å, α = 100.4160(10)°, β = 100.1850(10)°, γ = 103.1210(10)°, V = 2946.14(7) Å^3, T = 100.00(14) K, Z = 2, Z' = 1, μ(MoK$_\alpha$) = 1.165, 92238 reflections measured, 13513 unique (R_{int} = 0.0430) which were used in all calculations. The final wR_2 was 0.0725 (all data) and R_1 was 0.0307 (I > 2(I)).

[Eu(tbm)$_3$(*d*.phen)]

$C_{78}H_{45}D_8EuN_2O_9$, M_r = 1322.23, triclinic, *P*-1 (No. 2), a = 10.6028(3) Å, b = 13.5680(3) Å, c = 21.3502(5) Å, α = 93.066(2)°, β = 102.257(2)°, γ = 95.455(2)°, V = 2979.23(13) Å^3, T = 96.8(5) K, Z = 2, Z' = 1, μ(CuK$_\alpha$) = 8.064, 81842 reflections measured, 10611 unique (R_{int} = 0.1185) which were used in all calculations. The final wR_2 was 0.0901 (all data) and R_1 was 0.0396 (I > 2(I)).

[Gd(dnm)$_3$(DMSO)$_2$]

$C_{73}H_{57}GdO_8S_2$, M_r = 1282.54, triclinic, *P*-1 (No. 2), a = 9.2658(2) Å, b = 17.3496(4) Å, c = 20.1961(5) Å, α = 74.405(2)°, β = 89.817(2)°, γ = 86.726(2)°, V = 3121.81(13) Å^3, T = 120.05(10) K, Z = 2, Z' = 0, μ(MoK$_\alpha$) = 1.185, 60102 reflections measured, 13851 unique (R_{int} = 0.0626) which were used in all calculations. The final wR_2 was 0.1231 (all data) and R_1 was 0.0526 (I > 2(I)).

[La(tbm)$_3$(DMSO)$_2$]

$C_{70}H_{57}IO_{11}S_2$, M_r = 1265.17, triclinic, *P*-1 (No. 2), a = 11.3798(3) Å, b = 12.2112(4) Å, c = 24.2359(5) Å, α = 91.001(2)°, β = 103.102(2)°, γ = 114.331(2)°, V = 2965.41(15) Å^3, T = 293(2) K, Z = 2, Z' = 1, μ(CuK$_\alpha$) = 5.417, 63337 reflections measured, 10558 unique (R_{int} = 0.0923) which were used in all calculations. The final wR_2 was 0.1098 (all data) and R_1 was 0.0433 (I > 2(I)).

[La(tbm)$_3$(DMSO)(EtOH)]

$C_{70}H_{56}LaO_{11}S$, M_r = 1222.09, triclinic, *P*-1 (No. 2), a = 11.5027(3) Å, b = 12.0598(3) Å, c = 23.7789(5) Å, α = 92.274(2)°, β = 102.613(2)°, γ = 114.265(2)°, V = 2903.41(13) Å^3, T = 94.8(6) K, Z = 2, Z' = 0, μ(MoK$_\alpha$) = 6.857, 63340 reflections measured, 10353 unique (R_{int} = 0.0980) which were used in all calculations. The final wR_2 was 0.1304 (all data) and R_1 was 0.0498 (I > 2(I)).

[Lu(tbm)$_3$(DMSO)(EtOH)]

$C_{138}H_{107}Lu_2O_{22}S_2$, M_r = 1281.18, triclinic, *P*-1 (No. 2), a = 11.0653(4) Å, b = 11.9124(5) Å, c = 24.5190(7) Å, α = 77.057(3) °, β = 79.567(3) °, γ = 65.552(4) °, V = 2853.2(2) Å^3, T = 293(2) K, Z = 1, Z' = 0, μ(MoK$_\alpha$) = 0.916, 32921 reflections measured, 18823 unique (R_{int} = 0.0465) which were used in all calculations. The final wR_2 was 0.1193 (all data) and R_1 was 0.0520 (I > 2(I)).

[Nd(dnm)$_3$(DMSO)$_2$]

$C_{73}H_{57}NdO_8S_2$, M_r = 1270.54, triclinic, *P*-1 (No. 2), a = 9.2982(4) Å, b = 17.3375(8) Å, c = 20.1508(9) Å, α = 73.933(4)°, β = 89.878(3)°, γ = 86.495(4)°, V = 3115.4(2) Å^3, T = 120.05(10) K, Z = 2, Z' = 0, μ(MoK$_\alpha$) = 0.956, 42596 reflections measured, 10593 unique (R_{int} = 0.0986) which were used in all calculations. The final wR_2 was 0.1872 (all data) and R_1 was 0.0718 (I > 2(I)).

[Pr(tbm)$_3$(DMSO)(EtOH)]

$C_{70}H_{57}O_{11}PrS$, M_r = 1247.12, triclinic, P-1 (No. 2), a = 11.5055(3) Å, b = 12.0126(3) Å, c = 23.7766(5) Å, α = 92.182(2)°, β = 102.656(2)°, γ = 114.392(2)°, V = 2889.43(13) Å^3, T = 99.95(10) K, Z = 2, Z' = 1, μ(MoK$_\alpha$) = 0.943, 65354 reflections measured, 19755 unique (R_{int} = 0.0597) which were used in all calculations. The final wR_2 was 0.1199 (all data) and R_1 was 0.0512 (I > 2(I)).

[Tb(tbm)$_3$(DMSO)(H$_2$O)]·(EtOH)

$C_{34}H_{26.5}O_{5.5}S_{0.5}Tb_{0.5}$, M_r = 829.89, triclinic, P-1 (No. 2), a = 12.70300(10) Å, b = 14.0514(2) Å, c = 17.3571(2) Å, α = 100.0510(10)°, β = 99.2760(10)°, γ = 102.2370(10)°, V = 2917.38(6) Å^3, T = 94.5(6) K, Z = 2, Z' = 1, μ(MoK$_\alpha$) = 2.629, 226254 reflections measured, 20461 unique (R_{int} = 0.0597) which were used in all calculations. The final wR_2 was 0.0972 (all data) and R_1 was 0.0402 (I > 2(I)).

[Yb$_2$(Bdbm)$_3$(phen)$_2$]

$C_{96}H_{64}N_4O_{12}Yb_2$, M_r = 1811.59, monoclinic, $C2/c$ (No. 15), a = 31.3173(3) Å, b = 19.6080(3) Å, c = 17.0174(2) Å, β = 100.1060(10)°, α = γ = 90°, V = 10287.7(2) Å^3, T = 150.00(10) K, Z = 4, Z' = 0.5, μ(CuK$_\alpha$) = 3.694, 94687 reflections measured, 10423 unique (R_{int} = 0.0634) which were used in all calculations. The final wR_2 was 0.1843 (all data) and R_1 was 0.0522 (I > 2(I)).

[Yb(tbm)$_3$(*d*.phen)]

$C_{78}H_{45}D_8N_2O_9Yb$, M_r = 1343.31, triclinic, P-1 (No. 2), a = 10.6344(7) Å, b = 13.4027(8) Å, c = 21.3362(11) Å, α = 93.100(4)°, β = 102.200(5)°, γ = 96.211(5)°, V = 2945.6(3) Å^3, T = 96.9(5) K, Z = 2, Z' = 1, μ(CuK$_\alpha$) = 3.472, 51957 reflections measured, 10491 unique (R_{int} = 0.1226) which were used in all calculations. The final wR_2 was 0.1199 (all data) and R_1 was 0.0488 (I > 2(I)).

[Y(tbm)$_3$(DMSO)(H$_2$O)]·(EtOH)

$C_{35}H_{30}O_6S_{0.5}Y_{0.5}$, M_r = 607.07, triclinic, P-1 (No. 2), a = 12.6505(6) Å, b = 14.0259(5) Å, c = 17.4558(8) Å, α = 99.445(4)°, β = 98.067(4)°, γ = 101.589(4)°, V = 2944.5(2) Å^3, T = 94.6(7) K, Z = 2, Z' = 0, μ(MoK$_\alpha$) = 1.091, 34847 reflections measured, 19361 unique (R_{int} = 0.0445) which were used in all calculations. The final wR_2 was 0.1288 (all data) and R_1 was 0.0565 (I > 2(I)).

[Y(tbm)$_3$(phen)]

$C_{78}H_{53}N_2O_9Y$, M_r = 1251.13, triclinic, P-1 (No. 2), a = 10.6092(3) Å, b = 13.4763(4) Å, c = 21.3617(6) Å, α = 93.134(2)°, β = 102.193(2)°, γ = 95.996(2)°, V = 2959.65(15) Å^3, T = 99.3(2) K, Z = 2, Z' = 1, μ(MoK$_\alpha$) = 1.052, 95246 reflections measured, 20535 unique (R_{int} = 0.0528) which were used in all calculations. The final wR_2 was 0.1003 (all data) and R_1 was 0.0465 (I > 2(I)).

9.0. References

1. Bunzli, J.-C. G.; Eliseeva, S. V., Intriguing aspects of lanthanide luminescence. *Chem. Sci.* **2013,** *4* (5), 1939-1949.
2. Bunzli, J.-C. G.; Piguet, C., Taking advantage of luminescent lanthanide ions. *Chem. Soc. Rev.* **2005,** *34* (12), 1048-1077.
3. Bünzli, J.-C. G.; Eliseeva, S. V., Basics of Lanthanide Photophysics. In *Lanthanide Luminescence: Photophysical, Analytical and Biological Aspects*, Hänninen, P.; Härmä, H., Eds. Springer: Berlin, Heidelberg, 2010; pp 1-45.
4. Abad Galán, L. Exploring the Chemistry of Lanthanoid β–Triketonate Complexes. Curtin University, Curtin University, 2018.
5. Reid, B. L. Structural and Photophysical Investigation of Lanthanoid β-Triketonates. Curtin University, Curtin University, 2015.
6. MacDonald, M. R.; Bates, J. E.; Ziller, J. W.; Furche, F.; Evans, W. J., Completing the Series of +2 Ions for the Lanthanide Elements: Synthesis of Molecular Complexes of Pr2+, Gd2+, Tb2+, and Lu2+. *J. Am. Chem. Soc.* **2013,** *135* (26), 9857-9868.
7. Pyykkö, P.; Orama, O., *What did Johan Gadolin Actually do?* Springer: 1996.
8. Forsyth, M.; Hinton, B., *Rare Earth-Based Corrosion Inhibitors*. Elsevier: 2014; p 338.
9. Bünzli, J.-C. G., On the design of highly luminescent lanthanide complexes. *Coord. Chem. Rev.* **2015,** *293-294*, 19-47.
10. Eliseeva, S. V.; Bunzli, J.-C. G., Rare earths: jewels for functional materials of the future. *New J. Chem.* **2011,** *35* (6), 1165-1176.
11. Andres, J.; Hersch, R. D.; Moser, J. E.; Chauvin, A. S., A New Anti-Counterfeiting Feature Relying on Invisible Luminescent Full Color Images Printed with Lanthanide-Based Inks. *Adv Funct Mater.* **2014,** *24* (32), 5029-5036.
12. Reid, B. L.; Stagni, S.; Malicka, J. M.; Cocchi, M.; Hanan, G. S.; Ogden, M. I.; Massi, M., Lanthanoid β-triketonates: a new class of highly efficient NIR emitters for bright NIR-OLEDs. *Chem. Commun.* **2014,** *50* (78), 11580-11582.
13. Bünzli, J.-C. G.; Eliseeva, S. V., Lanthanide NIR luminescence for telecommunications, bioanalyses and solar energy conversion. *J. Rare Earth* **2010,** *28* (6), 824-842.
14. Bunzli, J.-C. G., Europium in the Limelight. *Nat. Chem.* **2010,** *2* (8), 696.
15. Bünzli, J.-C. G., Lanthanide Luminescence for Biomedical Analyses and Imaging. *Chem. Rev.* **2010,** *110* (5), 2729-2755.
16. Long, J. R., Implications in organic synthesis. In *Handbook on the Physics and Chemistry of Rare Earths*, Gschneider, K. A.; Eyring, J.; Eyring, L., Eds. Elsevier: 1986; Vol. 8, pp 335-373.
17. Bünzli, J.-C. G., Rising Stars in Science and Technology: Luminescent Lanthanide Materials. *Eur. J. Inorg. Chem.* **2017,** *2017* (44), 5058-5063.
18. Liu, J.-L.; Chen, Y.-C.; Tong, M.-L., Symmetry strategies for high performance lanthanide-based single-molecule magnets. *Chem. Soc. Rev.* **2018,** *47* (7), 2431-2453.

19. Cotton, S., *Lanthanide and Actinide Chemistry*. John Wiley & Sons Ltd.: 2006; p 263.
20. Siekierski, S., The itinerant character of 4f orbitals in lanthanide metals by a comparison of lanthanide contraction in metals and ionic compounds. *Inorganica Chim. Acta* **1985,** *109* (3), 199-201.
21. Cotton, S. A.; Harrowfield, J. M., Solvento Complexes of the Lanthanide Ions. *Encyclopedia of Inorganic and Bioinorganic Chemistry* **2012**.
22. Ruiz-Martínez, A.; Casanova, D.; Alvarez, S., Polyhedral Structures with an Odd Number of Vertices: Nine-Coordinate Metal Compounds. *Chem. Eur. J.* **2008,** *14* (4), 1291-1303.
23. Casanova, D.; Llunell, M.; Alemany, P.; Alvarez, S., The Rich Stereochemistry of Eight-Vertex Polyhedra: A Continuous Shape Measures Study. *Chem. Eur. J.* **2005,** *11* (5), 1479-1494.
24. Bersuker, I. B., *Electronic Structure and Properties of Transition Metal Compounds: Introduction to the Theory*. Wiley: 2010.
25. Bünzli, J.-C. G., Review: Lanthanide coordination chemistry: from old concepts to coordination polymers. *J. Coord. Chem.* **2014,** *67* (23-24), 3706-3733.
26. Casanova, D.; Cirera, J.; Llunell, M.; Alemany, P.; Avnir, D.; Alvarez, S., Minimal Distortion Pathways in Polyhedral Rearrangements. *J. Am. Chem. Soc.* **2004,** *126* (6), 1755-1763.
27. Weber, M. J., Rare earth lasers. In *Handbook on the Physics and Chemistry of Rare Earths*, Gschneider, K. A.; Eyring, J.; Eyring, L., Eds. Elsevier: 1979; Vol. 4, pp 275-315.
28. Eliseeva, S. V.; Bünzli, J.-C. G., Lanthanide luminescence for functional materials and bio-sciences. *Chem. Soc. Rev.* **2010,** *39* (1), 189-227.
29. Hasegawa, Y.; Kitagawa, Y.; Nakanishi, T., Effective photosensitized, electrosensitized, and mechanosensitized luminescence of lanthanide complexes. *NPG Asia Mater.* **2018,** *10* (4), 52-70.
30. Weissman, S. I., Intramolecular Energy Transfer The Fluorescence of Complexes of Europium. *J. Chem. Phys.* **1942,** *10* (4), 214-217.
31. Lehn, J. M., Perspectives in Supramolecular Chemistry - From Molecular Recognition towards Molecular Information Processing and Self-Organization. *Angew. Chem, Int. Ed. Engl.* **1990,** *29* (11), 1304-1319.
32. Sabbatini, N.; Guardigli, M.; Lehn, J.-M., Luminescent lanthanide complexes as photochemical supramolecular devices. *Coord. Chem. Rev.* **1993,** *123* (1), 201-228.
33. Kleinerman, M., Energy Migration in Lanthanide Chelates. *J. Chem. Phys.* **1969,** *51* (6), 2370-2381.
34. Steemers, F. J.; Verboom, W.; Reinhoudt, D. N.; van der Tol, E. B.; Verhoeven, J. W., New Sensitizer-Modified Calix[4]arenes Enabling Near-UV Excitation of Complexed Luminescent Lanthanide Ions. *J. Am. Chem. Soc.* **1995,** *117* (37), 9408-9414.
35. Abad Galán, L.; Sobolev, A.; Skelton, B.; Zysman-Colman, E.; Ogden, M. I.; Massi, M., Bright near Infrared Neodymium Emission from Europium Sensitisation in β-Triketonate Coordination Polymers. *ChemRxiv* **2018**.

36. Doffek, C.; Alzakhem, N.; Bischof, C.; Wahsner, J.; Güden-Silber, T.; Lügger, J.; Platas-Iglesias, C.; Seitz, M., Understanding the Quenching Effects of Aromatic C–H- and C–D-Oscillators in Near-IR Lanthanoid Luminescence. *J. Am. Chem. Soc.* **2012,** *134* (39), 16413-16423.
37. Tan, R. H. C.; Motevalli, M.; Abrahams, I.; Wyatt, P. B.; Gillin, W. P., Quenching of IR Luminescence of Erbium, Neodymium, and Ytterbium β-Diketonate Complexes by Ligand C−H and C−D Bonds. *J. Phys. Chem.* **2006,** *110* (48), 24476-24479.
38. Bassett, A. P.; Van Deun, R.; Nockemann, P.; Glover, P. B.; Kariuki, B. M.; Van Hecke, K.; Van Meervelt, L.; Pikramenou, Z., Long-Lived Near-Infrared Luminescent Lanthanide Complexes of Imidodiphosphinate "Shell" Ligands. *Inorg. Chem.* **2005,** *44* (18), 6140-6142.
39. Glover, P. B.; Bassett, A. P.; Nockemann, P.; Kariuki, B. M.; Van Deun, R.; Pikramenou, Z., Fully Fluorinated Imidodiphosphinate Shells for Visible- and NIR- Emitting Lanthanides: Hitherto Unexpected Effects of Sensitizer Fluorination on Lanthanide Emission Properties. *Chem. Eur. J.* **2007,** *13* (22), 6308-6320.
40. Kim, J.-H.; Park, Y.-P., Luminescence Properties of Yb(HFA-D)3 Complexes in Organic Solvents. *J. Korean Phys. Soc.* **2003,** *43* (2), 277.
41. Shimanouchi, T., Tables of molecular vibrational frequencies. Consolidated volume II. *J. Phys. Chem. Ref. Data* **1977,** *6* (3), 993-1102.
42. Sato, S.; Wada, M., Relations between Intramolecular Energy Transfer Efficiencies and Triplet State Energies in Rare Earth β-diketone Chelates. *Bull. Chem. Soc. Jpn.* **1970,** *43* (7), 1955-1962.
43. Binnemans, K., Rare-Earth Beta-Diketonates. In *Handbook on the Physics and Chemistry of Rare Earths*, Gschneider, K. A.; Bunzli, J.-G.; Pecharsky, V. K., Eds. Elsevier: 2005; Vol. 35.
44. Sato, N.; Shinkai, S., Energy-transfer luminescence of lanthanide ions encapsulated in sensitizer-modified calix[4]arenes. *J. Chem. Soc.* **1993,** (4), 621-624.
45. D'Alessio, D.; Muzzioli, S.; Skelton, B. W.; Stagni, S.; Massi, M.; Ogden, M. I., Luminescent lanthanoid complexes of a tetrazole-functionalised calix[4]arene. *Dalton Trans.* **2012,** *41* (16), 4736-4739.
46. Alpha, B.; Lehn, J. M.; Mathis, G., Energy Transfer Luminescence of Europium(III) and Terbium(III) Cryptates of Macrobicyclic Polypyridine Ligands. *Angew. Chem, Int. Ed. Engl.* **1987,** *26* (3), 266-267.
47. Blasse, G.; Dirksen, G. J.; Sabbatini, N.; Perathoner, S.; Lehn, J. M.; Alpha, B., Luminescence processes in [Tb.cntnd.bpy.bpy.bpy]3+ cryptate: a low-temperature solid-state study. *J. Phys. Chem.* **1988,** *92* (9), 2419-2422.
48. Hilder, M.; Junk, P. C.; Kynast, U. H.; Lezhnina, M. M., Spectroscopic properties of lanthanoid benzene carboxylates in the solid state: Part 1. *J. Photoch. Photobio. A* **2009,** *202* (1), 10-20.
49. Hilder, M.; Lezhnina, M.; Cole, M. L.; Forsyth, C. M.; Junk, P. C.; Kynast, U. H., Spectroscopic properties of lanthanoid benzene carboxylates in the solid state: Part 2. Polar substituted benzoates. *J. Photoch. Photobio. A* **2011,** *217* (1), 76-86.

50. Latva, M.; Takalo, H.; Mukkala, V.-M.; Matachescu, C.; Rodríguez-Ubis, J. C.; Kankare, J., Correlation between the lowest triplet state energy level of the ligand and lanthanide(III) luminescence quantum yield. *J. Lumin.* **1997,** *75* (2), 149-169.
51. Lemmetyinen, H.; Vuorimaa, E.; Jutila, A.; Mukkala, V. M.; Takalo, H.; Kankare, J., A time-resolved study of the mechanism of the energy transfer from a ligand to the lanthanide(III) ion in solutions and solid films. *J. Lumin.* **2000,** *15* (6), 341-350.
52. Hemmilä, I.; Mukkala, V. M.; Latva, M.; Kiilholma, P., Di- and tetracarboxylate derivatives of pyridines, bipyridines and terpyridines as luminogenic reagents for time-resolved fluorometric determination of terbium and dysprosium. *J. Biochem. Biophys. Methods* **1993,** *26* (4), 283-290.
53. Mukkala, V. M.; Kankare Jouko, J., New 2,2'-Bipyridine Derivatives and Their Luminescence Properties with Europium(III) and Terbium(III) Ions. *Helv. Chim. Acta* **1992,** *75* (5), 1578-1592.
54. Reuben, J.; Elgavish, G. A., Chapter 38 Shift reagents and NMR of paramagnetic lanthanide complexes. In *Handbook on the Physics and Chemistry of Rare Earths*, Gschneider, K. A.; Eyring, J.; Eyring, L., Eds. Elsevier: 1979; Vol. 4, pp 483-514.
55. Kido, J.; Hayase, H.; Hongawa, K.; Nagai, K.; Okuyama, K., Bright red light-emitting organic electroluminescent devices having a europium complex as an emitter. *Appl. Phys. Lett.* **1994,** *65* (17), 2124-2126.
56. Kido, J.; Ikeda, W.; Kimura, M.; Nagai, K., White-Light-Emitting Organic Electroluminescent Device Using Lanthanide Complexes. *Jpn. J. Appl. Phys.* **1996,** *35* (3B), L394.
57. Lunstroot, K.; Nockemann, P.; Van Hecke, K.; Van Meervelt, L.; Görller-Walrand, C.; Binnemans, K.; Driesen, K., Visible and Near-Infrared Emission by Samarium(III)-Containing Ionic Liquid Mixtures. *Inorg. Chem.* **2009,** *48* (7), 3018-3026.
58. Akerboom, S.; Meijer, M. S.; Siegler, M. A.; Fu, W. T.; Bouwman, E., Structure, photo- and triboluminescence of the lanthanoid dibenzoylmethanates: HNEt3 Ln(dbm)4. *J. Lumin.* **2013,** *145*, 278 - 282.
59. Wagner Anna, T.; Roesky Peter, W., Rare-Earth Metal Oxo/Hydroxo Clusters - Synthesis, Structures, and Applications. *Eur. J. Inorg. Chem.* **2016,** *2016* (6), 782-791.
60. Andrews, P. C.; Beck, T.; Fraser, B. H.; Junk, P. C.; Massi, M.; Moubaraki, B.; Murray, K. S.; Silberstein, M., Functionalised β-diketonate polynuclear lanthanoid hydroxo clusters: Synthesis, characterisation, and magnetic properties. *Polyhedron* **2009,** *28* (11), 2123-2130.
61. Andrews, P. C.; Gee, W. J.; Junk, P. C.; Massi, M., Variation of structural motifs in lanthanoid hydroxo clusters by ligand modification. *New J. Chem.* **2013,** *37* (1), 35-48.
62. Ismail, M.; Lyle, S. J.; Newbery, J. E., Some lanthanide and group II complexes with triketones. *J. Inorg. Nucl. Chem.* **1969,** *31* (7), 2091-2093.
63. Crosby, G. A.; Whan, R. E., Extreme Variations of the Emission Spectra of Dysprosium Chelates. *J. Chem. Phys.* **1960,** *32* (2), 614-615.

64. Crosby, G. A.; Whan, R. E.; Alire, R. M., Intramolecular Energy Transfer in Rare Earth Chelates. Role of the Triplet State. *J. Chem. Phys.* **1961,** *34* (3), 743-748.
65. Reid, B. L.; Woodward, R. C.; Fuller, R. O.; Sobolev, A. N.; Skelton, B. W.; Ogden, M. I.; Massi, M., Investigation of the structure and magnetism in lanthanide β-triketonate tetranuclear assemblies. *J. Coord. Chem.* **2016,** *69* (11-13), 1852-1863.
66. Reid, B. L.; Stagni, S.; Malicka, J. M.; Cocchi, M.; Sobolev, A. N.; Skelton, B. W.; Moore, E. G.; Hanan, G. S.; Ogden, M. I.; Massi, M., Lanthanoid/Alkali Metal β - Triketonate Assemblies: A Robust Platform for Efficient NIR Emitters. *Chem. Eur. J.* **2015,** *21* (50), 18354-18363.
67. Abad Galán, L.; Reid, B. L.; Stagni, S.; Sobolev, A. N.; Skelton, B. W.; Moore, E. G.; Hanan, G.; Zysman-Colman, E.; Ogden, M. I.; Massi, M., Probing the effect of β-triketonates in visible and NIR emitting lanthanoid complexes. *Dalton Trans.* **2018**.
68. Abad Galán, L.; Reid, B. L.; Stagni, S.; Sobolev, A. N.; Skelton, B. W.; Cocchi, M.; Malicka, J. M.; Zysman-Colman, E.; Moore, E. G.; Ogden, M. I.; Massi, M., Visible and Near-Infrared Emission from Lanthanoid β-Triketonate Assemblies Incorporating Cesium Cations. *Inorg. Chem.* **2017,** *56* (15), 8975-8985.
69. Abad Galán, L.; Wada, S.; Cameron, L.; Sobolev, A. N.; Hasegawa, Y.; Zysman-Colman, E.; Ogden, M. I.; Massi, M., Photophysical investigation of near infrared emitting lanthanoid complexes incorporating tris(2-naphthoyl)methane as a new antenna ligand. *Dalton Trans.* **2019,** *48* (11), 3768-3776.
70. Seitz, M.; Oliver, A. G.; Raymond, K. N., The Lanthanide Contraction Revisited. *J. Am. Chem. Soc.* **2007,** *129* (36), 11153-11160.
71. Ishiguro, S.; Umebayashi, Y.; Komiya, M., Thermodynamic and structural aspects on the solvation steric effect of lanthanide(III)—dependence on the ionic size. *Coord. Chem. Rev.* **2002,** *226* (1), 103-111.
72. Habenschuss, A.; Spedding, F. H., The coordination (hydration) of rare earth ions in aqueous chloride solutions from x-ray diffraction. III. SmCl3, EuCl3, and series behavior. *J. Chem. Phys.* **1980,** *73* (1), 442-450.
73. Habenschuss, A.; Spedding, F. H., The coordination (hydration) of rare earth ions in aqueous chloride solutions from x ray diffraction. I.TbCl3,DyCl3, ErCl3,TmCl3,and LuCl3. *J. Chem. Phys.* **1979,** *70* (6), 2797-2806.
74. Habenschuss, A.; Spedding, F. H., The coordination (hydration) of rare earth ions in aqueous chloride solutions from x-ray diffraction. II. LaCl3, PrCl3, and NdCl3a). *J. Chem. Phys.* **1979,** *70* (8), 3758-3763.
75. Cotton, S. A., *Scandium, Yttrium & the Lanthanides: Inorganic & Coordination Chemistry*. **2006**.
76. Zabrodsky, H.; Peleg, S.; Avnir, D., Continuous symmetry measures. *J. Am. Chem. Soc.* **1992,** *114* (20), 7843-7851.
77. Binnemans, K., Interpretation of europium(III) spectra. *Coord. Chem. Rev.* **2015,** *295*, 1-45.
78. Lakowicz, J. R., *Principles of Fluorescence Spectroscopy*. 3 ed.; Springer US: 2006.

79. Hollerman, W. A.; Fontenot, R. S.; Bhat, K. N.; Aggarwal, M. D., Measuring the Process Variability in Triboluminescence Emission Yield for EuD4TEA. *Metall. Mater. Trans. A* **2012,** *43* (11), 4200-4203.

80. Sadikov, G. G.; Antsyshkina, A. S.; Rodnikova, M. N.; Solonina, I. A., Intracomplex π-π stacking interaction between adjacent phenanthroline molecules in complexes with rare-earth nitrates: Crystal and molecular structures of bis(1,10-Phenanthroline)trinitratoytterbium and bis(1,10-Phenanthroline)trinitratolanthanum. *Crystallography Reports* **2009,** *54* (1), 48-58.

81. Stanley, J. M.; Chan, C. K.; Yang, X.; Jones, R. A.; Holliday, B. J., Synthesis, X-ray crystal structure and photophysical properties of tris(dibenzoylmethanido)(1,10-phenanthroline)samarium(III). *Polyhedron* **2010,** *29* (12), 2511-2515.

82. Brito, H. F.; Malta, O. L.; Felinto, M. C. F. C.; Teotonio, E. E. S.; Menezes, J. F. S.; Silva, C. F. B.; Tomiyama, C. S.; Carvalho, C. A. A., Luminescence investigation of the Sm(III)-β-diketonates with sulfoxides, phosphine oxides and amides ligands. *J. Alloy. Comp.* **2002,** *344* (1), 293-297.

83. Zhuravlev, K.; Tsaryuk, V.; Kudryashova, V.; Pekareva, I.; Yakovlev, Y., Role of methylene spacer in the excitation energy transfer in europium 1- and 2- naphthylcarboxylates. *J. Lumin.* **2010,** *130*, 1489-1496.

84. Shih, H.-R.; Chang, Y.-S., Structure and Photoluminescence Properties of Sm(3+) Ion-Doped YInGe(2)O(7) Phosphor. *Materials* **2017,** *10* (7), 779.

85. Sager, W. F.; Filipescu, N.; Serafin, F. A., Substituent Effects on Intramolecular Energy Transfer. I. Absorption and Phosphorescence Spectra of Rare Earth β-Diketone Chelates. *J. Phys. Chem.* **1965,** *69* (4), 1092-1100.

86. Bassett, A. P.; Magennis, S. W.; Glover, P. B.; Lewis, D. J.; Spencer, N.; Parsons, S.; Williams, R. M.; De Cola, L.; Pikramenou, Z., Highly Luminescent, Triple- and Quadruple-Stranded, Dinuclear Eu, Nd, and Sm(III) Lanthanide Complexes Based on Bis-Diketonate Ligands. *J. Am. Chem. Soc.* **2004,** *126* (30), 9413-9424.

87. Crosby, G. A.; Demas, J. N., Measurement of photoluminescence quantum yields. Review. *J. Phys. Chem.* **1971,** *75* (8), 991-1024.

88. Peters, J. A.; Huskens, J.; Raber, D. J., Lanthanide induced shifts and relaxation rate enhancements. *Prog. Nucl. Mag. Res. Sp.* **1996,** *28* (3), 283-350.

89. Ahmed, Z.; Iftikhar, K., Synthesis, luminescence and NMR studies of lanthanide (III) complexes with hexafluoroacetylacetone and phenanthroline. Part II. *Inorganica Chim. Acta* **2012,** *392*, 165-176.

90. Yang, L.; Gong, Z.; Nie, D.; Lou, B.; Bian, Z.; Guan, M.; Huang, C.; Lee, H. J.; Baik, W. P., Promoting near-infrared emission of neodymium complexes by tuning the singlet and triplet energy levels of β-diketonates. *New J. Chem.* **2006,** *30* (5), 791-796.

91. Condon, E., A Theory of Intensity Distribution in Band Systems. *Phys. Rev.* **1926,** *28* (6), 1182-1201.

92. Tsvirko, M. P.; Meshkova, S. B.; Venchikov, V. Y.; Topilova, Z. M.; Bol'shoi, D. V., Determination of contributions of various molecular groups to nonradiative deactivation of electronic excitation energy in β-diketonate complexes of ytterbium(III). *Opt Spektrosk* **2001,** *90* (5), 669-673.
93. Parsons, S.; Flack, H. D.; Wagner, T., Use of intensity quotients and differences in absolute structure refinement. *Acta crystallogr. B* **2013,** *69* (Pt 3), 249-259.

10.0. Appendix

10.1. Publication Acknowledgements

Shown below is the statement of contribution with regards to the following paper: Abad Galán L., Wada S., Cameron L., Sobolev A. N., Hasegawa Y., Zysman-Colman E., Ogden M. I., Massi M.. *Dalton Trans.* **2019**. DOI: 10.1039/C8DT04749A

To whom it may concern,

I, Lee Cameron, contributed the synthesis and photophysical analysis of the complex [Sm(**tnm**)$_3$(DMSO)$_2$] to the publication entitled; *Photophysical investigation of near infrared emitting lanthanoid complexes incorporating tris(2-naphthoyl)methane as a new antenna ligand*. Abad Galan, L.; Wada, S.; Cameron, L.; Sobolev, A. N.; Hasegawa, Y.; Zysman-Colman, E.; Ogden, M. I.; Massi, M., *Dalton Trans.* **2019**.

I, as a Co-Author, endorse that this level of contribution by the candidate indicated above is appropriate.

Co-author 1: Laura Abad Galan

Co-author 2: Satoshi Wada

Co-author 3: Alexandre N. Sobolev

Co-author 4: Eli Zysman-Colman

Co-author 5: Mark Ogden

Co-author 6: Massimiliano Massi

10.2. NMR Spectra

Bis-tribenzoylmethane (**Btbm**H_2) Spectra

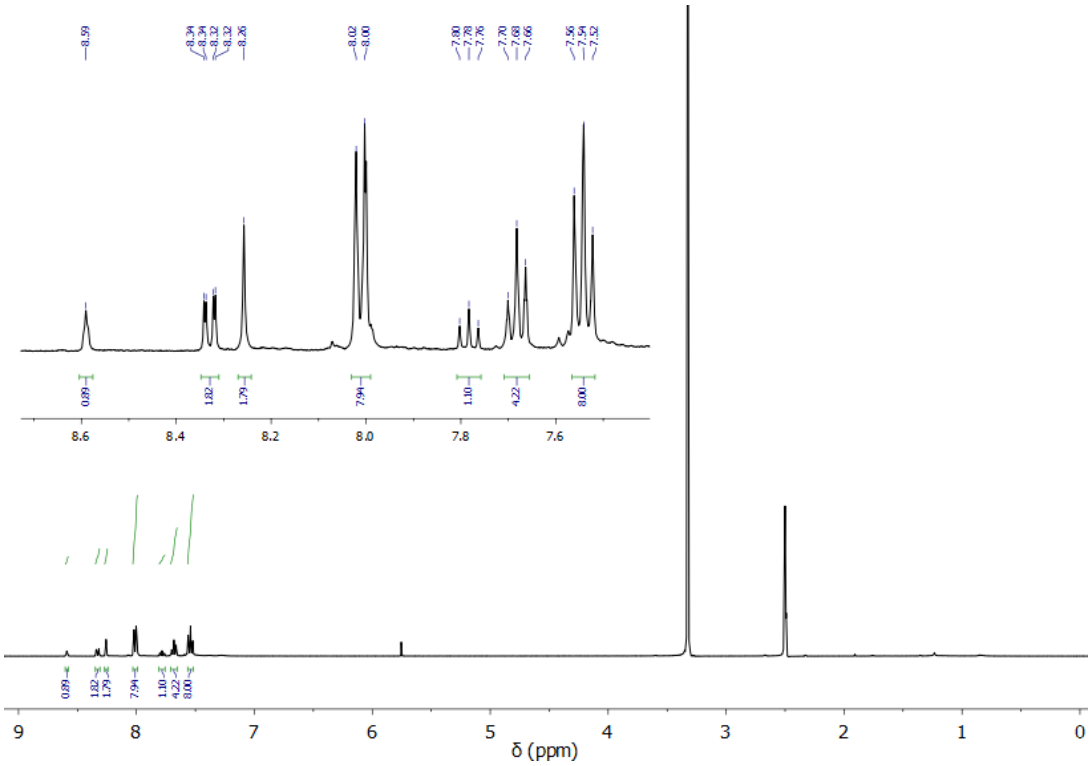

*Figure A1: ^{1}H NMR spectrum of **Btbm**H_2. Solvent = DMSO-d_6*

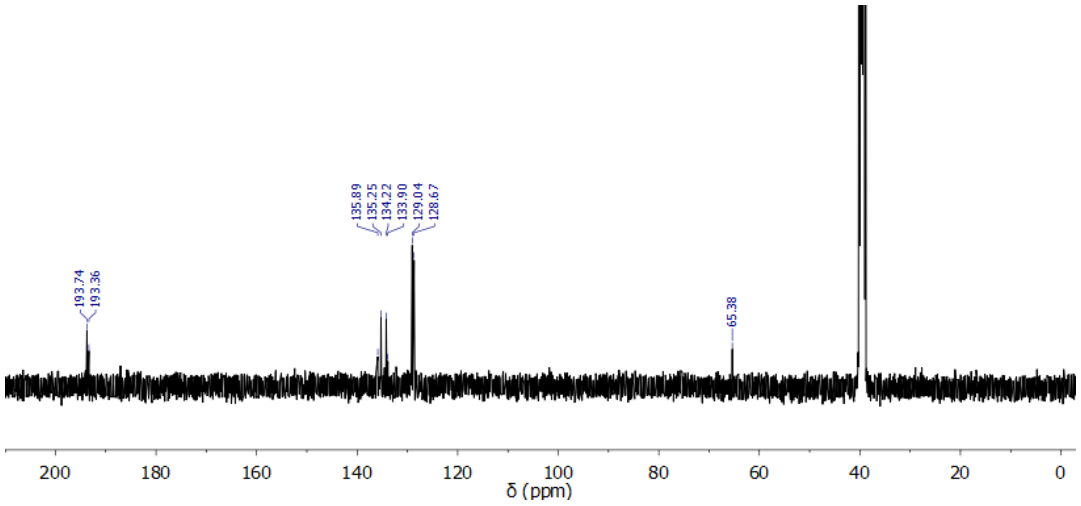

*Figure A2: ^{13}C NMR spectrum of **Btbm**H_2. Solvent = DMSO-d_6*

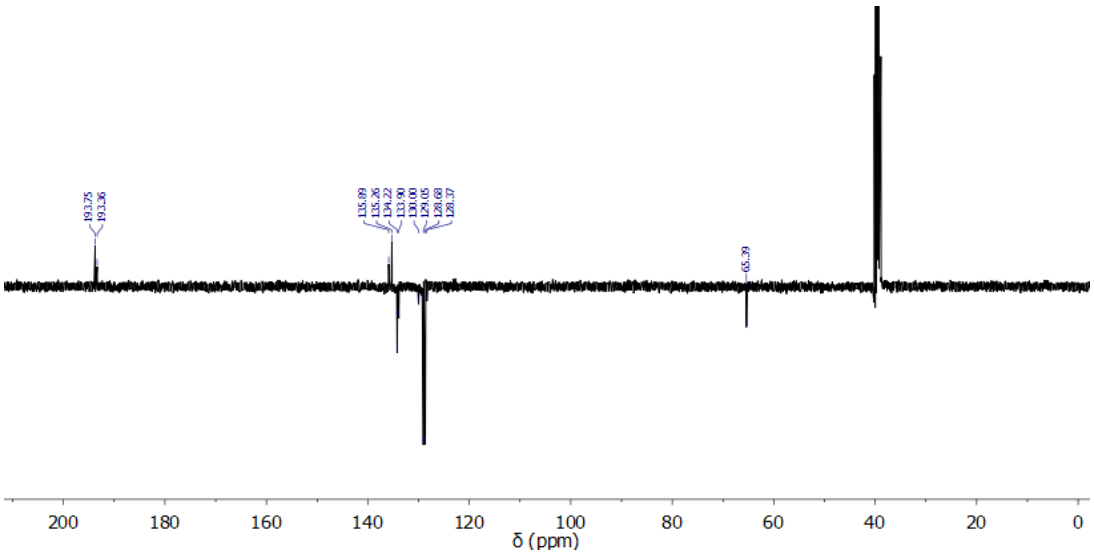

Figure A3: DEPTQ 135 spectrum of ***Btbm****H₂. Solvent = DMSO-d₆*

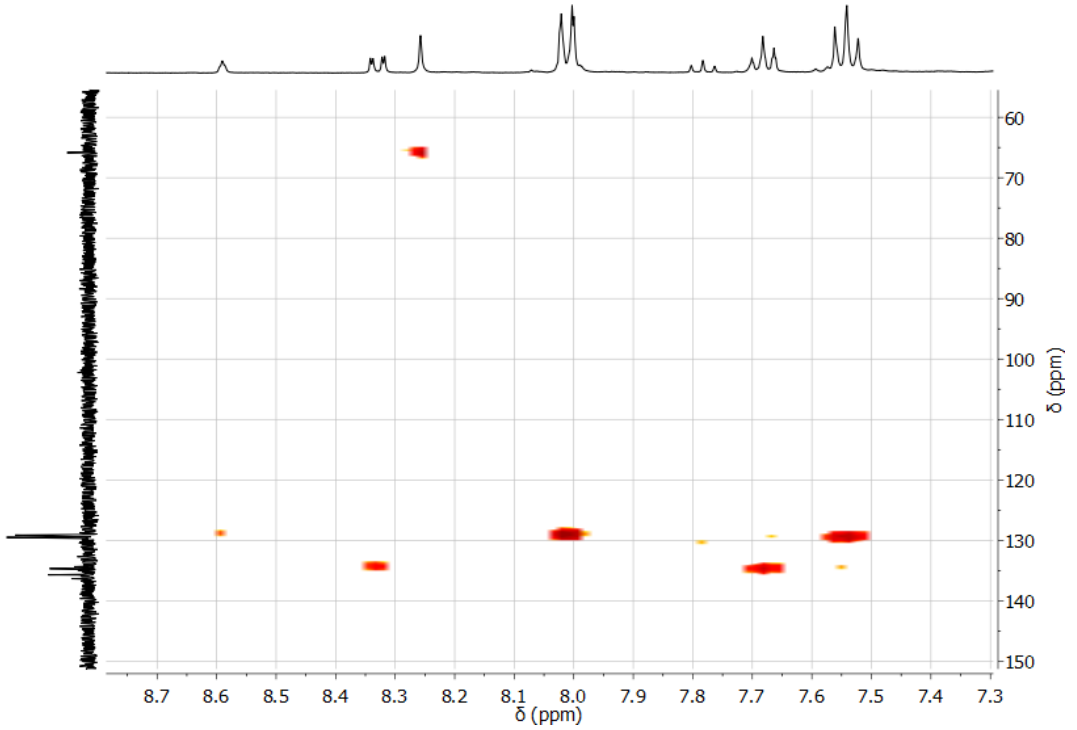

Figure A4: HSQC spectrum of ***Btbm****H₂. Solvent = DMSO-d₆*

10.3. UV-Vis Absorption Spectra

Chapter 2: DMSO Solvated Complexes

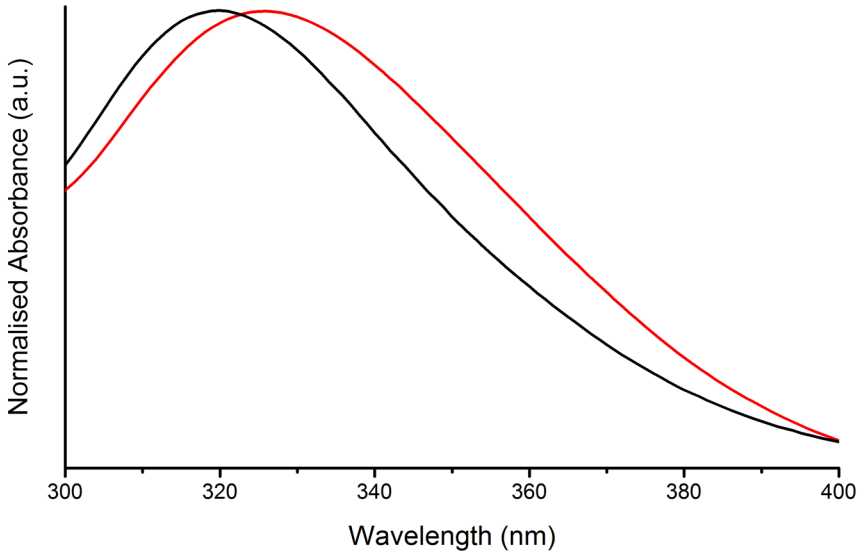

*Figure A5: Absorbance spectra of [Ln(**tbm**)$_3$(DMSO)(H$_2$O)]·(EtOH) for Eu^{3+} (red) and Yb^{3+} (black) in a MeCN solution (10^{-5} M).*

Chapter 3: 1,10-Phenanthroline Complexes

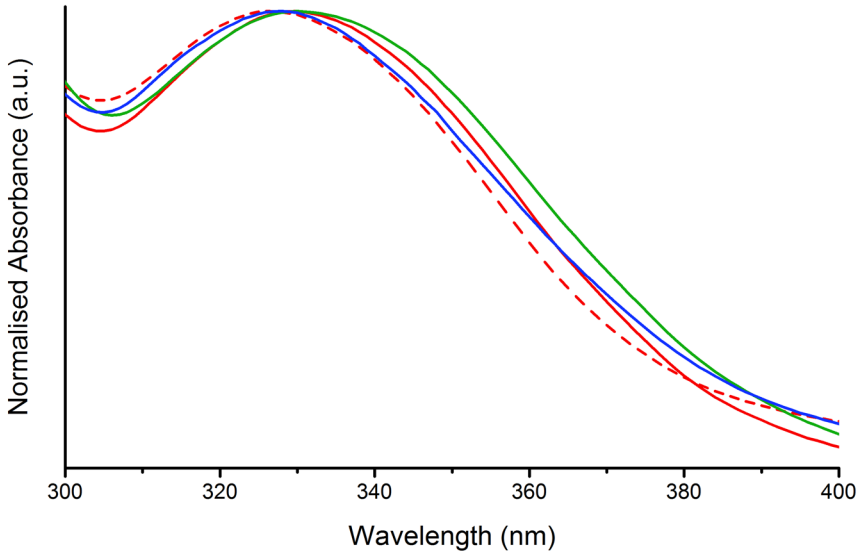

*Figure A6: Absorbance spectra of [Ln(**tbm**)$_3$(phen)] (dashed trace) and [Ln(**tbm**)$_3$(d-phen)] (solid trace) for Sm^{3+} (red), Eu^{3+} (green), and Yb^{3+} (blue) in a DCM solution (10^{-5} M).*

Chapter 4: Di/Tri-naphthoylmethane Complexes

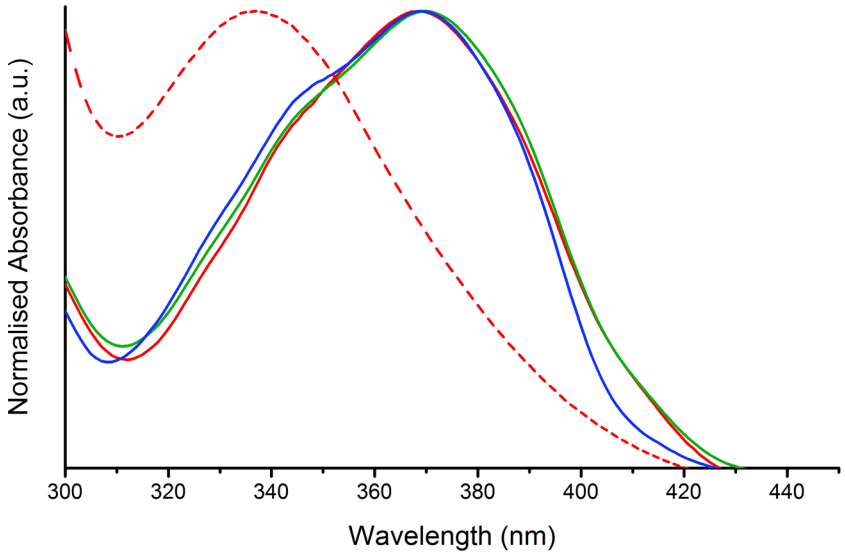

*Figure A7: Absorbance spectra of [Ln(**dnm**)$_3$(DMSO)$_2$] (solid trace) and [Ln(**tnm**)$_3$(DMSO)$_2$] (dashed trace) for Sm^{3+} (red), Eu^{3+} (green), and Yb^{3+} (blue) in a MeCN solution (10^{-5} M).*

Chapter 5: Bis-ketonate Ligands and Complexes

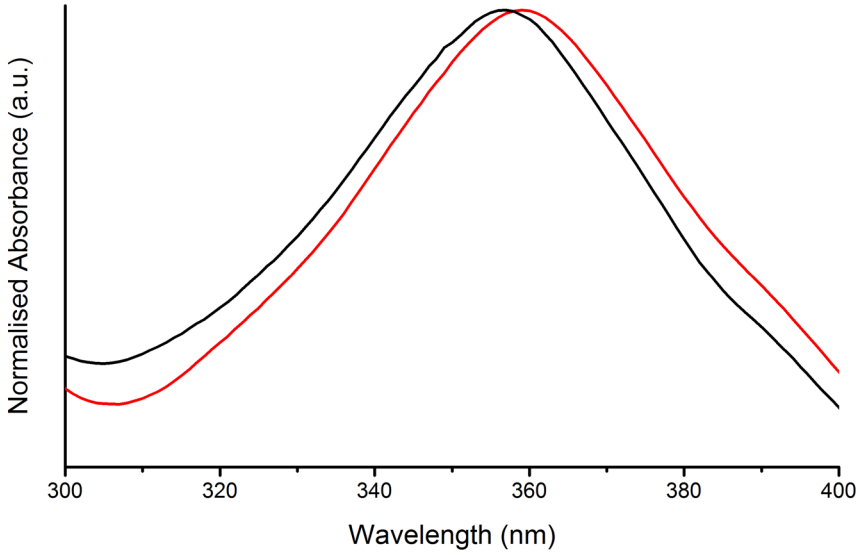

*Figure A8: Absorbance spectra of [Ln$_2$(**Bdbm**)$_3$(phen)$_2$] for Eu^{3+} (red) and Yb^{3+} (black) in a DCM solution (10^{-5} M).*

10.4. Structural Information

10.4.1. Complexes from Chapter 2.

*Table A1: Selected inter- and intra- molecular distances (Å) of the [Ln(**tbm**)$_3$(DMSO)$_2$] (Ln = La^{3+}, Sm^{3+}) complexes.*

La^{3+}		**Sm^{3+}**	
La1 – O0	2.498	Sm1 – O1	2.368
La1 – O004	2.448	Sm1 – O2	2.41
La1 – O006	2.53	Sm1 – O11	2.363
La1 – O007	2.436	Sm1 – O12	2.403
La1 – O008	2.47	Sm1 – O21	2.385
La1 – O00A	2.483	Sm1 – O22	2.397
La1 – O00C	2.518	Sm1 – O31	2.408
La1 – O00D	2.488	Sm1 – O32	2.382
La1 – La1	10.2222	Sm1 – Sm1	10.384

*Table A2: Selected inter- and intra- molecular distances (Å) of the [Ln(**tbm**)$_3$(DMSO)(EtOH)] (Ln = La^{3+}, Pr^{3+}, Er^{3+}, Lu^{3+}) complexes.*

	La^{3+}	**Er^{3+}**	**Lu^{3+}**	**Pr^{3+}**	
Ln1 – O1	2.475 (4)	2.349 (1)	2.297 (2)	Pr01 – O003	2.538 (3)
Ln1 – O2	2.459 (4)	2.325 (1)	2.324 (3)	Pr01 – O004	2.435 (2)
Ln1 – O3	2.488 (3)	2.344 (1)	2.255 (3)	Pr01 – O005	2.433 (3)
Ln1 – O4	2.461 (3)	2.347 (1)	2.294 (2)	Pr01 – O006	2.431 (2)
Ln1 – O5	2.524 (3)	2.287 (2)	2.323 (2)	Pr01 – O007	2.419 (3)
Ln1 – O6	2.454 (3)	2.31 (1)	2.318 (2)	Pr01 – O008	2.413 (2)
Ln1 – O7	2.577 (5)	2.291 (2)	2.346 (3)	Pr01 – O009	2.478 (2)
Ln1 – O8	2.471 (4)	2.377 (2)	2.259 (4)	Pr01 – O00A	2.424 (2)
Ln1 – Ln1	9.880 (6)	9.939 (6)	9.899 (7)	Pr01 – Pr01	9.888 (6)

*Table A3: Selected inter- and intra- molecular distances (Å) of the [Ln(**tbm**)$_3$(DMSO)(H$_2$O)]·(EtOH) ((Ln = Eu^{3+}, Tb^{3+}, Dy^{3+}, Yb^{3+}, Y^{3+}) complexes.*

	Tb^{3+}	**Dy^{3+}**	**Y^{3+}**
Ln1 – O1	2.337 (2)	2.345 (2)	2.323 (2)
Ln1 – O2	2.327 (2)	2.312 (2)	2.305 (2)
Ln1 – O3	2.356 (2)	2.318 (2)	2.339 (1)
Ln1 – O4	2.328 (2)	2.323 (1)	2.297 (2)
Ln1 – O5	2.317 (2)	2.337 (2)	2.341 (2)
Ln1 – O6	2.370 (2)	2.356 (2)	2.306 (1)
Ln1 – O7	2.434 (2)	2.316 (1)	2.412 (2)
Ln1 – O8	2.334 (2)	2.431 (2)	2.289 (1)
Ln1 – Ln1	8.624 (5)	8.643 (5)	8.621 (6)
	Eu^{3+}		**Yb^{3+}**
Eu1 – O003	2.363 (2)	Yb1 – O10	2.267 (2)
Eu1 – O004	2.397 (2)	Yb1 – O11	2.273 (2)
Eu1 – O005	2.383 (2)	Yb1 – O12	2.295 (2)
Eu1 – O006	2.348 (2)	Yb1 – O21	2.315 (2)
Eu1 – O007	2.351 (2)	Yb1 – O22	2.277 (2)
Eu1 – O008	2.34 (1)	Yb1 – O31	2.27 (2)
Eu1 – O009	2.372 (2)	Yb1 – O32	2.307 (2)
Eu1 – O00B	2.462 (2)	Yb1 – O1W	2.384 (2)
Eu1 – Eu1	8.717 (5)	Yb1 – Yb1	8.626 (5)

10.4.2. Complexes from Chapter 3

*Table A4: Selected inter- and intra- molecular distances (Å) of (HNEt$_3$)[Sm(**dbm**)$_4$]·(EtOH) and [Sm(**dbm**)$_3$(phen)]·(EtOH).*

(HNEt$_3$)[Sm(dbm)$_4$]·(EtOH)			
Sm1 – O11	2.398 (4)	Sm2 – O51	2.369 (3)
Sm1 – O12	2.420 (4)	Sm2 – O52	2.448 (3)
Sm1 – O21	2.444 (3)	Sm2 – O61	2.369 (4)
Sm1 – O22	2.376 (4)	Sm2 – O62	2.427 (3)
Sm1 – O31	2.401 (4)	Sm2 – O71	2.411 (4)
Sm1 – O32	2.364 (4)	Sm2 – O72	2.383 (3)
Sm1 – O41	2.402 (4)	Sm2 – O81	2.414 (3)
Sm1 – O42	2.389 (4)	Sm2 – O82	2.397 (3)
Sm1 – Sm1	23.699 (7)	Sm2 – Sm2	14.440 (7)
Sm1 – Sm2	13.006 (7)	Sm2 – Sm1	15.011 (7)
Sm1 – Sm2	14.389 (7)		
[Sm(dbm)$_3$(phen)]·(EtOH)			
Sm1 – O11	2.307 (3)		
Sm1 – O12	2.304 (3)		
Sm1 – O21	2.313 (3)		
Sm1 – O22	2.290 (3)		
Sm1 – O31	2.317 (3)		
Sm1 – O32	2.294 (3)		
Sm1 – N11	2.548 (4)		
Sm1 – N21	2.546 (4)		
Sm1 – Sm1	10.594 (3)		
Sm1 – Sm1	11.442 (7)		
Sm1 – Sm1	11.888 (5)		

*Table A5: Selected inter- and intra- molecular distances (Å) of the [Ln(**tbm**)$_3$(phen)] (Ln = Sm^{3+}, Y^{3+}), and [Ln(**tbm**)$_3$(d-phen)] (Ln = Eu^{3+}, Yb^{3+}).*

[Ln(tbm)$_3$(phen)]			
Sm^{3+}		**Y^{3+}**	
Sm1 – N11	2.616 (1)	Y001 – N009	2.558 (1)
Sm1 – N21	2.599 (1)	Y001 – N00C	2.530 (1)
Sm1 – O11	2.340 (1)	Y001 – O002	2.321 (1)
Sm1 – O12	2.388 (1)	Y001 – O003	2.279 (1)
Sm1 – O21	2.350 (1)	Y001 – O004	2.291 (1)
Sm1 – O22	2.376 (1)	Y001 – O005	2.314 (1)
Sm1 – O31	2.354 (1)	Y001 – O006	2.348 (1)
Sm1 – O32	2.402 (1)	Y001 – O007	2.284 (1)
Sm1 – Sm1	9.241 (6)	Y001 – Y001	9.236 (6)
π – π	3.257	π – π	3.243
Centroid – Centroid	3.395	Centroid – Centroid	3.400
[Ln(tbm)$_3$(*d*-phen)]			
Eu^{3+}		**Yb^{3+}**	
Eu1 – N1	2.603 (3)	Yb1 – N	2.488 (4)
Eu1 – N2	2.577 (3)	Yb1 – N0AA	2.526 (4)
Eu1 – O1	2.376 (2)	Yb1 – O0AA	2.247 (3)
Eu1 – O2	2.323 (2)	Yb1 – O1AA	2.290 (4)
Eu1 – O3	2.34 (2)	Yb1 – O2AA	2.256 (3)
Eu1 – O4	2.388 (2)	Yb1 – O3AA	2.313 (3)
Eu1 – O5	2.329 (2)	Yb1 – O4AA	2.259 (3)
Eu1 – O6	2.361 (2)	Yb1 – O5AA	2.292 (4)
Eu1 – Eu1	9.237 (6)	Yb1 – Yb1	9.206 (8)
π – π	3.250	π – π	3.238
Centroid – Centroid	3.392	Centroid – Centroid	3.410

10.4.3. Complexes from Chapter 4

*Table A6: Selected inter- and intra- molecular distances (Å) of the [Ln(**dnm**)$_3$(DMSO)$_2$] (Ln = Nd^{3+}, Sm^{3+}, Eu^{3+}, Gd^{3+}) complexes.*

	Nd^{3+}	**Gd^{3+}**
Ln1 – O1	2.420 (4)	2.366 (3)
Ln1 – O2	2.408 (5)	2.370 (3)
Ln1 – O3	2.403 (4)	2.369 (3)
Ln1 – O4	2.376 (6)	2.332 (3)
Ln1 – O5	2.381 (5)	2.333 (3)
Ln1 – O6	2.448 (5)	2.414 (3)
Ln1 – O7	2.454 (5)	2.425 (3)
Ln1 – O8	2.480 (5)	2.417 (3)
Ln1 – Ln1	7.606 (6)	7.845 (5)

Eu^{3+}		**Sm^{3+}**	
Eu1 – O004	2.378 (3)	Sm1 – O1	2.472 (3)
Eu1 – O005	2.417 (3)	Sm1 – O2	2.455 (3)
Eu1 – O006	2.377	Sm1 – O3	2.428 (4)
Eu1 – O007	2.340 (3)	Sm1 – O11	2.365 (3)
Eu1 – O008	2.337 (2)	Sm1 – O12	2.401 (3)
Eu1 – O009	2.380 (2)	Sm1 – O21	2.373 (2)
Eu1 – O00A	2.428 (3)	Sm1 – O22	2.406 (3)
Eu1 – O00B	2.433 (3)	Sm1 – O31	2.400 (2)
Eu1 – Eu1	7.703 (5)	Sm1 – O32	2.344 (3)
		Sm1 – Sm1	8.447 (5)